

Validation of Quantitative Measurements in Cardiovascular Imaging

Guest Editors: Peter M. A. van Ooijen, Marco Francone, Joachim Lotz, and Volker Rasche





Validation of Quantitative Measurements in Cardiovascular Imaging

BioMed Research International

Validation of Quantitative Measurements in Cardiovascular Imaging

Guest Editors: Peter M. A. van Ooijen, Marco Francone,
Joachim Lotz, and Volker Rasche



Copyright © 2015 Hindawi Publishing Corporation. All rights reserved.

This is a special issue published in “BioMed Research International.” All articles are open access articles distributed under the Creative Commons Attribution License, which permits unrestricted use, distribution, and reproduction in any medium, provided the original work is properly cited.

Contents

Validation of Quantitative Measurements in Cardiovascular Imaging, Peter M. A. van Ooijen, Marco Francone, Joachim Lotz, and Volker Rasche
Volume 2015, Article ID 321623, 2 pages

Semiautomatic, Quantitative Measurement of Aortic Valve Area Using CTA: Validation and Comparison with Transthoracic Echocardiography, V. Tuncay, N. Prakken, P. M. A. van Ooijen, R. P. J. Budde, T. Leiner, and M. Oudkerk
Volume 2015, Article ID 648283, 9 pages

The Fetal Modified Myocardial Performance Index: Is Automation the Future?, Priya Maheshwari, Amanda Henry, and Alec W. Welsh
Volume 2015, Article ID 215910, 9 pages

Free-Breathing 3D Imaging of Right Ventricular Structure and Function Using Respiratory and Cardiac Self-Gated Cine MRI, Yanchun Zhu, Jing Liu, Jonathan Weinsaft, Pascal Spincemaille, Thanh D. Nguyen, Martin R. Prince, Shanglian Bao, Yaoqin Xie, and Yi Wang
Volume 2015, Article ID 819102, 9 pages

Use of Contrast-Enhanced Ultrasound in Carotid Atherosclerotic Disease: Limits and Perspectives, Gianfranco Varetto, Lorenzo Gibello, Claudio Castagno, Simone Quaglino, Matteo Ripepi, Emilio Benintende, Andrea Gattuso, Paolo Garneri, Stefano Zan, Giacomo Capaldi, Ugo Bertoldo, and Pietro Rispoli
Volume 2015, Article ID 293163, 7 pages

Validation and Development of a New Automatic Algorithm for Time-Resolved Segmentation of the Left Ventricle in Magnetic Resonance Imaging, Jane Tufvesson, Erik Hedström, Katarina Steding-Ehrenborg, Marcus Carlsson, Håkan Arheden, and Einar Heiberg
Volume 2015, Article ID 970357, 12 pages

Development of an *Ex Vivo*, Beating Heart Model for CT Myocardial Perfusion, Gert Jan Pelgrim, Marco Das, Ulrike Haberland, Cees Slump, Astri Handayani, Sjoerd van Tuijl, Marco Stijnen, Ernst Klotz, Matthijs Oudkerk, Joachim E. Wildberger, and Rozemarijn Vliegenthart
Volume 2015, Article ID 412716, 8 pages

Importance of Reference Muscle Selection in Quantitative Signal Intensity Analysis of T2-Weighted Images of Myocardial Edema Using a T2 Ratio Method, Iacopo Carbone, Helene Childs, Ahmed Aljizeeri, Naeem Merchant, and Matthias G. Friedrich
Volume 2015, Article ID 232649, 9 pages

Editorial

Validation of Quantitative Measurements in Cardiovascular Imaging

Peter M. A. van Ooijen,¹ Marco Francone,² Joachim Lotz,³ and Volker Rasche⁴

¹*Department of Radiology, University Medical Center Groningen, University of Groningen, Groningen, Netherlands*

²*Department of Radiological Oncological and Pathological Sciences, Sapienza University of Rome, Rome, Italy*

³*University Medical Center Göttingen, Institute of Clinical and Interventional Radiology, Göttingen, Germany*

⁴*University of Ulm, Ulm, Germany*

Correspondence should be addressed to Peter M. A. van Ooijen; p.m.a.van.ooijen@umcg.nl

Received 30 April 2015; Accepted 30 April 2015

Copyright © 2015 Peter M. A. van Ooijen et al. This is an open access article distributed under the Creative Commons Attribution License, which permits unrestricted use, distribution, and reproduction in any medium, provided the original work is properly cited.

1. Introduction

Recent developments in cardiovascular imaging have shown a trend towards quantitative measurement of findings. These quantitative measurements could eventually be the basis to obtain quantitative imaging biomarkers that could be used to predict, diagnose, and treat disease. However, the first step to achieve quantitative imaging biomarkers is to establish proper validation of these quantitative measurements to ensure that the numbers obtained from the imaging data are reliable, reproducible, accurate, and clinically useful. This process involves the proper standardization and validation of all steps in the imaging process from acquisition, preprocessing, and postprocessing to reading and reporting. With the papers published in this special issue we hope to increase the evidence required to achieve quantitative imaging biomarkers in cardiovascular imaging by validation of those quantitative measurements in phantoms, animal models, and clinical data.

2. Modeling and Phantom Development

To allow proper validation the use of patient or volunteer data is often nonoptimal because of the lack of a gold-standard that can be used to validate the quantification. This often results in the use of other modalities or manual expert reading to validate against. One way of solving this issue could be the implementation of a phantom that can be used to perform

the validation. However, a shortcoming of these phantoms is often their lack of realism with respect to anatomy and function. G. J. Pelgrim et al. describe in their contribution how they implemented an ex vivo, perfused porcine heart model for myocardial perfusion CT imaging. These kinds of developments where animal organs are used as basis for a phantom could provide a more real-life environment while also providing the possibility of obtaining the gold standard by additional measurements, controlled experiments, and pathological evaluation.

3. Acquisition Technique and Protocol

Acquisition techniques and protocols are vendor specific, resulting in a variation in measured values for the same morphological or functional parameters. To overcome these differences, standardization and calibration of acquisition systems and protocols could be part of the solution.

For example, a review by G. Varetto et al. on the value of contrast enhanced ultrasound (CEUS) for vulnerable plaque analysis. These kinds of reviews can provide valuable information on the validity of acquisition techniques and allow a discussion of the possibility of generalized acquisition protocols with high accuracy and reliability to allow a more standardized quantification. One of the aspects revealed by this study that although the reliability of the acquisition technique is high, a shared, user-friendly protocol of imaging

analysis is not available yet although this would be mandatory to allow comparison of results.

Patient cooperation can also be an issue in the acquisition of data that can be used for quantitative evaluation. Y. Zhu et al. show that the accuracy and reproducibility of the current technique for right ventricular evaluation using 2D breath-hold MR can be compromised by slice misregistration or requirement to use a larger slice gap. This is mainly caused by the inability of the patients to hold their breath consistently during the acquisition. To overcome these problems 3D scan protocols are developed that are hampered by the fact that they require a long breath-hold. They therefore propose, in their paper, the use of a free-breathing 3D imaging acquisition to tackle these problems while retaining a dataset of proper quality to allow quantitative measurement of RV function.

4. Postprocessing Algorithms and Validation

Postprocessing techniques are applied in all imaging modalities to obtain quantitative information. However, there is usually no standardization available and all research groups and vendors have their own algorithms and approach. Part of the solution is in the automation of algorithms, thus eliminating the observer influence. Another part is the extensive cross-validation of different algorithms and approaches.

Segmentation of the left ventricle for the determination of left ventricular function has been an area of research for quite some time already. The literature has shown an increasing reproducibility and accuracy of algorithms used for this segmentation although many still rely on either manual segmentation or manual correction of automatically generated contours. One of the main problems in the segmentation of the left ventricle is its complex motion during the cardiac cycle. Of this the long-axis motion is often not taken into account. The study by J. Tufvesson et al. presented in this special issue aims to develop and validate an automatic postprocessing algorithm for time-resolved segmentation, covering the whole LV, including basal slices affected by long-axis motion. They show minor differences between manual segmentation and their automatic segmentation resulting in an algorithm that is very well applicable in clinical practice.

Another example of automation in segmentation of areas of interest is the work by V. Tuncay et al. who describe a newly developed semiautomatic segmentation technique to determine the Aortic Valve Area in MDCT datasets. They show that automation of this measurement provides accurate, more reproducible, and faster measurement. Validation was done by comparing both to manual expert segmentation and to measurements obtained with a more established modality (Transthoracic Echocardiography) performed in the same patient.

The importance of proper validation and calibration of measurements is also demonstrated in the paper by I. Carbone et al. They studied the suitability of several skeletal muscles as reference regions for calculating the T2-SI-ratio for semiautomatic quantification of the extent of myocardial edema. In result it was shown that using the serratus anterior is the most reliable and reproducible muscle for measuring the extent of myocardial edema.

P. Maheshwari et al. show in their review paper that although a measurement such as the modified Myocardial Performance Index (Mod-MPI) is well-established, standardization can still be lacking resulting in varying outcomes between different operators. They therefore propose an automated measurement of the Mod-MPI to allow its proper implementation into clinical use.

*Peter M. A. van Ooijen
Marco Francone
Joachim Lotz
Volker Rasche*

Research Article

Semiautomatic, Quantitative Measurement of Aortic Valve Area Using CTA: Validation and Comparison with Transthoracic Echocardiography

V. Tuncay,¹ N. Prakken,² P. M. A. van Ooijen,^{1,2}
R. P. J. Budde,³ T. Leiner,³ and M. Oudkerk¹

¹Center for Medical Imaging North East Netherlands (CMI-NEN), Department of Radiology, University of Groningen, University Medical Center Groningen, P.O. Box 30001, 9700 RB Groningen, Netherlands

²Department of Radiology, University of Groningen, University Medical Center, P.O. Box 30001, 9700 RB Groningen, Netherlands

³Department of Radiology, University Medical Center Utrecht, P.O. Box 85500, 3508 GA Utrecht, Netherlands

Correspondence should be addressed to P. M. A. van Ooijen; p.m.a.van.ooijen@umcg.nl

Received 12 September 2014; Accepted 3 April 2015

Academic Editor: Michael Gotzmann

Copyright © 2015 V. Tuncay et al. This is an open access article distributed under the Creative Commons Attribution License, which permits unrestricted use, distribution, and reproduction in any medium, provided the original work is properly cited.

Objective. The aim of this work was to develop a fast and robust (semi)automatic segmentation technique of the aortic valve area (AVA) MDCT datasets. **Methods.** The algorithm starts with detection and cropping of Sinus of Valsalva on MPR image. The cropped image is then binarized and seed points are manually selected to create an initial contour. The contour moves automatically towards the edge of aortic AVA to obtain a segmentation of the AVA. AVA was segmented semiautomatically and manually by two observers in multiphase cardiac CT scans of 25 patients. Validation of the algorithm was obtained by comparing to Transthoracic Echocardiography (TTE). Intra- and interobserver variability were calculated by relative differences. Differences between TTE and MDCT manual and semiautomatic measurements were assessed by Bland-Altman analysis. Time required for manual and semiautomatic segmentations was recorded. **Results.** Mean differences from TTE were -0.19 (95% CI: -0.74 to 0.34) cm^2 for manual and -0.10 (95% CI: -0.45 to 0.25) cm^2 for semiautomatic measurements. Intra- and interobserver variability were $8.4 \pm 7.1\%$ and $27.6 \pm 16.0\%$ for manual, and $5.8 \pm 4.5\%$ and $16.8 \pm 12.7\%$ for semiautomatic measurements, respectively. **Conclusion.** Newly developed semiautomatic segmentation provides an accurate, more reproducible, and faster AVA segmentation result.

1. Introduction

Aortic stenosis (AS) is the most common valvular heart disease in the developed countries, affecting 3 percent of the population older than 65 years. It causes higher morbidity and mortality than any other cardiac valve disease [1]. AS is defined as narrowing of the aortic valve opening, which reduces blood flow from the heart into the aorta. The normal size of the aortic valve area (AVA) at maximum opening of the valve is 3 to 4 cm^2 [2]. When the AVA decreases below 1 cm^2 , AS is considered to be severe [3]. For severe AS, valve replacement is the only effective treatment. However, a sizeable fraction of patients are at high risk for postoperative mortality and may refuse surgery or cannot undergo surgery due to comorbidity [4]. Recently, transcatheter aortic valve

replacement (TAVR) techniques have been developed to provide less invasive treatment for those patients [5–11]. In management of AS, the timing for surgical treatment is very important. Late treatment may lead to an increase in the transaortic pressure gradient, myocardial pressure overload, and eventually left ventricular (LV) hypertrophy and increased LV wall thickness [12]. Visualization of the AVA is used to determine the threshold for invasive treatment and to obtain preoperative information about the aortic dimensions and proximity to other important structures such as the coronary arteries.

Different imaging modalities have been used and compared for measuring the AVA [13–23]. Initially, catheterization was the standard method for evaluating AVA, but in time its usage decreased due to its being an invasive modality

and technical limitations. Alternatively, the 2D echocardiographic continuity equation, which currently is the most common tool to derive the AVA, was used to measure the AVA. However, this technique underestimates AVA since it assumes that the left ventricular outflow tract (LVOT) has circular geometry and that flow through the LVOT is laminar and uniform [24, 25]. Bruder et al. showed a strong correlation between the AVA determined by echocardiography and MRI [20] indicating that MRI can also be used to determine AVA. However, MRI is contraindicated for patients with metal implants or claustrophobia. Moreover MRI has lower spatial resolution in comparison to CT [12]. More recently, development of ECG-gated multidetector computed tomography (MDCT) has led to further improvements in cardiac imaging [21], and CT is now also regarded as a reliable method to measure the AVA [26]. The latest developments in dual source and 320-slice CT enable high temporal resolution acquisition and obtain sufficient image quality at high spatial resolution in almost every patient throughout the cardiac cycle. However, streaking and blooming artifacts due to heavy calcification of the aortic valve leaflets or the aortic root which hamper visualization and analysis of the AVA can still occur.

Delgado and Bax suggested that 3D planimetric measurement of the AVA by MDCT images may provide more reliable information on the assessment of AVA in comparison with echocardiography [27]. However, planimetric measurement of AVA is currently performed manually by the radiologist using standard 3D visualization and measurement software, which is time consuming and introduces user dependence and intra- and interobserver variability [28].

The aim of this study was to develop and validate a (semi)automatic segmentation technique of the AVA and to compare manual and semiautomatic measurements with the Transthoracic Echocardiography (TTE) results. Our goal is to reduce the user dependency and time spent on measurements and to enable reproducible and accurate measurement of AVA on MDCT datasets.

2. Materials and Methods

2.1. Experimental Design. In this study multiphase CT scans of 25 patients (15 female, mean age 82.84 ± 5.16 years) were used. All of the patients had moderate to severe aortic stenosis and underwent TAVI at a tertiary referral center. All subjects underwent CT scanning and TTE.

Informed consent requirement was waived by the local IRB because of the retrospective nature of this study without additional burden to the patients involved.

The maximum aortic valve opening phase was selected visually for all patients. A stack of reformations was obtained after centering the axis of the multiplanar reconstruction (MPR) at the level of aortic valve and then changing the orientation of the plane perpendicular to the LVOT. The preselected slices were segmented both manually and semiautomatically by two independent observers 1, a biomedical engineer with more than 5 years of experience, and 2, a cardiac radiologist with almost 10 years of medical imaging experience. Observer 1 repeated the measurement 1 day after in order to determine intraobserver variability. Manual

and semiautomatic measurements were compared with the current reference standard Transthoracic Echocardiography (TTE) with regard to AVA. Time spent for measurements was recorded for manual and semiautomatic segmentations.

2.2. Transthoracic Echocardiography. TTE was performed as part of the routine workup of the patient. TTE derived AVA measurements were obtained from the clinical patient records. The velocity in the left ventricular outflow tract and at the level of the aortic valve and the LVOT diameter were measured. From these measurements the AVA was calculated using the continuity equation.

2.3. Multislice Computed Tomography. Image acquisition of the retrospectively ECG-gated CTA of the thoracoabdominal aorta was performed on a multidetector 256-slice CT (Brilliance iCT, Philips Healthcare, Best, The Netherlands). An ECG trace was recorded during the procedure. The region of acquisition ranged from above the aortic arch to the groin. Based on a locator image, a circular region of interest was drawn within the descending aorta. Nonionic iodinated contrast material (Ultravist, 300 mg iopromide per mL, Schering Nederland BV, Weesp, The Netherlands) was injected intravenously. As soon as the descending aorta reached a density of 125 Hounsfield units (HU) within the region of interest, the patient was instructed to maintain a breath hold. Seven seconds later, image acquisition started in a craniocaudal direction with concurrent ECG trace recording. The following parameters were used: detector collimation 128×0.625 mm; pitch 0.30; matrix size 512×512 . Tube voltage and tube current-time product depended on the patient's weight and were 100 kVp and 300 mAs, respectively, for patients <70 kg, and 120 kVp and 250 mAs, respectively, for patients ≥ 70 kg.

2.4. AVA Segmentation Algorithm. The segmentation algorithm (Figure 1) starts with the detection of the Sinus of Valsalva (SOV) on the MPR image. Once the SOV is detected, the region covering the SOV is cropped from the whole image (Figure 1(a)). The cropped image (Figure 1(b)) is binarized by adaptive thresholding (Figure 1(c)). The user places seed points (Figure 1(d)) to create an initial contour (Figure 1(e)) covering the aortic valve opening. The contour moves towards the edge of the aortic valve opening automatically (Figure 1(f)). The contour covers the pixels from the edge of the opening area and also the AVA opening area. The pixels of the opening area are selected and the number of pixels is multiplied by the pixel size to determine the AV opening area (Figure 1(g)).

2.4.1. Detection and Cropping of the Sinus of Valsalva. Image cropping was used to reduce computation time. In the object detection the object size, shape, location, and orientation play major roles. Since the SOV is located in the central part of the MPR image, detection and cropping of this region begin with a preliminary cropping operation, which covers the most of the central part of the MPR image. After the initial cropping, the grayscale image is binarized using global thresholding with a threshold level based on the histogram

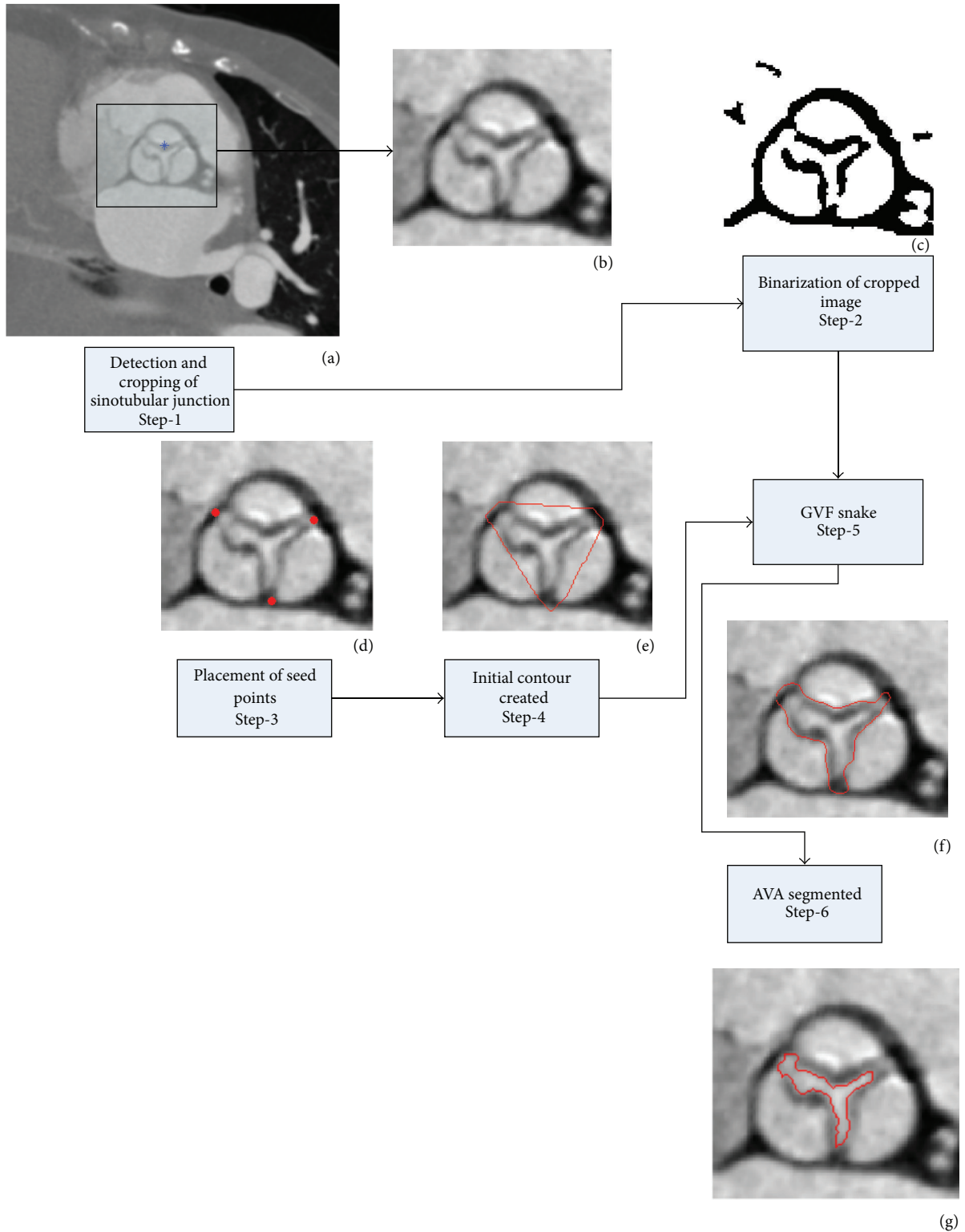


FIGURE 1: The flowchart of the general algorithm.

of the image. The binary image contains only white (object) and black (background) pixels, which enables detection of the objects in the image and facilitates the use of morphological operations. Following binarization, objects smaller than 700

pixels were removed. Secondly the SOV was disconnected and isolated. The SOV is located in the central part of image, such that objects on the border of the image were removed. After detection of the SOV, the region covering it was cropped

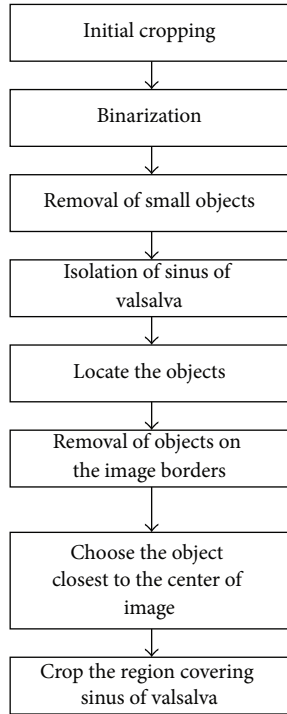


FIGURE 2: The flowchart of the SOV detection and cropping algorithm.

from the image (Figure 2). All following operations were performed on the cropped image.

2.4.2. Segmentation of AVA. The flowchart in Figure 3 shows the details of the segmentation of the AVA. The main segmentation tool is the gradient vector flow (GVF) snake [29]. The snake algorithm is an active contour, which moves to the edges of the object in order to reach the boundaries of the object. In the binarized images (described above) the edges are clearer and the active contour can move towards the object boundaries easier compared to grayscale images. The user places three seed points on the grayscale image where the cusps are connected to each other to create the initial contour for the GVF snake. This initial contour creates a mask image, which is used on the binarized image. The active contour shrinks to cover the AVA region. However, the GVF snake result overestimates the AVA. Therefore this GVF snake contour is used to mask the image again. In case the resulting double-masked image contains more than 1 object, the size and location of these objects were determined. Objects smaller than 40 mm^2 and the object most distant from the center were removed. The remaining object was identified as the AVA.

2.4.3. Detection and Removal of Calcification. Aortic valve calcification is very common in a population with AS. In order to segment the AVA properly one must first detect the calcifications and then exclude the calcified areas from the AVA region. Since a contrast agent was used in the CT scans we cannot use the fixed 130 HU threshold to detect pixels

in calcified areas. We therefore developed an algorithm to determine the threshold of calcified pixels, consisting of the following 5 steps:

- (1) Calculation of the histogram (Figure 4) and determination of the index number (index) of the maximum pixel intensity (im_{Max}).
- (2) Calculation of the maximum histogram value ($MaxH$).
- (3) Decreasing the index until reaching $MaxH/3$ and setting the corresponding intensity level as the initial estimation ($T_{calcest}$) for calculation of calcium threshold (T_{calc}).
- (4) Determination of the dynamic range of the image.
 - (i) Starting from the first bin of the histogram, the amount of pixels in each bin was counted until reaching half of the total number of pixels.
 - (ii) The index number of the histogram bin where the algorithm stopped corresponds to the dynamic range (DR) of the image.
- (5) Calculation of the calcium threshold (T_{calc}) for $DR > 0.7 * im_{Max}$ (brighter images) by (1) and T_{calc} for $DR < 0.7 * im_{Max}$ was calculated by (2):

$$T_{calc} = T_{calcest} + (im_{Max} - T_{calcest}) * 0.5, \quad (1)$$

$$T_{calc} = T_{calcest} + (im_{Max} - T_{calcest}) * 0.2. \quad (2)$$

An example is given in Figure 5. The calcified pixels on grayscale image (Figure 5(a)) are detected and given a blue color (Figure 5(b)).

2.5. Computation Time. Computation time was defined as the time between the visualization of the final cropped image and the display of the measurement of the AVA size. For manual measurements it included the time required for the user to trace the orifice perimeter and the calculation of the selected area. For the semiautomatic measurements it included the selection of the seed points by the user and the computation of AVA based on the semiautomatic segmentation results. The time was measured internally by the developed software tool and displayed when the AVA size measurement was finished.

2.6. Validation and Statistical Analysis. Relative differences between the measurements were calculated to determine (1) the intraobserver variability of the semiautomatic measurements and (2) the intraobserver variability of the manual measurements. Relative difference was calculated as follows:

$$\text{Relative difference} = \frac{\text{Absolute difference} * 100}{\text{Mean of the measurements}}. \quad (3)$$

Differences between TTE and MDCT manual and semiautomatic measurements were assessed by Bland-Altman plots. Statistical analyses were performed using IBM SPSS Statistics version 20.0.0.1 (SPSS Inc., Chicago, USA).

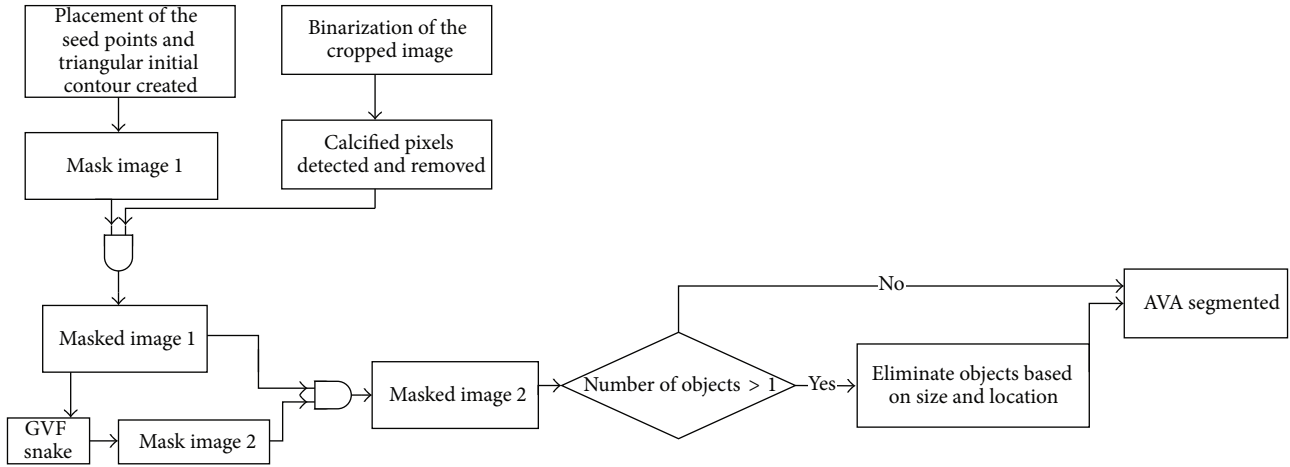


FIGURE 3: The flowchart of the AVA segmentation algorithm.

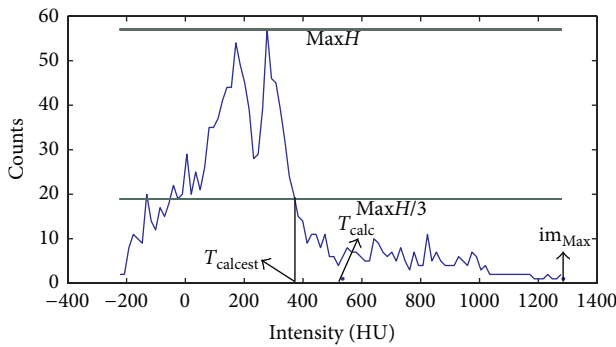


FIGURE 4: The histogram of the grayscale image.

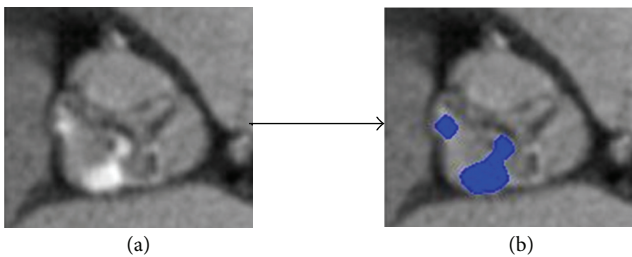


FIGURE 5: Example of the calcium detection algorithm.

3. Results

3.1. Segmentation Results. Aortic valve areas as measured manually and semiautomatically are listed in Table 1. Sample results of the semiautomatic segmentation are given in Figure 6. Semiautomatic segmentation of AVA was achieved successfully for both calcified (Figures 6(a), 6(b), and 6(d)) and noncalcified aortic valves (Figure 6(c)). The output result of a segmentation and computation time for a sample image is given in Figure 6(e) showing one part of the graphic user interface.

3.2. Computation Time. The computation times of both observers were shorter for the semiautomatic measurements.

TABLE 1: Manual and semiautomatic AVA measurements.

	Mean \pm SD
Observer 1, manual measurements (cm ²)	0.88 \pm 0.23
Observer 1, semiautomatic measurements (cm ²)	0.85 \pm 0.15
Observer 2, manual measurements (cm ²)	0.98 \pm 0.29
Observer 2, semiautomatic measurements (cm ²)	0.82 \pm 0.18

TABLE 2: Observer variability.

	Relative difference (%)
Intraobserver variability, manual	8.4 \pm 7.1
Intraobserver variability, semiautomatic	5.8 \pm 4.5
Interobserver variability, manual	27.6 \pm 16.0
Interobserver variability, semiautomatic	16.8 \pm 12.7

Manual measurements took 18.85 ± 5.66 seconds and 16.69 ± 3.69 seconds for observer 1 and observer 2, respectively. Semiautomatic measurements were 5.06 ± 0.72 (observer 1) and 6.68 ± 1.79 seconds (observer 2).

3.3. Observer Variability. Differences in intraobserver variability of manual and semiautomatic measurements are listed in Table 2. Both intra- and interobserver variability were lower for semiautomatic measurements.

3.4. Comparing Manual and Semiautomatic Measurements with TTE. Comparisons of the manual and semiautomatic measurements with TTE results were performed using Bland-Altman plots; mean difference between TTE and MDCT results was -0.19 (95% CI: -0.74 to 0.34) cm² for manual and -0.10 (95% CI: -0.45 to 0.25) cm² for semiautomatic measurements (Figures 7 and 8). The differences were significantly different from 0 ($p = 0.001$ for manual and $p = 0.007$ for semiautomatic measurements) indicating a bias. Both mean difference and the confidence interval are smaller in the comparison of TTE and semiautomatic measurements which indicates that semiautomatic measurements are closer to the TTE measurements than to the manual measurements.

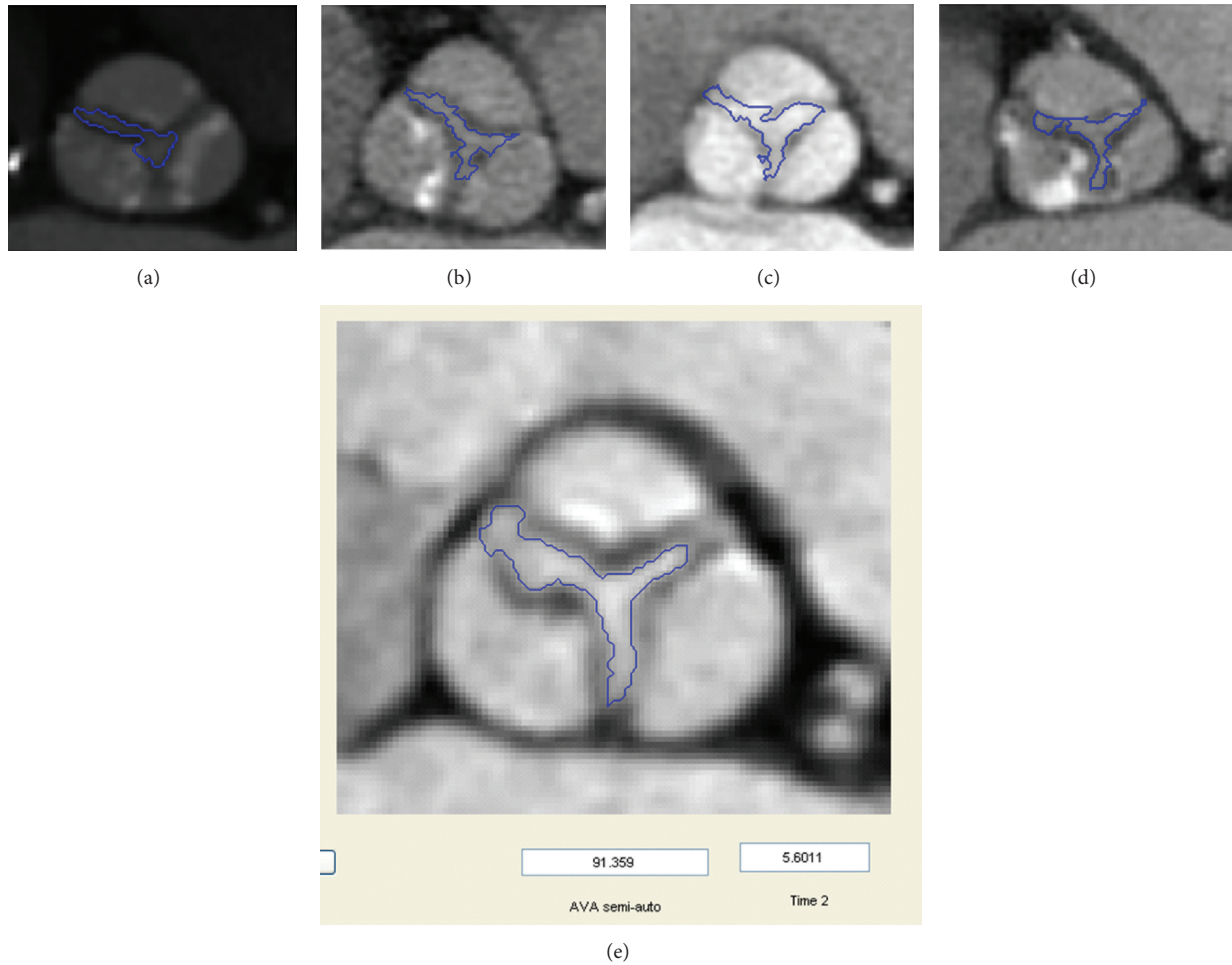


FIGURE 6: Results of semiautomatic measurements on various images (a–d). Result on graphic user interface (e).

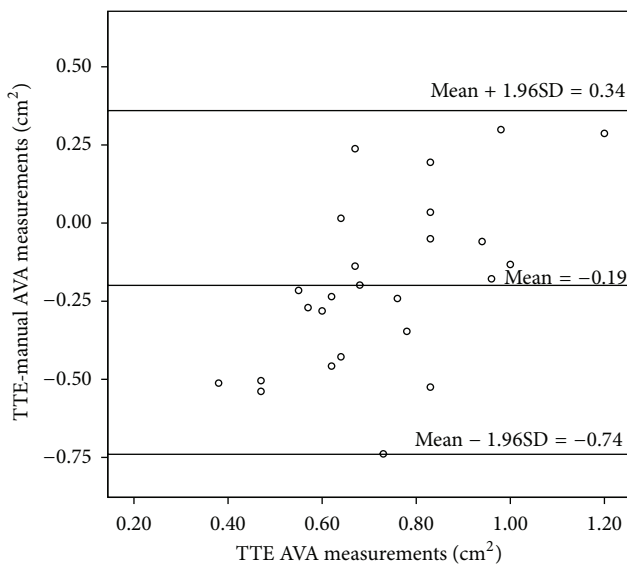


FIGURE 7: Bland-Altman plot between the TTE and manual AVA measurements.

4. Discussion

4.1. Research Summary. In this study we propose a semi-automatic segmentation technique to measure the AVA and compared it with the manual segmentation using TTE measurements as the reference standard. The focus of the study was to investigate whether the repeatability and reproducibility of the AVA measurements can be improved with the semiautomatic segmentation along with an improvement in computation time. First of all, our results show that semiautomatic measurements are closer to the reference TTE measurements. Furthermore the intra- and interobserver variations are lower for the semiautomatic measurements compared to manual measurements. Finally semiautomatic measurements are more than 10 seconds faster than the manual measurements.

4.2. Previous Studies and Current Study. TTE is currently the most widely used imaging modality to measure the AVA. The continuity equation, which is used to calculate the AVA based on 2D TTE data, assumes that the LVOT has a circular shape.

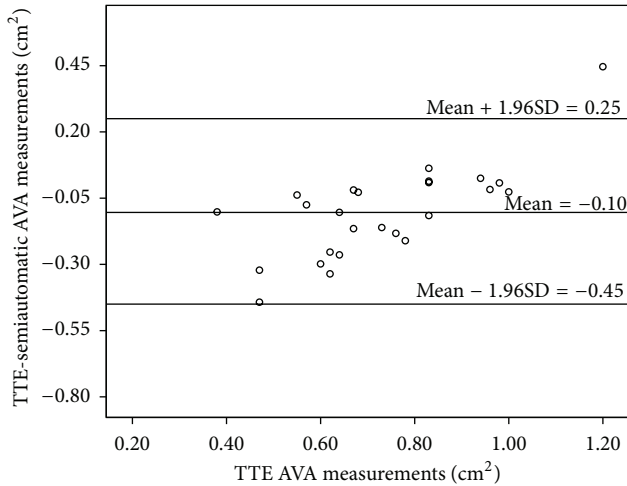


FIGURE 8: Bland-Altman plot between the TTE and semiautomatic AVA measurements.

A recent study showed that this assumption might cause underestimation of the AVA [30]. TTE was compared to CT in several studies. Larsen et al. observed 6% and 16% intra- and interobserver variability for MDCT measurements on patient with broad severity of AS. Meanwhile the intra- and interobserver variability were 13% and 19% for the TTE measurements [31]. In our study the interobserver variability of semiautomatic measurements was 16% in the measurements on the patients with severe AS. Lembcke et al. conducted a study with 160 patients using 64-MDCT and TTE. They found $0.17 \pm 0.24 \text{ cm}^2$ mean difference between MDCT and TTE measurements [32]. In our study we observed $0.19 \pm 0.27 \text{ cm}^2$ and $0.10 \pm 0.18 \text{ cm}^2$ mean differences in the comparisons of TTE with manual and semiautomatic MDCT measurements, respectively.

Even though (semi)automatic quantification of the aortic root dimensions such as aortic annulus, Sinus of Valsalva, and sinotubular junction using CT data has already been available in the literature [33] there is a paucity of data about (semi)automatic quantification of the AVA using CT images. Previous research already showed that echocardiography underestimates that the AVA and CT planimetric measurements are closer to the real AVA. Moreover CT is the modality used for measuring the aortic valve calcium score which associated with AS. All of these reasons make CT the method of choice. However, planimetric CT measurement of the AVA is currently performed manually, which is user dependent and time consuming. Our results demonstrate the feasibility of developing an algorithm for semiautomatic quantitative measurements of AVA in order to reduce observer variability and the time spent on the measurements. Moreover this technique is shown to also work on the target population of AS patients with a significant calcium load. The calcified regions should be detected and the opening area should be segmented excluding the calcified area. A calcification threshold is needed in order to detect the pixels belonging to the calcified region. However, in virtually all CT scans made for preoperative evaluation in patients with aortic stenosis

a contrast agent is injected which makes it impossible to set a fixed calcification threshold. To overcome this issue, an algorithm was developed to calculate the calcification threshold for each CTA image individually.

The ultimate goal of fully automatic user independent segmentation was not achieved and user selection of three seed points is still required in the semiautomatic segmentation. Main reason for this is that the image quality with the current CT technology does not allow making the AVA segmentation fully automatic due to unclear object (AV) boundaries in some cases. The GVF snake was the method of choice since the snake algorithm works in cases where some parts of the object boundaries are not clear. A possible solution to make the segmentation less user dependent could be to develop an algorithm which can detect parts of the AVA boundaries (semi)automatically and interpolate the rest of the object boundary. Further developments in CT technology with higher spatial resolution and less calcium artifacts might also help to achieve the goal of fully automatic segmentation of the AVA. Our results show that CT based AVA segmentation can be achieved with less user dependence and as a result a higher reproducibility and less time consuming measurements of AVA segmentation were obtained.

4.3. Limitations. A possible limitation of our study was that the users were not asked to rechoose the phase and opening plane on which to measure the AVA. However, this choice was made to eliminate the user interference in the measurement results in order to really test the accuracy of the developed algorithm. Another limitation of this study is the selected patient group. We studied a relatively small sample of patients with varying delay between TTE and CT imaging and all subjects had severe AS (mean AVA smaller than 1.0 cm^2). Future work will have to be carried out in larger cohorts containing subject with varying degrees of AS. Also, we cannot rule out that differences in AVA can be attributed to differences in area over time as opposed to difference inherent to the imaging techniques used. The time difference between the CT and ultrasound measurements was more than 100 days for 6 patients. A final limitation is having 2 different measurement techniques using the TTE and MDCT data. In MDCT measurements we had the direct measurements using the planimetric image of the AVA; on the other hand AVA was measured indirectly by the flow information gathered by the TTE. This difference between the measurement techniques led to the variation between the TTE and MDCT manual and semiautomatic measurements. Therefore further work required to determine what the clinical followup should be based on MDCT measurements.

4.4. Implications. Studies comparing the use of CT and echocardiography found that CT can be an alternative to the current gold standard echocardiography in the quantification of AVA [26, 27]. Our study has some implications in semiautomatic quantification of AVA on the CT images. First of all the intra- and interobserver variability of semiautomatic measurements are better than the manual measurements. These results imply that the variation caused by the user interaction is decreased by using the semiautomatic software,

which is desirable for quantitative assessment of medical images. Moreover semiautomatic software provides a faster calculation of the AVA in comparison with the manual measurements. Faster measurements decrease the workload. The comparison of manual and semiautomatic CT measurements with the current standard TTE measurements revealed that semiautomatic measurements are closer to the TTE measurements. If the standard modality for measuring the AVA will switch from echocardiography to CT, semiautomatic measurements can serve as a better option in comparison to the manual measurements due to the smaller difference between the TTE and semiautomatic measurements.

5. Conclusion

In this study a semiautomatic segmentation technique that can be used in AVA segmentation is proposed. Based on preliminary results the algorithm provides adequate segmentation of representative images, also those including severe calcification, and provides a faster, more accurate, and more reproducible AVA segmentation compared to the currently used manual segmentation.

Disclosure

The authors would like to state that there is no relationship with industry in this study. Recently, R. P. J. Budde moved to the Erasmus Medical Center, Rotterdam, The Netherlands.

Conflict of Interests

The authors declare that there is no conflict of interests regarding the publication of this paper.

References

- [1] M. Lindroos, M. Kupari, J. Heikkilä, and R. Tilvis, "Prevalence of aortic valve abnormalities in the elderly: an echocardiographic study of a random population sample," *Journal of the American College of Cardiology*, vol. 21, no. 5, pp. 1220–1225, 1993.
- [2] W. Grossman, D. Jones, and L. P. McLaurin, "Wall stress and patterns of hypertrophy in the human left ventricle," *The Journal of Clinical Investigation*, vol. 56, no. 1, pp. 56–64, 1975.
- [3] American College of Cardiology/American Heart Association Task Force on Practice Guidelines, Society of Cardiovascular Anesthesiologists, Society for Cardiovascular Angiography and Interventions et al., "ACC/AHA 2006 guidelines for the management of patients with valvular heart disease: a report of the American College of Cardiology/American Heart Association Task Force on Practice Guidelines (writing committee to revise the 1998 Guidelines for the Management of Patients With Valvular Heart Disease): developed in collaboration with the Society of Cardiovascular Anesthesiologists: endorsed by the Society for Cardiovascular Angiography and Interventions and the Society of Thoracic Surgeons," *Circulation*, vol. 114, no. 5, pp. e84–e231, 2006.
- [4] B. Iung, A. Cachier, G. Baron et al., "Decision-making in elderly patients with severe aortic stenosis: why are so many denied surgery?" *European Heart Journal*, vol. 26, no. 24, pp. 2714–2720, 2005.
- [5] H. R. Andersen, L. L. Knudsen, and J. M. Hasenkam, "Transluminal implantation of artificial heart valves. Description of a new expandable aortic valve and initial results with implantation by catheter technique in closed chest pigs," *European Heart Journal*, vol. 13, no. 5, pp. 704–708, 1992.
- [6] A. Cribier, H. Eltchaninoff, C. Tron et al., "Early experience with percutaneous transcatheter implantation of heart valve prosthesis for the treatment of end-stage inoperable patients with calcific aortic stenosis," *Journal of the American College of Cardiology*, vol. 43, no. 4, pp. 698–703, 2004.
- [7] E. Grube, J. C. Laborde, U. Gerckens et al., "Percutaneous implantation of the CoreValve self-expanding valve prosthesis in high-risk patients with aortic valve disease: the siegburg first-in-man study," *Circulation*, vol. 114, no. 15, pp. 1616–1624, 2006.
- [8] E. Grube, G. Schuler, L. Buellesfeld et al., "Percutaneous aortic valve replacement for severe aortic stenosis in high-risk patients using the second- and current third-generation self-expanding CoreValve prosthesis: device success and 30-day clinical outcome," *Journal of the American College of Cardiology*, vol. 50, no. 1, pp. 69–76, 2007.
- [9] S. V. Lichtenstein, A. Cheung, J. Ye et al., "Transapical transcatheter aortic valve implantation in humans: initial clinical experience," *Circulation*, vol. 114, no. 6, pp. 591–596, 2006.
- [10] J. G. Webb, M. Chandavimol, C. R. Thompson et al., "Percutaneous aortic valve implantation retrograde from the femoral artery," *Circulation*, vol. 113, no. 6, pp. 842–850, 2006.
- [11] J. G. Webb, S. Pasupati, K. Humphries et al., "Percutaneous transarterial aortic valve replacement in selected high-risk patients with aortic stenosis," *Circulation*, vol. 116, no. 7, pp. 755–763, 2007.
- [12] N. Saikrishnan, G. Kumar, F. J. Sawaya, S. Lerakis, and A. P. Yoganathan, "Accurate assessment of aortic stenosis: a review of diagnostic modalities and hemodynamics," *Circulation*, vol. 129, no. 2, pp. 244–253, 2014.
- [13] J. K. Willmann, D. Weishaupt, M. Lachat et al., "Electrocardiographically gated multi-detector row CT for assessment of valvular morphology and calcification in aortic stenosis," *Radiology*, vol. 225, no. 1, pp. 120–128, 2002.
- [14] G. M. Feuchtner, S. Müller, J. Bonatti et al., "Sixty-four slice CT evaluation of aortic stenosis using planimetry of the aortic valve area," *American Journal of Roentgenology*, vol. 189, no. 1, pp. 197–203, 2007.
- [15] E. Bouvier, D. Logeart, J.-L. Sablayrolles et al., "Diagnosis of aortic valvular stenosis by multislice cardiac computed tomography," *European Heart Journal*, vol. 27, no. 24, pp. 3033–3038, 2006.
- [16] R. C. Gilkeson, A. H. Markowitz, A. Balgude, and P. B. Sachs, "MDCT evaluation of aortic valvular disease," *American Journal of Roentgenology*, vol. 186, no. 2, pp. 350–360, 2006.
- [17] S. J. Cowell, D. E. Newby, J. Burton et al., "Aortic valve calcification on computed tomography predicts the severity of aortic stenosis," *Clinical Radiology*, vol. 58, no. 9, pp. 712–716, 2003.
- [18] R. Koos, A. H. Mahnken, A. M. Sinha, J. E. Wildberger, R. Hoffmann, and H. P. Kühl, "Aortic valve calcification as a marker for aortic stenosis severity: assessment on 16-MDCT," *American Journal of Roentgenology*, vol. 183, no. 6, pp. 1813–1818, 2004.
- [19] G. J. Morgan-Hughes, P. E. Owens, C. A. Roobottom, and A. J. Marshall, "Three dimensional volume quantification of aortic valve calcification using multislice computed tomography," *Heart*, vol. 89, no. 10, pp. 1191–1194, 2003.

- [20] O. Bruder, M. Jochims, P. Hunold et al., "Comparison of aortic valve area measured by magnetic resonance imaging and dual-source computed tomography," *Acta Radiologica*, vol. 50, no. 6, pp. 645–651, 2009.
- [21] A. Lembcke, D. E. Kivelitz, A. C. Borges et al., "Quantification of aortic valve stenosis: head-to-head comparison of 64-slice spiral computed tomography with transesophageal and transthoracic echocardiography and cardiac catheterization," *Investigative Radiology*, vol. 44, no. 1, pp. 7–14, 2009.
- [22] E. J. Weinberg and M. R. Kaazempur Mofrad, "A multiscale computational comparison of the bicuspid and tricuspid aortic valves in relation to calcific aortic stenosis," *Journal of Biomechanics*, vol. 41, no. 16, pp. 3482–3487, 2008.
- [23] F. Chenot, P. Montant, C. Goffinet et al., "Evaluation of anatomic valve opening and leaflet morphology in aortic valve bioprosthesis by using multidetector CT: comparison with transthoracic echocardiography," *Radiology*, vol. 255, no. 2, pp. 377–385, 2010.
- [24] F. A. Flachskampf, "Severe aortic stenosis with low gradient and apparently preserved left ventricular systolic function—under-recognized or overdiagnosed?" *European Heart Journal*, vol. 29, no. 8, pp. 966–968, 2008.
- [25] K. K. Poh, R. A. Levine, J. Solis et al., "Assessing aortic valve area in aortic stenosis by continuity equation: a novel approach using real-time three-dimensional echocardiography," *European Heart Journal*, vol. 29, no. 20, pp. 2526–2535, 2008.
- [26] O. Klass, M. J. Walker, M. E. Olszewski et al., "Quantification of aortic valve area at 256-slice computed tomography: comparison with transesophageal echocardiography and cardiac catheterization in subjects with high-grade aortic valve stenosis prior to percutaneous valve replacement," *European Journal of Radiology*, vol. 80, no. 1, pp. 151–157, 2011.
- [27] V. Delgado and J. J. Bax, "Classical methods to measure aortic valve area in the era of new invasive therapies: still accurate enough?" *International Journal of Cardiovascular Imaging*, vol. 25, no. 2, pp. 183–185, 2009.
- [28] T. Gaspar, S. Adawi, R. Sachner et al., "Three-dimensional imaging of the left ventricular outflow tract: impact on aortic valve area estimation by the continuity equation," *Journal of the American Society of Echocardiography*, vol. 25, no. 7, pp. 749–757, 2012.
- [29] C. Xu and J. L. Prince, "Snakes, shapes, and gradient vector flow," *IEEE Transactions on Image Processing*, vol. 7, no. 3, pp. 359–369, 1998.
- [30] H. Utsunomiya, H. Yamamoto, J. Horiguchi et al., "Underestimation of aortic valve area in calcified aortic valve disease: effects of left ventricular outflow tract ellipticity," *International Journal of Cardiology*, vol. 157, no. 3, pp. 347–353, 2012.
- [31] L. H. Larsen, K. F. Kofoed, H. G. Carstensen et al., "Aortic valve area assessed with 320-detector computed tomography: comparison with transthoracic echocardiography," *International Journal of Cardiovascular Imaging*, vol. 30, no. 1, pp. 165–173, 2014.
- [32] A. Lembcke, M. Woinke, A. C. Borges et al., "Grading of aortic valve stenosis at 64-slice spiral computed tomography: comparison with transthoracic echocardiography and calibration against cardiac catheterization," *Investigative Radiology*, vol. 44, no. 6, pp. 360–368, 2009.
- [33] V. Delgado, A. C. T. Ng, J. D. Schuijf et al., "Automated assessment of the aortic root dimensions with multidetector row computed tomography," *Annals of Thoracic Surgery*, vol. 91, no. 3, pp. 716–723, 2011.

Review Article

The Fetal Modified Myocardial Performance Index: Is Automation the Future?

Priya Maheshwari,¹ Amanda Henry,^{1,2,3,4} and Alec W. Welsh^{1,2,4}

¹Faculty of Medicine, School of Women's & Children's Health, University of New South Wales, Sydney, NSW 2052, Australia

²Department of Maternal-Fetal Medicine, Royal Hospital for Women, Locked Bag 2000, Barker Street, Randwick, NSW 2031, Australia

³Women's and Children's Health, St George Hospital, Kogarah, NSW 2217, Australia

⁴Australian Centre for Perinatal Science, University of New South Wales, Sydney, NSW 2052, Australia

Correspondence should be addressed to Alec W. Welsh; alec.welsh@unsw.edu.au

Received 15 August 2014; Accepted 28 September 2014

Academic Editor: Marco Francone

Copyright © 2015 Priya Maheshwari et al. This is an open access article distributed under the Creative Commons Attribution License, which permits unrestricted use, distribution, and reproduction in any medium, provided the original work is properly cited.

The fetal modified myocardial performance index (Mod-MPI) is a noninvasive, pulsed-wave Doppler-derived measure of global myocardial function. This review assesses the progress in technical refinements of its measurement and the potential for automation to be the crucial next step. The Mod-MPI is a ratio of isovolumetric to ejection time cardiac time intervals, and the potential for the left ventricular Mod-MPI as a tool to clinically assess fetal cardiac function is well-established. However, there are wide variations in published reference ranges, as (1) a standardised method of selecting cardiac time intervals used in Mod-MPI calculation has not been established; (2) cardiac time interval measurement currently requires manual, inherently subjective placement of callipers on Doppler ultrasound waveforms; and (3) ultrasound machine settings and ultrasound system type have been found to affect Mod-MPI measurement. Collectively these factors create potential for significant inter- and intraobserver measurement variability. Automated measurement of the Mod-MPI may be the next key development which propels the Mod-MPI into routine clinical use. A novel automated system of Mod-MPI measurement is briefly presented and its implications for the future of the Mod-MPI in fetal cardiology are discussed.

1. Introduction

Fetal echocardiography has developed over the past 30 years as the primary noninvasive modality used to evaluate fetal cardiac anatomy, haemodynamics, and function [1]. Functional cardiac assessment using echocardiography is becoming increasingly valued because it facilitates the detection of subtle myocardial dysfunction during development and can guide management and improve neonatal outcomes [2]. Early intervention can prevent progression into intrauterine cardiac failure [3].

The myocardial performance index (MPI) is a noninvasive pulsed-wave Doppler-derived measure of global myocardial function which has been evaluated in fetal cardiology and is a ratio of isovolumetric to ejection time cardiac time intervals [1]. However, its clinical applications have been limited

due to its poor reproducibility [4]. This review charts the development of this index as applied to the fetus and progress in technical refinements of its measurement, with particular focus on developments since the introduction and acceptance in 2005 of the modified-MPI, or Mod-MPI [5]. The Mod-MPI was defined using specific methodology for measuring the time periods required in fetal MPI calculation.

2. Development of the Pulsed-Wave Doppler Derived Myocardial Performance Index (MPI)

The MPI was first described for adult cardiac evaluation in cases of dilated cardiomyopathy in 1995 by Tei et al. [7]. Originally known as the Tei Index but later termed the MPI,

it is traditionally a pulsed-wave derived index which incorporates measurement of cardiac time intervals and is defined as follows [8]:

$$\begin{aligned} \text{MPI} = & (\text{isovolumetric contraction time (ICT)} \\ & + \text{isovolumetric relaxation time (IRT)}) \quad (1) \\ & \times (\text{ejection time (ET)})^{-1}. \end{aligned}$$

Both atrioventricular and ventricular ejection flows are evaluated to determine constituent time intervals. The ICT represents the time when myocardial contraction causes increased intraventricular pressure without an accompanying change in ventricular volume since all valves are closed during this phase [9]. The IRT refers to the postsystolic myocardial relaxation that occurs as calcium reuptake begins in cardiomyocytes, which decreases intraventricular pressure since no blood is entering or leaving the ventricles [9]. The ET starts when the ventricular pressure is raised sufficiently to open the aortic/pulmonary valves, causing the myocardium to deform and for blood to be ejected from the ventricle [10].

Myocardial dysfunction results in increased MPI values, predominantly due to a prolongation of the IRT although often accompanied by a reduced ET [1]. Calcium reuptake in cardiomyocytes is suppressed during cardiac functional deterioration which extends the time required for the myocardium to fully relax [11], and the IRT is the main MPI parameter to become abnormal early in cardiac dysfunction [10].

The MPI has been demonstrated to correlate well with other invasive and noninvasive measures of left ventricular function in adults [12]. Pulsed-wave Doppler-derived MPI was validated and became widely used as a quantitative measure of global cardiac function first in adults and then in the paediatric population [13–15]. The MPI is a particularly valuable index because precise anatomical imaging is not necessary in order to measure the MPI and it is independent of heart rate, blood pressure, and ventricular shape because the index only incorporates time intervals [7, 16, 17]. The fact that it is relatively easily measurable and can be incorporated into a routine ultrasound examination adds to its utility in the fetal context [18].

3. Application of the MPI to Fetal Cardiac Evaluation

Tsutsumi et al. in 1999 were the first to report the use of the MPI to evaluate global myocardial function in fetuses, using two waveforms and therefore two cardiac cycles [17]. Subsequent studies demonstrated a wide variability in normal reference values, likely contributed to by the lack of clear landmarks in the Doppler waveforms to calculate time intervals and the possible impacts of fetal heart rate variation between the two waveforms [7, 19, 20]. Measurement using two cardiac cycles also meant that individual measurements of the ICT and IRT could not be made.

Friedman et al. proposed a new position for the Doppler sample volume in 2003 which enabled the left ventricular

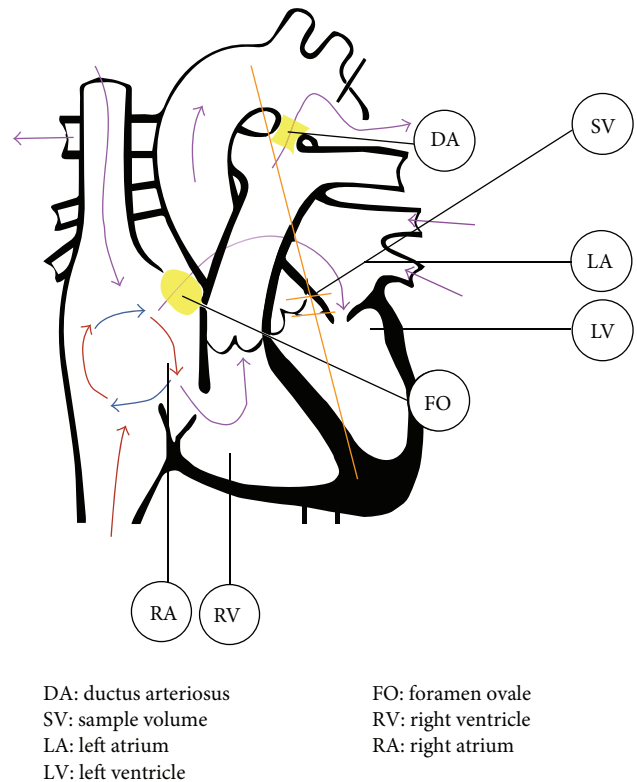


FIGURE 1: Positioning of the Doppler sample volume for acquisition of the left MPI. Modified from OpenStax College (2013) [6].

MPI to be evaluated from a single Doppler waveform [1]. Close proximity of the mitral inflow and aortic outflow tracts in the fetal heart allowed isovolumetric periods and ejection time to each be recorded simultaneously within the same cardiac cycle (see Figure 1).

The opening and closing of valve leaflets produces Doppler echoes or “clicks,” seen as vertical stripes on the Doppler waveform. The methodology for calculating the left MPI was further modified by Raboisson et al. in 2003 when they proposed that the Doppler click of the aortic valve opening be used as a landmark in order to better estimate the time intervals of MPI calculation [21].

In 2005, Hernandez-Andrade et al. introduced the modified MPI (Mod-MPI) using the beginning of opening and closing Doppler clicks of both the aortic and mitral valves as measurement landmarks for determination of the different time periods (see Figures 2 and 3) [5]. This significantly reduced the inter- and intraobserver variability and thus improved reproducibility of the index in fetal medicine. For the left Mod-MPI, the Doppler sample gate was placed on the lateral wall of the ascending aorta close to the mitral valve in an apical four-chamber view of the fetal heart, as shown in Figures 1 and 2 [5].

The MPI has been used to demonstrate fetal cardiac dysfunction in a number of pathological conditions, including intrauterine growth restriction [17, 22–25], maternal diabetes [26–30], twin-twin transfusion syndrome (TTTS) [31–34],

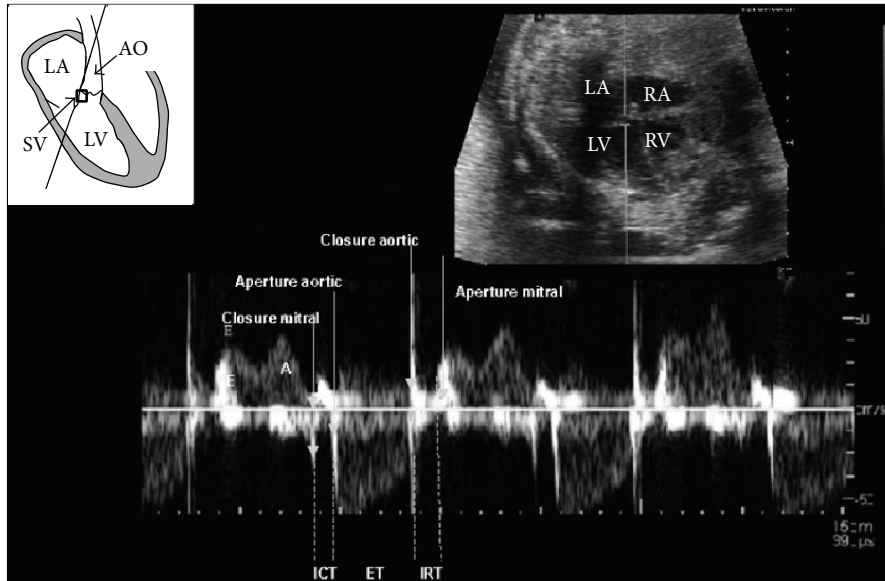


FIGURE 2: The schematic diagram at top left shows placement of the Doppler sample volume (SV) in left Mod-MPI measurement. The corresponding Doppler waveform is shown at bottom and the 2D echocardiograph is at top right. LV: left ventricle; LA: left atrium; RV: right ventricle; RA: right atrium; AO: aortic outflow tract; adapted from Hernandez-Andrade et al. (2005) [5].

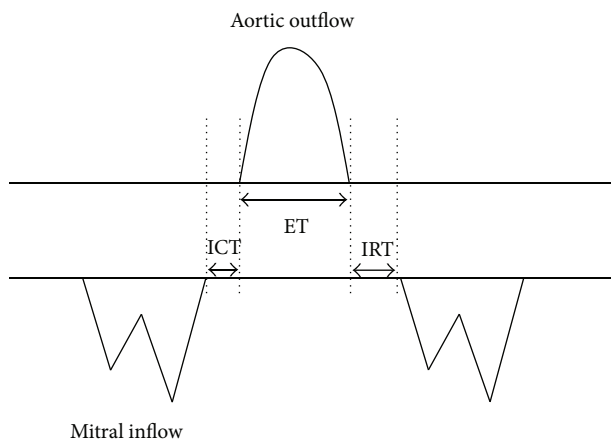


FIGURE 3: Time interval measurements are based upon the echoes from valve movements.

congenital heart malformations [35–39], preeclampsia [40], and other fetal conditions [41–44].

Figure 4 summarises the developments leading to the Mod-MPI, and it also highlights the direction of research since then which will be analysed in the subsequent sections of this review.

4. Varied Measurements between Research Groups

Manual placement of a time calliper on the Doppler waveform is used to measure the time intervals between various clicks. Minor variations in calliper placement and hence

alterations of mere milliseconds in time interval measurements result in significantly different Mod-MPIs [47]. For example, an alteration of only 4 milliseconds in constituent components of the MPI results in a variation in MPI of approximately $\pm 12\text{--}14\%$ [48].

A lack of consensus on calliper placement between research groups has likely contributed to the wide range of values (0.35–0.60) for quoted “normal” Mod-MPIs in singleton fetuses [1, 17–19, 45, 47, 49–52]. Some authors describe almost constant left MPI measurements throughout pregnancy, whilst others report gradual increases or decreases in mean MPI (Figure 5). These factors have restricted the translational potential of the MPI, as while individual research groups have demonstrated significant differences between their pathological subgroups and controls [24, 28, 49, 53], the lack of a universal reference range makes meaningful comparison of pathological findings between research groups impractical.

5. Technical Considerations

5.1. Calliper Placement. The opening and closing of valve leaflets produces “original” Doppler clicks in the same direction as blood flow (for opening clicks) or opposite direction to flow (for closing clicks). Smaller Doppler echoes may be present in the opposite direction to the original clicks, termed “reflected” clicks (see Figures 6 and 7) [4]. The original and reflected clicks share a common peak time point, and it is suggested that thinner clicks enable more precise measurement [4].

Although the first normal range for fetal MPI was established using calliper positioning at the beginning (just before the echo) of the valve click [5], the criteria for demarcation

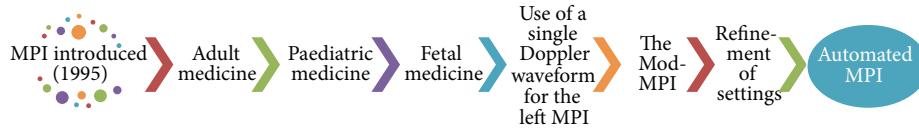


FIGURE 4: The main stages of evolution of the MPI since 1995.

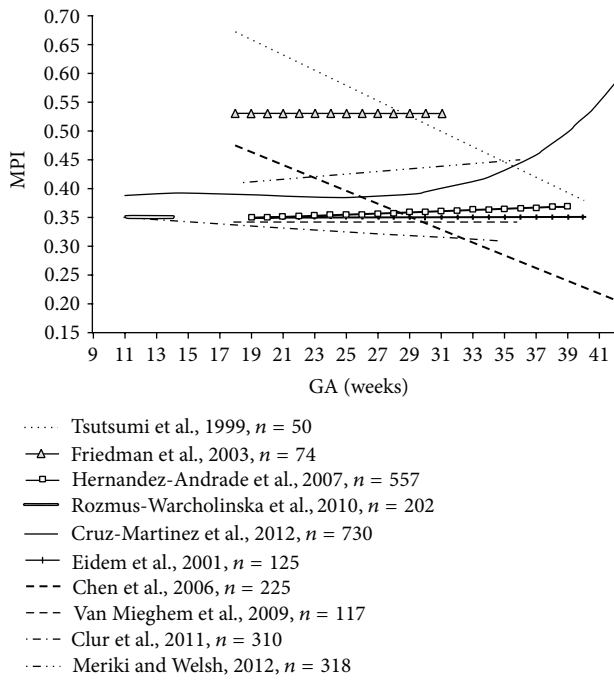
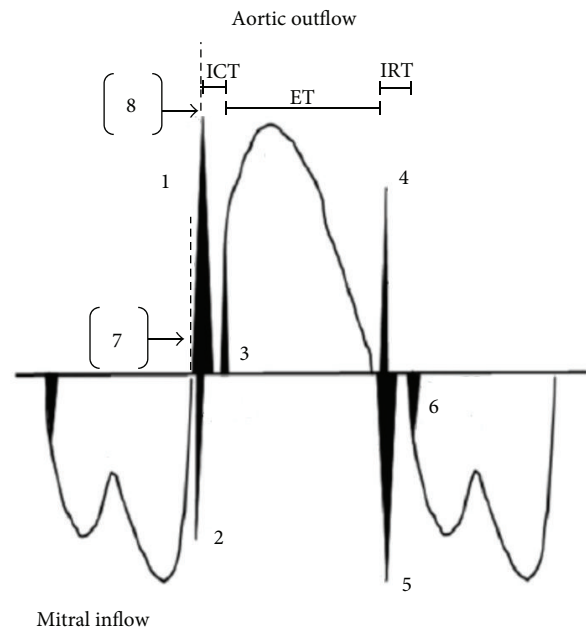


FIGURE 5: Gestational age-adjusted mean values for fetal left MPI in studies published from 1999 to 2012; adapted from Cruz-Martinez et al. (2012) [45, 46].



Note. Mitral valve: MV; aortic valve: AV.

- (1) Original MV closure click [1]
- (2) Reflected MV closure click
- (3) Original AV opening click
- (4) Reflected AV closure click
- (5) Original AV closure click
- (6) Original MV opening click
- (7) Beginning of [1]
- (8) Peak of [1]

FIGURE 7: Schematic representation of valve clicks for the left Mod-MPI Doppler waveform, with a focus for time intervals on the original mitral valve closure click for simplicity; adapted from Meriki and Welsh [47].

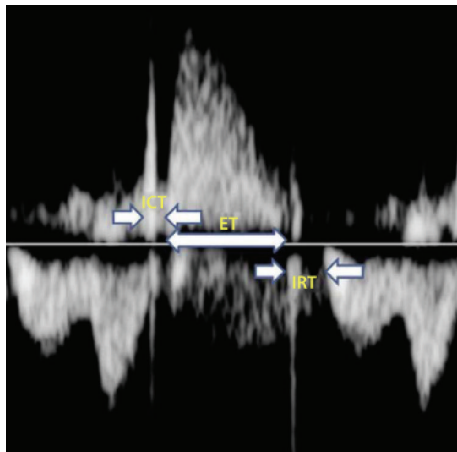


FIGURE 6: Left Mod-MPI Doppler waveform, showing the time intervals [47].

of time intervals according to valve clicks are conflicting between subsequent studies. Some position callipers from the end of one click to the beginning of the next, corresponding to physiological time intervals as the period of valve movement is not included in ICT and IRT calculations [49]. A number of studies have failed to define a methodology for demarcating time intervals [28, 50, 51]. Other studies have positioned the calliper at the peak of valve clicks (see Figure 7) [47]. This is a clearer landmark that overcomes variations in valve click widths, though it does not absolutely correlate with the physiological time periods because the valves open at the start and close at the end of valve clicks. However, it has higher repeatability than the original method and it overcomes the limitations created by clicks of varying widths and therefore is likely to be a more useful method [54].

TABLE 1: Technique and machine settings used in various studies (adapted from Mahajan et al., in press [46]).

	Angle of insonation (°)	WMF (Hz)	Sample volume (mm)	Sweep velocity (cm/s)	Doppler gain	Placement of time cursor
Tei, 1995 [8]	ND	ND	ND	10	ND	Beginning of mitral inflow and aortic outflow waveforms.
Hernandez-Andrade et al., 2005 [5]	<30	70	3	15	Min.	Beginning of valve clicks.
Van Mieghem et al., 2009 [49]	<15	≥120	ND	10	ND	End of closing clicks to beginning of opening clicks.
Meriki et al., 2012 [48]	<15	300	3	15	Min.	Peak of valve clicks.
Lobmaier et al., 2014 for Siemens Antares machine* [56]	<15	281	4	15	60 dB	Beginning of valve clicks.
Lobmaier et al., 2014 for Voluson 730 Expert machine* [56]	<15	210	4	15	-10 dB	Beginning of valve clicks.

WMF: wall motion filter; ND: not defined; min.: minimum.

*Values displayed are the “optimal settings” for each ultrasound machine trialled in this study, as various settings were compared.

5.2. Machine Settings and Acquisition Technique. Hernandez-Andrade et al. described optimal settings as summarised in row 2 of Table 1 and suggested use of the fastest possible sweep velocity [55]. Higher sweep velocities create greater horizontal “stretch,” with clearer visualisation of valve clicks for more accurate time interval measurement. Low Doppler gain and a high-pass wall motion filter (WMF) were suggested in order to limit artefacts and noise and enable more precise recognition of clicks [55]. Meriki et al. further defined a fixed WMF at 300 Hz as providing improved repeatability and additionally stated that the angle of insonation should be kept less than 15° and Doppler aliasing avoided [48].

Lobmaier et al. have since investigated the impact on left Mod-MPI values of differing ultrasound settings (namely, sweep speed, gain, and WMF) and equipment [56]. They are the first to investigate the effect of using different equipment on Mod-MPI calculation and repeatability of measurement, specifically by comparing Mod-MPI values obtained from the Siemen Antares and Voluson 730 Expert ultrasound machines.

Lobmaier et al. concluded that raised sweep velocities and WMF resulted in superior measurement repeatability because of the association of those settings with higher intraclass correlation coefficients (ICCs), although optimal machine settings differ between manufacturers. Their results and the settings used by other groups are summarised in Table 1 [56]. In future research similar methodology needs to be applied to optimising MPI settings for different machines, which may result in different reference ranges depending on machine type used.

6. Automation of the MPI

The establishment of universal agreement for machine settings does not appear too distant if future studies can build on the findings of Lobmaier et al. [56]. Lack of a standardised

method of selecting cardiac time intervals for Mod-MPI calculation remains another key barrier to the development of a universal reference range to replace the various gestation-adjusted normal ranges published to date. There is an inherent subjectivity in manual selection of time points for measurement of cardiac time intervals, as reflected by ICCs of 0.8-0.9 when intra- and interobserver variability of Mod-MPI calculation is studied, even when calculation is performed by experienced operators using stringent, predefined criteria [47, 54]. With machine settings now having been optimised, we feel that the automated measurement of the Mod-MPI is the crucial next step towards the development of the Mod-MPI as a routinely utilised clinical tool.

We have developed a novel automated MPI system in a collaboration between fetal medicine practitioners and biomedical engineers [57]. The automation algorithm automatically locates valve click peaks and calculates the Mod-MPI using the morphological characteristics of the aortic and mitral flow in the Doppler ultrasound waveform and the intensity signals (or “brightness”) from waveform images [57]. Repeatability of the fetal left Mod-MPI when obtained using this automated system for fetal Mod-MPI measurement and a comparison with manual measurement have been the focus of recent research. Preliminary data suggest that Mod-MPI automation is sensitive, precise, and feasible when compared to an experienced human observer’s acquisition of Mod-MPI values [57]. Our automation system is in the process of being internationally tested with the intention of ultimately open sourcing the algorithm.

Lee et al. have also proposed a system of automatically measuring the Mod-MPI [58]. Their Auto Mod-MPI system (Samsung Electronics Co. Ltd., Suwon, South Korea) detects valve clicks using a methodology which first requires the operator to manually select a region of interest in the Doppler waveform before any further image analysis can take place [59]. In comparison, our automated MPI system does not

require manual selection of a region of interest, instead it analyses the entire image automatically. The valve clicks in our automated MPI system are found by a weighted sum of various signals in the region surrounding the valve click. Whilst both automation systems use the morphology of the waveform to identify the clicks, our system also uses intensity information of the image for identification of all four valve clicks. This is only possible for two of the four clicks in the automation system proposed by Yoon et al. [59]. Further, our automation system localises valve clicks independently of each other rather than sequentially [60].

Multiple groups have found that the IRT is the cardiac time interval for which repeatability has been demonstrated to be the poorest [54, 56] which is important because the IRT is often the first time interval to be affected in cardiac dysfunction [10]. The morphological characteristics of the mitral valve opening include lack of a reflected click and tendency for the valve opening to be thick and tilted [47]. This is an additional reason why the subjectivity in operator-dependent calliper placement is likely to be the major source of measurement imprecision and contributor to interoperator measurement variability, especially for the IRT but to a lesser extent the other time intervals. Automation of the Mod-MPI may facilitate the incorporation of the MPI as a routine measure of fetal cardiac function by removing the significant subjective component of manual calliper placement for measurement of the constituent time intervals.

Further, manual calculation is time-consuming and requires highly trained staff. An average of 65 fetal MPI measurements is required to attain competence at producing reliable measurements [61]. Automated calculation of the Mod-MPI is likely to significantly reduce the amount of time needed for a Mod-MPI value to be generated and facilitate Mod-MPI signal capture amongst sonographers with limited expertise in Mod-MPI acquisition [57]. If automated Mod-MPI proves to be readily applicable to the clinical setting, the subsequently generated automated Mod-MPI normal values will provide a universal reference range to replace the multiple prior manually derived ranges. This in turn will allow definitive assessment of whether differences in Mod-MPI values in pathological subgroups versus uncomplicated controls are sufficient for Mod-MPI to translate from research tool to clinical utility.

7. A Note on the Right Heart MPI

Progressive refinement of left Mod-MPI measurement has been facilitated by the fact that only a single waveform is required [1, 5, 48]. The Mod-MPI for the right heart has traditionally been a slightly more cumbersome measure. This is because the tricuspid and pulmonary valves are located in differing anatomical planes so that two waveforms from two different planes have been necessary for right Mod-MPI calculation, and the waveforms have not been obtainable from the same cardiac cycle [5]. Hernandez-Andrade et al. suggested that small potential variations in the fetal heart rate between recordings of the two waveforms could affect the reproducibility of the right Mod-MPI, although the degree of heart

rate variation sufficient to impact reproducibility is uncertain. This concern regarding reproducibility may have contributed to most MPI research focusing on the left ventricle rather than the right in normal and pathological pregnancies following the introduction of the Mod-MPI [26, 40, 48, 62].

However, Meriki et al. have since demonstrated similar reproducibility of left and right MPI [54]. The right MPI is considered an important parameter because the fetus is right-heart dominant [63]. Furthermore, the right MPI may provide an earlier indication of the development of pathology because changes in right heart function precede changes in left heart function in the context of pathology such as TTTS [54]. Recently we have found that the right MPI can be acquired using a single plane, single waveform technique in fetuses until approximately 26 weeks of gestation when the tricuspid and pulmonary valves diverge (unpublished data). Thus earlier in pregnancy, a fetal right Mod-MPI may be derivable from a waveform identical to that which is currently used for left Mod-MPI calculation. This will allow an automated process to calculate the right Mod-MPI in the same way as for the left, thereby increasing the ease of clinical application and utility of the right Mod-MPI.

8. Conclusion

The MPI is a noninvasive marker of global myocardial function and a sensitive tool for detecting fetal cardiac dysfunction. Its translational potential is now mainly constrained by the lack of standardised methodology for demarcation of the time periods used in its calculation and the need for improvement of its repeatability and ease of measurement. Since the introduction of the Mod-MPI, various studies have been necessary to evaluate technical refinements in order to standardise its measurement. Automation of the measurement process may be considered as the next logical step towards unification of the Mod-MPI measurement process, and we hope towards its role as a cornerstone of functional fetal echocardiography.

Conflict of Interests

The authors declare that there is no conflict of interests regarding the publication of this paper.

Acknowledgment

The authors would like to thank Jingjing Wang from the UNSW Graduate School of Biomedical Engineering for her assistance in developing a simplified explanation of their automated MPI system.

References

- [1] D. Friedman, J. Buyon, M. Kim, and J. S. Glickstein, "Fetal cardiac function assessed by Doppler myocardial performance index (Tei index)," *Ultrasound in Obstetrics & Gynecology*, vol. 21, no. 1, pp. 33–36, 2003.

- [2] A. J. Moon-Grady, S. Hirose, G. Kesby, S. Menahem, and W. Tworetzky, "The fetus as a cardiac patient: assessment and therapy of cardiovascular pathology before birth," *International Journal of Pediatrics*, vol. 2010, Article ID 974520, 2 pages, 2010.
- [3] S. Balasubramanian and T. A. Tacy, "Functional imaging in fetal echocardiography: a review of conventional and novel approaches," *Cardiovascular Engineering and Technology*, vol. 4, no. 3, pp. 276–285, 2013.
- [4] N. Meriki and A. W. Welsh, "Technical considerations for measurement of the fetal left modified myocardial performance index," *Fetal Diagnosis and Therapy*, vol. 31, no. 1, pp. 76–80, 2012.
- [5] E. Hernandez-Andrade, J. Lopez-Tenorio, H. Figueroa-Diesel et al., "A modified myocardial performance (Tei index) based on the use of valve clicks improves reproducibility of fetal left cardiac function assessment," *Ultrasound in Obstetrics & Gynecology*, vol. 26, no. 3, pp. 227–232, 2005.
- [6] Open Stax College, *2916 Fetal Circulatory System-02*, Licensed under Creative Commons Attribution-Share Alike 3.0 via Wikimedia Commons, 2013, http://commons.wikimedia.org/wiki/File:2916_Fetal_Circulatory_System-02.jpg#mediaviewer/File:2916_Fetal_Circulatory_System-02.jpg.
- [7] C. Tei, L. H. Ling, D. O. Hodge et al., "New index of combined systolic and diastolic myocardial performance: a simple and reproducible measure of cardiac function—a study in normals and dilated cardiomyopathy," *Journal of Cardiology*, vol. 26, no. 6, pp. 357–366, 1995.
- [8] C. Tei, "New non-invasive index for combined systolic and diastolic ventricular function," *Journal of Cardiology*, vol. 26, no. 2, pp. 135–136, 1995.
- [9] A. C. Guyton and J. E. Hall, *Guyton and Hall Textbook of Medical Physiology*, Elsevier Saunders, Philadelphia, Pa, USA, 12th edition, 2011.
- [10] F. Crispi and E. Gratacs, "Fetal cardiac function: technical considerations and potential research and clinical applications," *Fetal Diagnosis and Therapy*, vol. 32, no. 1-2, pp. 47–64, 2012.
- [11] V. A. Browne, V. M. Stiffel, W. J. Pearce, L. D. Longo, and R. D. Gilbert, "Activator calcium and myocardial contractility in fetal sheep exposed to long-term high-altitude hypoxia," *American Journal of Physiology—Heart and Circulatory Physiology*, vol. 272, no. 3, pp. H1196–H1204, 1997.
- [12] C. Tei, R. A. Nishimura, J. B. Seward, and A. J. Tajik, "Noninvasive doppler-derived myocardial performance index: correlation with simultaneous measurements of cardiac catheterization measurements," *Journal of the American Society of Echocardiography*, vol. 10, no. 2, pp. 169–178, 1997.
- [13] M. Ishii, G. Eto, C. Tei et al., "Quantitation of the global right ventricular function in children with normal heart and congenital heart disease: a right ventricular myocardial performance index," *Pediatric Cardiology*, vol. 21, no. 5, pp. 416–421, 2000.
- [14] S. J. Mooradian, C. S. Goldberg, D. C. Crowley, and A. Ludomirsky, "Evaluation of a noninvasive index of global ventricular function to predict rejection after pediatric cardiac transplantation," *American Journal of Cardiology*, vol. 86, no. 3, pp. 358–360, 2000.
- [15] K. Ichihashi, Y. Yada, N. Takahashi, Y. Honma, and M. Momoi, "Utility of a Doppler-derived index combining systolic and diastolic performance (Tei index) for detecting hypoxic cardiac damage in newborns," *Journal of Perinatal Medicine*, vol. 33, no. 6, pp. 549–552, 2005.
- [16] B. W. Eidem, C. Tei, P. W. O'Leary, F. Cotta, and J. B. Seward, "Nongeometric quantitative assessment of right and left ventricular function: myocardial performance index in normal children and patients with Ebstein anomaly," *Journal of the American Society of Echocardiography*, vol. 11, no. 9, pp. 849–856, 1998.
- [17] T. Tsutsumi, M. Ishii, G. Eto, M. Hota, and H. Kato, "Serial evaluation for myocardial performance in fetuses and neonates using a new Doppler index," *Pediatrics International*, vol. 41, no. 6, pp. 722–727, 1999.
- [18] C. B. Falkensammer, J. Paul, and J. C. Huhta, "Fetal congestive heart failure: correlation of Tei index and cardiovascular-score," *Journal of Perinatal Medicine*, vol. 29, no. 5, pp. 390–398, 2001.
- [19] B. W. Eidem, J. M. Edwards, and F. Cetta, "Quantitative assessment of fetal ventricular function: establishing normal values of the myocardial performance index in the fetus," *Echocardiography*, vol. 18, no. 1, pp. 9–13, 2001.
- [20] K. Ichizuka, R. Matsuoka, J. Hasegawa et al., "The Tei index for evaluation of fetal myocardial performance in sick fetuses," *Early Human Development*, vol. 81, no. 3, pp. 273–279, 2005.
- [21] M.-J. Raboisson, M. Bourdages, and J.-C. Fouron, "Measuring left ventricular myocardial performance index in fetuses," *American Journal of Cardiology*, vol. 91, no. 7, pp. 919–921, 2003.
- [22] K. Niewiadomska-Jarosik, E. Lipecka-Kidawska, U. Kowalska-Koprek et al., "Assessment of cardiac function in fetuses with intrauterine growth retardation using the Tei index," *Developmental Period Medicine*, vol. 9, no. 2, pp. 153–160, 2005.
- [23] A. Benavides-Serralde, M. Scheier, R. Cruz-Martinez et al., "Changes in central and peripheral circulation in intrauterine growth-restricted fetuses at different stages of umbilical artery flow deterioration: new fetal cardiac and brain parameters," *Gynecologic and Obstetric Investigation*, vol. 71, no. 4, pp. 274–280, 2011.
- [24] M. Comas, F. Crispi, R. Cruz-Martinez, J. M. Martinez, F. Figueras, and E. Gratacós, "Usefulness of myocardial tissue Doppler vs conventional echocardiography in the evaluation of cardiac dysfunction in early-onset intrauterine growth restriction," *American Journal of Obstetrics & Gynecology*, vol. 203, no. 1, pp. 45.e1–45.e7, 2010.
- [25] F. Crispi, E. Hernandez-Andrade, M. M. Pellers et al., "Cardiac dysfunction and cell damage across clinical stages of severity in growth-restricted fetuses," *American Journal of Obstetrics & Gynecology*, vol. 199, no. 3, pp. 254.e1–254.e8, 2008.
- [26] J. Garcia-Flores, M. Jañez, M. C. Gonzalez, N. Martinez, M. Espada, and A. Gonzalez, "Fetal myocardial morphological and functional changes associated with well-controlled gestational diabetes," *European Journal of Obstetrics Gynecology and Reproductive Biology*, vol. 154, no. 1, pp. 24–26, 2011.
- [27] M. L. Wong, W. H. S. Wong, and Y. F. Cheung, "Fetal myocardial performance in pregnancies complicated by gestational impaired glucose tolerance," *Ultrasound in Obstetrics & Gynecology*, vol. 29, no. 4, pp. 395–400, 2007.
- [28] N. E. Russell, M. Foley, B. T. Kinsley, R. G. Firth, M. Coffey, and F. M. McAuliffe, "Effect of pregestational diabetes mellitus on fetal cardiac function and structure," *American Journal of Obstetrics & Gynecology*, vol. 199, no. 3, pp. 312.e1–312.e7, 2008.
- [29] K. Campbell, S. Thung, C. Buhimschi, J. Copel, and O. Bahtiyar, "OP16.02: the Tei index to assess myocardial performance in fetuses of diabetic mothers," *Ultrasound in Obstetrics & Gynecology*, vol. 38, no. S1, p. 101, 2011.

- [30] N. Russell, M. Foley, and F. McAuliffe, "First trimester fetal cardiac function—is there a difference between the diabetic and non-diabetic population?" *American Journal of Obstetrics & Gynecology*, vol. 195, no. 6, p. S137, 2006.
- [31] T. Van Mieghem, P. Klaritsch, E. Doné et al., "Assessment of fetal cardiac function before and after therapy for twin-to-twin transfusion syndrome," *American Journal of Obstetrics & Gynecology*, vol. 200, no. 4, pp. 400.e1–400.e7, 2009.
- [32] J. J. Stirnemann, M. Mougeot, F. Proulx et al., "Profiling fetal cardiac function in twin-twin transfusion syndrome," *Ultrasound in Obstetrics & Gynecology*, vol. 35, no. 1, pp. 19–27, 2010.
- [33] M. J. Raboisson, J. C. Fouron, J. Lamoureux et al., "Early inter-twin differences in myocardial performance during the twin-to-twin transfusion syndrome," *Circulation*, vol. 110, no. 19, pp. 3043–3048, 2004.
- [34] M. Habli, E. Michelfelder, J. Livingston et al., "Acute effects of selective fetoscopic laser photocoagulation on recipient cardiac function in twin-twin transfusion syndrome," *American Journal of Obstetrics & Gynecology*, vol. 199, no. 4, pp. 412.e1–412.e6, 2008.
- [35] Y. Chen, G. Lv, B. Li, and Z. Wang, "Cerebral vascular resistance and left ventricular myocardial performance in fetuses with ebstein's anomaly," *The American Journal of Perinatology*, vol. 26, no. 4, pp. 253–258, 2009.
- [36] A. Szwest, Z. Tian, M. McCann, D. Donaghue, and J. Rychik, "Right ventricular performance in the fetus with hypoplastic left heart syndrome," *Annals of Thoracic Surgery*, vol. 87, no. 4, pp. 1214–1219, 2009.
- [37] N. Inamura, M. Taketazu, J. F. Smallhorn, and L. K. Hornberger, "Left ventricular myocardial performance in the fetus with severe tricuspid valve disease and tricuspid insufficiency," *The American Journal of Perinatology*, vol. 22, no. 2, pp. 91–97, 2005.
- [38] N. Inamura, Y. Kado, T. Nakajima, and F. Kayatani, "Left and right ventricular function in fetal tetralogy of fallot with absent pulmonary valve," *The American Journal of Perinatology*, vol. 22, no. 4, pp. 199–204, 2005.
- [39] S. A. Clur, A. C. van der Wal, J. Ottenkamp, and C. M. Bilardo, "Echocardiographic evaluation of fetal cardiac function: clinical and anatomical correlations in two cases of endocardial fibroelastosis," *Fetal Diagnosis and Therapy*, vol. 28, no. 1, pp. 51–57, 2010.
- [40] O. Api, M. Balcin Emeksiz, M. Api, V. Ugurel, and O. Unal, "Modified myocardial performance index for evaluation of fetal cardiac function in pre-eclampsia," *Ultrasound in Obstetrics & Gynecology*, vol. 33, no. 1, pp. 51–57, 2009.
- [41] Y. Mori, M. J. Rice, R. W. McDonald et al., "Evaluation of systolic and diastolic ventricular performance of the right ventricle in fetuses with ductal constriction using the Doppler Tei index," *The American Journal of Cardiology*, vol. 88, no. 10, pp. 1173–1178, 2001.
- [42] A. L. L. Müller, P. M. Barrios, L. M. Kliemann, E. G. Valério, R. Gasnier, and J. A. Magalhães, "Tei index to assess fetal cardiac performance in fetuses at risk for fetal inflammatory response syndrome," *Ultrasound in Obstetrics & Gynecology*, vol. 36, no. 1, pp. 26–31, 2010.
- [43] T. Van Mieghem, L. Gucciardo, E. Doné et al., "Left ventricular cardiac function in fetuses with congenital diaphragmatic hernia and the effect of fetal endoscopic tracheal occlusion," *Ultrasound in Obstetrics & Gynecology*, vol. 34, no. 4, pp. 424–429, 2009.
- [44] A. Szwest, Z. Tian, M. McCann et al., "Impact of altered loading conditions on ventricular performance in fetuses with congenital cystic adenomatoid malformation and twin-twin transfusion syndrome," *Ultrasound in Obstetrics & Gynecology*, vol. 30, no. 1, pp. 40–46, 2007.
- [45] R. Cruz-Martinez, F. Figueras, M. Bennasar et al., "Normal reference ranges from 11 to 41 weeks' gestation of fetal left modified myocardial performance index by conventional doppler with the use of stringent criteria for delimitation of the time periods," *Fetal Diagnosis and Therapy*, vol. 32, no. 1-2, pp. 79–86, 2012.
- [46] A. Mahajan, A. Henry, N. Meriki et al., "The (Pulsed-Wave) Doppler fetal myocardial performance index: technical challenges, clinical applications and future research," *Fetal Diagnosis and Therapy*. In press.
- [47] N. Meriki and A. W. Welsh, "Development of australian reference ranges for the left fetal modified myocardial performance index and the influence of caliper location on time interval measurement," *Fetal Diagnosis and Therapy*, vol. 32, no. 1-2, pp. 87–95, 2012.
- [48] N. Meriki, A. Izurieta, and A. W. Welsh, "Fetal left modified myocardial performance index: technical refinements in obtaining pulsed-Doppler waveforms," *Ultrasound in Obstetrics & Gynecology*, vol. 39, no. 4, pp. 421–429, 2012.
- [49] T. Van Mieghem, L. Gucciardo, P. Lewi et al., "Validation of the fetal myocardial performance index in the second and third trimesters of gestation," *Ultrasound in Obstetrics & Gynecology*, vol. 33, no. 1, pp. 58–63, 2009.
- [50] S. A. B. Clur, K. O. Rengerink, B. W. J. Mol, J. Ottenkamp, and C. M. Bilardo, "Fetal cardiac function between 11 and 35 weeks' gestation and nuchal translucency thickness," *Ultrasound in Obstetrics & Gynecology*, vol. 37, no. 1, pp. 48–56, 2011.
- [51] W. Rozmus-Warcholinska, A. Wloch, G. Acharya et al., "Reference values for variables of fetal cardiocirculatory dynamics at 11–14 weeks of gestation," *Ultrasound in Obstetrics & Gynecology*, vol. 35, no. 5, pp. 540–547, 2010.
- [52] Q. Chen, X.-F. Sun, and H.-J. Liu, "Assessment of myocardial performance in fetuses by using Tei index," *Chinese Journal of Obstetrics and Gynecology*, vol. 41, no. 6, pp. 387–390, 2006.
- [53] K. Ichizuka, R. Matsuoka, J. Hasegawa, and T. Okai, "OP39.07: the Tei index in FGR fetus," *Ultrasound in Obstetrics & Gynecology*, vol. 36, no. S1, p. 166, 2010.
- [54] N. Meriki, A. Izurieta, and A. Welsh, "Reproducibility of constituent time intervals of right and left fetal modified myocardial performance indices on pulsed Doppler echocardiography: a short report," *Ultrasound in Obstetrics & Gynecology*, vol. 39, no. 6, pp. 654–658, 2012.
- [55] E. Hernandez-Andrade, H. Figueroa-Diesel, C. Kottman et al., "Gestational-age-adjusted reference values for the modified myocardial performance index for evaluation of fetal left cardiac function," *Ultrasound in Obstetrics & Gynecology*, vol. 29, no. 3, pp. 321–325, 2007.
- [56] S. Lobmaier, M. Cruz-Lemini, B. Valenzuela-Alcaraz et al., "Influence of equipment and settings on myocardial performance index repeatability and definition of settings to achieve optimal reproducibility," *Ultrasound in Obstetrics & Gynecology*, vol. 43, no. 6, pp. 632–639, 2014.
- [57] J. Wang, A. Henry, S. Redmond, and A. Welsh, "OC08.02: automation of the fetal myocardial performance index," *Ultrasound in Obstetrics & Gynecology*, vol. 44, no. S1, p. 18, 2014.
- [58] M. Y. Lee, H. S. Won, E. J. Jeon et al., "Feasibility of using Auto Mod-MPI system, a novel technique for the automated

- measurement of the fetal modified myocardial performance index,” *Ultrasound in Obstetrics & Gynecology*, vol. 43, no. 6, pp. 640–645, 2014.
- [59] H. Yoon, H. Lee, K.-W. Jeon et al., “Automated measurement of fetal myocardial performance index in ultrasound Doppler waveforms,” in *Medical Imaging 2014: Ultrasonic Imaging and Tomography*, vol. 9040 of *Proceedings of SPIE*, 90401E, p. 8, February 2014.
- [60] H. C. Yoon, H. Lee, and H. Jung, “Image processing method and apparatus,” European Patent Application number: 13163808.2 , European Patent Office, 2013.
- [61] R. Cruz-Martinez, F. Figueras, J. J. Jaramillo et al., “Learning curve for Doppler measurement of fetal modified myocardial performance index,” *Ultrasound in Obstetrics & Gynecology*, vol. 37, no. 2, pp. 158–162, 2011.
- [62] R. Papanna, L. K. Mann, S. Molina, A. Johnson, and K. J. Moise, “Changes in the recipient fetal Tei index in the peri-operative period after laser photocoagulation of placental anastomoses for twin-twin transfusion syndrome,” *Prenatal Diagnosis*, vol. 31, no. 2, pp. 176–180, 2011.
- [63] J. Rychik, “Fetal cardiovascular physiology,” *Pediatric Cardiology*, vol. 25, no. 3, pp. 201–209, 2004.

Research Article

Free-Breathing 3D Imaging of Right Ventricular Structure and Function Using Respiratory and Cardiac Self-Gated Cine MRI

Yanchun Zhu,^{1,2,3} Jing Liu,³ Jonathan Weinsaft,⁴ Pascal Spincemaille,³ Thanh D. Nguyen,³ Martin R. Prince,³ Shanglian Bao,² Yaoqin Xie,¹ and Yi Wang³

¹*Institute of Biomedical and Health Engineering, Shenzhen Institutes of Advanced Technology, Chinese Academy of Sciences, 1068 Xueyuan Avenue, Shenzhen University Town, Nanshan District, Shenzhen 518055, China*

²*Beijing City Key Lab of Medical Physics and Engineering, School of Physics, Peking University, 201 Chengfu Road, Haidian District, Beijing 100871, China*

³*Department of Radiology, Weill Cornell Medical College, 515 East 71st Street, New York, NY 10021, USA*

⁴*Division of Cardiology, Department of Medicine, Weill Cornell Medical College, 520 East 70th Street, New York, NY 10065, USA*

Correspondence should be addressed to Yaoqin Xie; yq.xie@siat.ac.cn and Yi Wang; yiwang@med.cornell.edu

Received 15 August 2014; Revised 26 September 2014; Accepted 7 October 2014

Academic Editor: Volker Rasche

Copyright © 2015 Yanchun Zhu et al. This is an open access article distributed under the Creative Commons Attribution License, which permits unrestricted use, distribution, and reproduction in any medium, provided the original work is properly cited.

Providing a movie of the beating heart in a single prescribed plane, cine MRI has been widely used in clinical cardiac diagnosis, especially in the left ventricle (LV). Right ventricular (RV) morphology and function are also important for the diagnosis of cardiopulmonary diseases and serve as predictors for the long term outcome. The purpose of this study is to develop a self-gated free-breathing 3D imaging method for RV quantification and to evaluate its performance by comparing it with breath-hold 2D cine imaging in 7 healthy volunteers. Compared with 2D, the 3D RV functional measurements show a reduction of RV end-diastole volume (RVEDV) by 10%, increase of RV end-systole volume (RVESV) by 1.8%, reduction of RV systole volume (RVSV) by 21%, and reduction of RV ejection fraction (RVEF) by 12%. High correlations between the two techniques were found (RVEDV: 0.94; RVESV: 0.85; RVSV: 0.95; and RVEF: 0.89). Compared with 2D, the 3D image quality measurements show a small reduction in blood SNR, myocardium-blood CNR, myocardium contrast, and image sharpness. In conclusion, the proposed self-gated free-breathing 3D cardiac cine imaging technique provides comparable image quality and correlated functional measurements to those acquired with the multiple breath-hold 2D technique in RV.

1. Introduction

Cardiac magnetic resonance (CMR) is a widely used non-invasive imaging method for depicting cardiac structure, function, perfusion, and viability [1]. Cine MRI can capture the cyclic contraction and relaxation of the heart, enabling the evaluation of ventricular and valvular function as well as shunt detection [2]. Cardiac cine images are conventionally acquired using a breath-hold 2D balanced steady-state free precession (SSFP) pulse sequence, which can provide accurate and reproducible volume quantification [3] of both the left ventricle (LV) [4, 5] and the right ventricle (RV) [6–8]. However, the accuracy can be compromised by the slice misregistration due to inconsistent breath-holding levels during subsequent 2D scans and also by the slice

gap often used to shorten the number of required breath-holds in less cooperative patients. Breath-hold 3D SSFP cine MRI has been developed to overcome these challenges by providing contiguous spatial coverage without gap and eliminating slice misregistration. However, this approach requires a long breath-hold, which is not suitable for older patients, particularly those with cardiopulmonary diseases. A major limitation of breath-hold cine MRI in general is spatial resolution, which is constrained by the length of the breath-hold. Finally, compared to free breathing, breath holding alters the intrathoracic pressure which can impact right ventricular filling.

Recently, respiratory and cardiac self-gated cardiac cine MRI pulse sequences have emerged as promising imaging approaches for achieving higher resolution during free

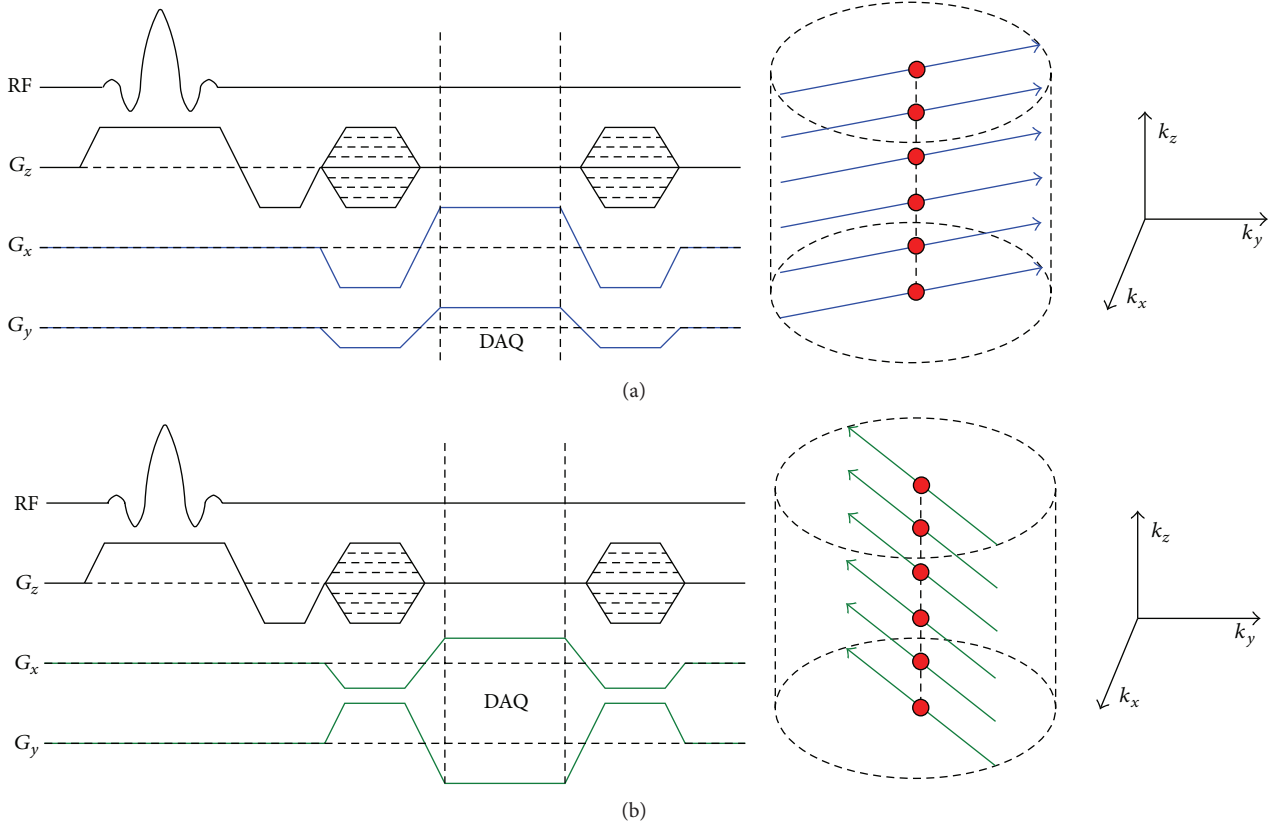


FIGURE 1: SSFP pulse sequence collects a profile with multiple slice encoding lines for a specific projection angle (blue lines in (a)) and changed projection angle after finishing the last profile (green lines in (b)).

breathing [9, 10]. While the utility of respiratory and cardiac self-gated cardiac cine MRI for LV imaging has been demonstrated, its application to the assessment of RV appears quite limited due to its thin wall structure. RV morphology and function have been increasingly recognized as important cardiac parameters in the diagnosis and treatment of patients with cardiopulmonary diseases [7] and especially congenital heart disease [11]. The purpose of this study was to develop a self-gated free-breathing 3D SSFP cine imaging method for RV quantification and to evaluate its performance by comparing with breath-hold 2D SSFP cine imaging in healthy volunteers.

2. Materials and Methods

2.1. Self-Gated Pulse Sequence Design. Figure 1 shows the pulse sequence diagram of the implemented self-gated 3D SSFP cine pulse sequence with hybrid radial k -space sampling (Cartesian sampling along slice encoding direction (k_z) and radial sampling in the k_x - k_y plane) [12, 13]. All slice encodes for a given projection angle are acquired sequentially (Figure 1(a)) and named as a profile. The acquisition then switches to the next projection angle (Figure 1(b)) and acquires the next profile. Each profile including n_z slice encodes spends the time of n_z TR. The projection angle is increased by the golden

angle of 111.2° to generate approximately uniform k -space distribution of the projections at any time point, allowing for robust sliding window reconstructions to achieve the desired temporal resolution and/or undersampling artifacts [14].

2.2. Image Reconstruction. The flow chart of self-gating image reconstruction is shown in Figure 2. The profile centers, shown as red points in Figure 1, were used to extract the self-gating signal of both respiratory and cardiac motions. As described in [12], 1D Fourier transform of profile centers can be used to derive imaging volume projection along the z -axis, which is called Z-intensity projection (ZIP). The center of mass (COM) of each ZIP contains mixed respiratory and cardiac motions that occur during the data acquisition. Since these motions are known to have different frequency contents (0.1–0.5 Hz for respiratory motion and 0.6–3 Hz for cardiac motion) [15], they can be separated by using band pass filter. The coil element with the smallest variance of the detected R-R intervals was selected for cardiac gating and, similarly, the coil element with the smallest variance of respiratory peak or valley positions was chosen for respiratory gating. This technique was capable of tracking both respiratory and cardiac motions [12].

The detected respiratory and cardiac motion signals were used to determine the respiratory position and cardiac phase associated with each profile. A respiratory histogram was

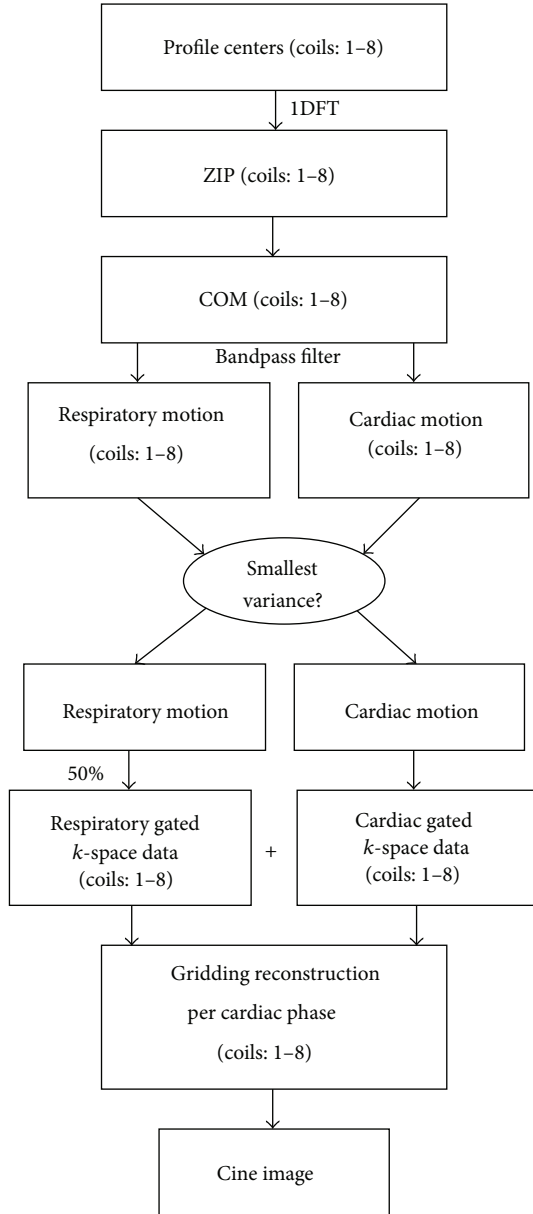


FIGURE 2: Block diagram of the algorithm used in self-gated reconstruction. Profile centers are used to derive self-gating signals. Respiratory and cardiac self-gating signals are used to classify profiles before using gridding reconstruction for each cardiac phase.

calculated and only data acquired within a given window (50% of acquired data) around the peak of the histogram were used for image reconstruction. The profiles detected with the same cardiac phase number, according to the self-gated cardiac motion signal, were used for reconstruction. Sliding window reconstruction with tornado temporal filter [16] (Figure 3(a)) was applied to decrease the streaking artifacts caused by undersampling in the k_x - k_y plane. The temporal aperture was the specified cardiac phase (p th) beginning at the lowest spatial frequency and increasing linearly to the highest spatial frequency (Figure 3(a)). The corresponding k -space distribution for the p th cardiac phase reconstruction

was depicted in Figure 3(b). The proportion of high spatial frequency k -space data shared from neighboring cardiac phases (one-third of the number of cardiac phases) was related to cardiac phase distance. Temporal resolution of each cardiac phase image was calculated as center period of tornado window, which spent n_z TR. Images were reconstructed from radial k -space data using gridding algorithm [17] with Kaiser-Bessel window as a gridding kernel.

2.3. *Human Imaging Experiment.* Cardiac cine MRI was performed in seven healthy volunteers (32 ± 7 yo, 5 male and 2 female) using a 1.5 T GE HDx scanner (maximum gradient amplitude 33 mT/m, slew-rate 120T/m/s, Excite 14M5 software; GE Healthcare, Waukesha, WI, USA). The study was approved by the local institutional review board at Weill Cornell Medical College, and written informed consent was obtained from all subjects. An eight-channel cardiac phased-array coil was used for signal reception. Both 2D and 3D cine MRI were performed in each subject in randomized order. The typical cine imaging parameters were as follows: (1) breath-hold multislice 2D cine: TR/TE = 3.5/1.2 ms, flip angle = 60° , BW = ± 125 kHz, FOV = 31 cm, imaging matrix = 256×192 (reconstructed to 256×256), slice thickness/gap = 7/3 mm, number of slices = 12–14, measured spatial resolution = $1.2 \times 1.6 \times 7$ mm³, reconstructed spatial resolution = $1.2 \times 1.2 \times 7$ mm³, views per segment = 24, temporal resolution = 84 ms, and number of reconstructed phases = 28 by view sharing for visualization purposes, scan time about 5 min (including nearly 2.5 min total rest time between consecutive breath-holds); (2) free-breathing self-gated 3D cine: TR/TE = 4.4/1.3 ms, flip angle = 40° , BW = ± 125 kHz, FOV = 31 cm, reconstructed image matrix = 256×256 , slice thickness = 7 mm (no gap), number of slices = 14, measured and reconstructed spatial resolutions = $1.2 \times 1.2 \times 7$ mm³, and temporal resolution = 61.6 ms, scan time about 5 min (to match 2D cine acquisition time). RV images were acquired in the short-axis view parallel to the mitral valve from the tricuspid valve to the pulmonic valve annulus.

2.4. *Data Analysis.* RV contours were traced by an experienced physician and RV volumes, from which RV ejection fraction (RVEF) was calculated, were measured by manual planimetry at end-diastole (RVEDV) and end-systole (RVESV) using a modified Simpson’s rule. Technical challenges associated with manual RV contouring are related to the thinness of the RV wall, wall trabeculations, infundibulum and pulmonary valve level, separation between RV and right atrium in basal slices, and protrusion of basal structures, such as the initial ascending aorta, all of which can lead to partial volume effect. If the pulmonary valve was evident in the basal slice, both in end-diastole and end-systole, only the portion of the volume below the level of the pulmonary valve was included. For the inflow part of the RV, the blood volume was excluded from the RV volume if the surrounding wall was thin and not trabeculated, as it was considered to be in the right atrium. To assess the agreement between 2D and 3D cine imaging, linear regression and Bland-Altman analysis were used [18]. A two-sided Wilcoxon signed-rank test was used to

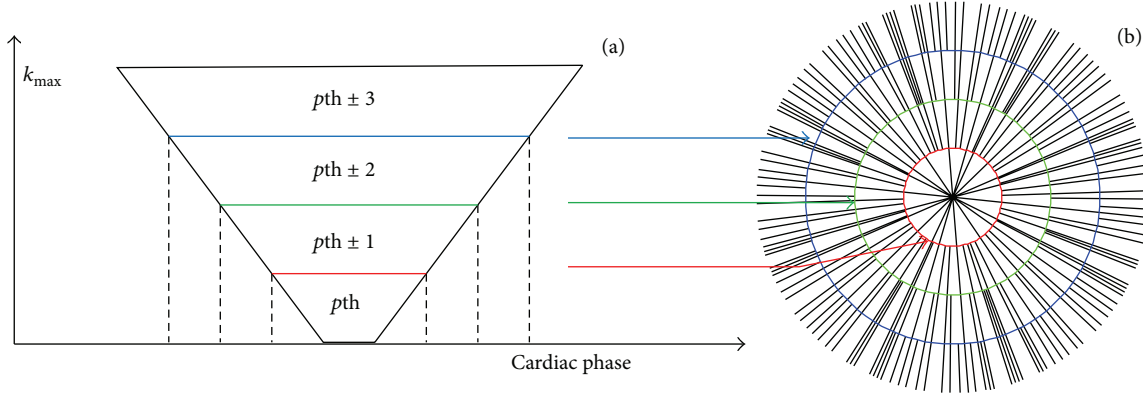


FIGURE 3: Schematic diagram of tornado temporal filter in sliding window reconstruction of p_{th} cardiac phase (a) and corresponding k -space distribution (b).

assess the difference between the two methods. The Pearson correlation coefficient was calculated to assess the correlation between the two methods. P value < 0.05 was considered statistically significant.

Image quality measures, including blood SNR, myocardium-blood contrast, CNR, and image sharpness, were calculated from a mid-ventricular slice for each volunteer. Blood SNR was calculated as the ratio of the average blood signal measured in the RV cavity to the standard deviation of background signals. Myocardium-blood contrast was calculated according to

$$\text{Contrast} = \frac{S_{\text{blood}} - S_{\text{myocardium}}}{|S_{\text{blood}}| + |S_{\text{myocardium}}|} \times 100\%, \quad (1)$$

where S_{blood} and $S_{\text{myocardium}}$ are the average signal intensities of the blood and myocardium, respectively. This relative measure gives a contrast range of 0-1 [19]. Compared with the contrast-to-noise ratio (CNR), the contrast parameter can directly reflect the contrast of two tissues by omitting the background noise difference. Image sharpness was used to evaluate the interface of the RV myocardium and the RV blood pool. Four signal profiles, evenly spaced around the RV circumference and positioned across the endocardial border of RV, were measured from end-diastole and end-systole mid-RV images. The local maximum (I_{max}) and minimum (I_{min}) intensity values across the endocardial border were determined, from which image sharpness was calculated as the inverse of the distance between $0.8(I_{\text{max}} - I_{\text{min}}) + I_{\text{min}}$ and $0.2(I_{\text{max}} - I_{\text{min}}) + I_{\text{min}}$ [20]. The image sharpness was obtained by averaging over the four profiles.

3. Results

All scans were completed successfully. Figure 4 shows an example of synchronized self-gating signals. Temporal resolutions of both self-gating signals were 61.6 ms. The valleys of cardiac self-gating curves were detected and used as trigger. The mean of heart rate and respiratory rate of the subject shown in Figure 4 is 55 bpm (beats per minutes) and 17 bpm (breaths per minute). Figure 5 shows the short-axis cardiac

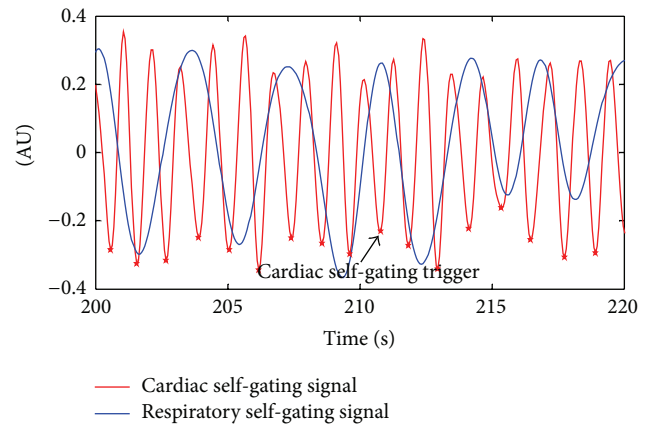


FIGURE 4: Cardiac self-gating signal (red line) and respiratory self-gating signal (blue line) were synchronized and presented, respectively. Amplitudes of both curves were rescaled for display purposes only. The asterisk represents cardiac self-gating trigger. Note: AU: arbitrary unit.

cine images obtained with breath-hold 2D and free-breathing 3D imaging during diastole and systole, demonstrating similar visualization of cardiac structures and excellent motion suppression of the developed self-gated 3D pulse sequence. Note that 3D imaging yielded 12 contiguous slices without gap, while 2D imaging only provided 10 slices with a 3 mm interslice gap. The 3D images have 61.6 ms temporal resolution and $1.2 \times 1.2 \text{ mm}^2$ in-plane spatial resolution, while the 2D images have 84 ms temporal resolution and $1.2 \times 1.6 \text{ mm}^2$ measured in-plane spatial resolution.

Figure 6 shows the comparison of RV areas in different slice locations between breath-hold 2D and self-gated free-breathing 3D methods. Average RV diastole and systole areas are shown as red curves for 2D and blue curves for 3D. RV systolic area curves of 2D and 3D fit well and the volumes are similar, with bias of $-1.1 \pm 6.4 \text{ mL}$ (as shown in Table 1). Compared with systole, diastolic areas measured in 2D cine images are larger, especially towards the cardiac apex and

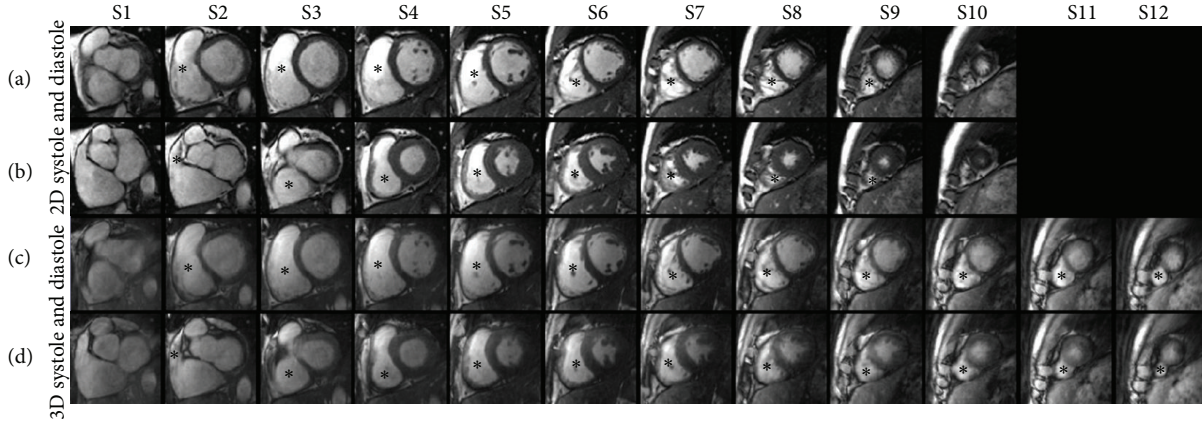


FIGURE 5: Comparisons of cine images acquired with the standard breath-hold 2D and the proposed free-breathing 3D techniques. Cardiac short-axis images of end-diastolic phase and end-systolic phase obtained with breath-hold 2D technique are shown in (a) and (b), and those obtained with the 3D technique are shown in (c) and (d), respectively. The asterisk denotes the RV.

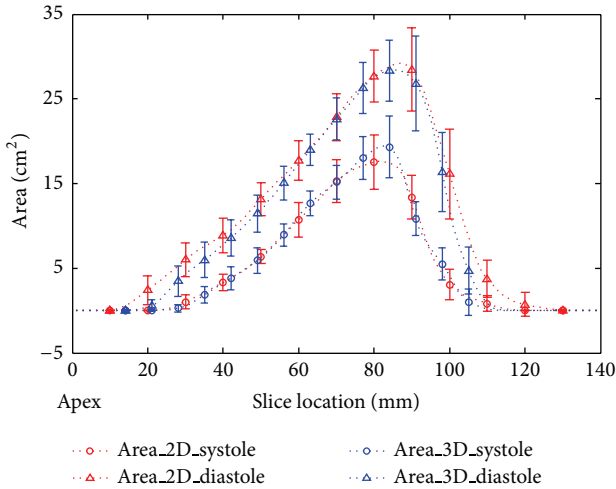


FIGURE 6: Comparison of systolic and diastolic RV areas obtained at different slice locations using breath-hold 2D and self-gated free-breathing 3D cine imaging.

base, which causes 2D RVEDV to be higher than 3D with bias of 15.1 ± 8.5 mL, as shown in Table 1.

Figure 7 shows the scatter plots and Bland-Altman plots comparing RV functional parameters obtained with breath-hold 2D and self-gated 3D cine imaging. There was a strong correlation between the two techniques with regard to RVEDV ($r = 0.94$), RVESV ($r = 0.85$), RVSV ($r = 0.95$), and RVEF ($r = 0.89$). The Pearson correlations were statistically significant ($P < 0.05$) (Table 1). The linear regression plots (Figures 7(a)–7(c)) show that 3D functional results are linear with 2D. The Bland-Altman plots (Figures 7(d)–7(f)) reveal that differences between 2D and 3D fall within ± 2 SD. Table 1 summarizes RV measurements over all subjects. Compared to 2D, there is a reduction of RVEDV by 10%, increase of RVESV by 1.8%, reduction of RVSV by 21%, and reduction of RVEF by 12% in 3D. The difference of the functional measurements between 2D and 3D techniques is statistically

TABLE 1: RV functional measurements obtained with the standard breath-hold 2D and self-gated free-breathing 3D cine MRI ($N = 7$).

	RVEDV (mL)	RVESV (mL)	RVSV (mL)	RVEF (%)
2D	147.5 ± 25.3	71.4 ± 11.4	76.1 ± 16.7	51.3 ± 4.7
3D	132.4 ± 22.1	72.5 ± 11.7	59.9 ± 13.4	45.0 ± 4.9
Bias	15.1 ± 8.5	-1.0 ± 6.4	16.2 ± 5.8	6.3 ± 2.2
Correlation	0.94	0.85	0.95	0.89
P value (Pearson)	0.001	0.02	0.001	0.007
P value (Wilcoxon)	0.02	0.74	0.02	0.02

Note: RVEDV: right ventricular end-diastolic volume, RVESV: right ventricular end-systolic volume, RVSV: right ventricular stroke volume, and RVEF: right ventricular ejection fraction.

significant in RVEDV, RVSV, and RVEF ($P < 0.05$) and not significant in RVESV ($P = 0.74$).

Figure 8 shows the comparison of mid-ventricular slices obtained during end-diastolic and end-systolic cardiac phases from seven volunteers. A few streaking artifacts appear in 3D self-gated images due to undersampling (undersampling ratio: 2~3) and motion. Table 2 shows image quality measurements from mid-ventricular images in Figure 8. Compared with 2D, the 3D image quality measurements show a small reduction in blood SNR, myocardium-blood CNR, myocardium contrast, and image sharpness. Compared with other image quality measurements, differences of myocardium-blood CNR and contrast measurements in end-diastole images were statistically significant ($P < 0.05$).

4. Discussion and Conclusions

In this study, a respiratory and cardiac self-gated free-breathing 3D cardiac cine imaging method was demonstrated to provide comparable image quality and correlated RV functional parameters to those obtained with the standard breath-hold 2D acquisition in 7 healthy volunteers. These

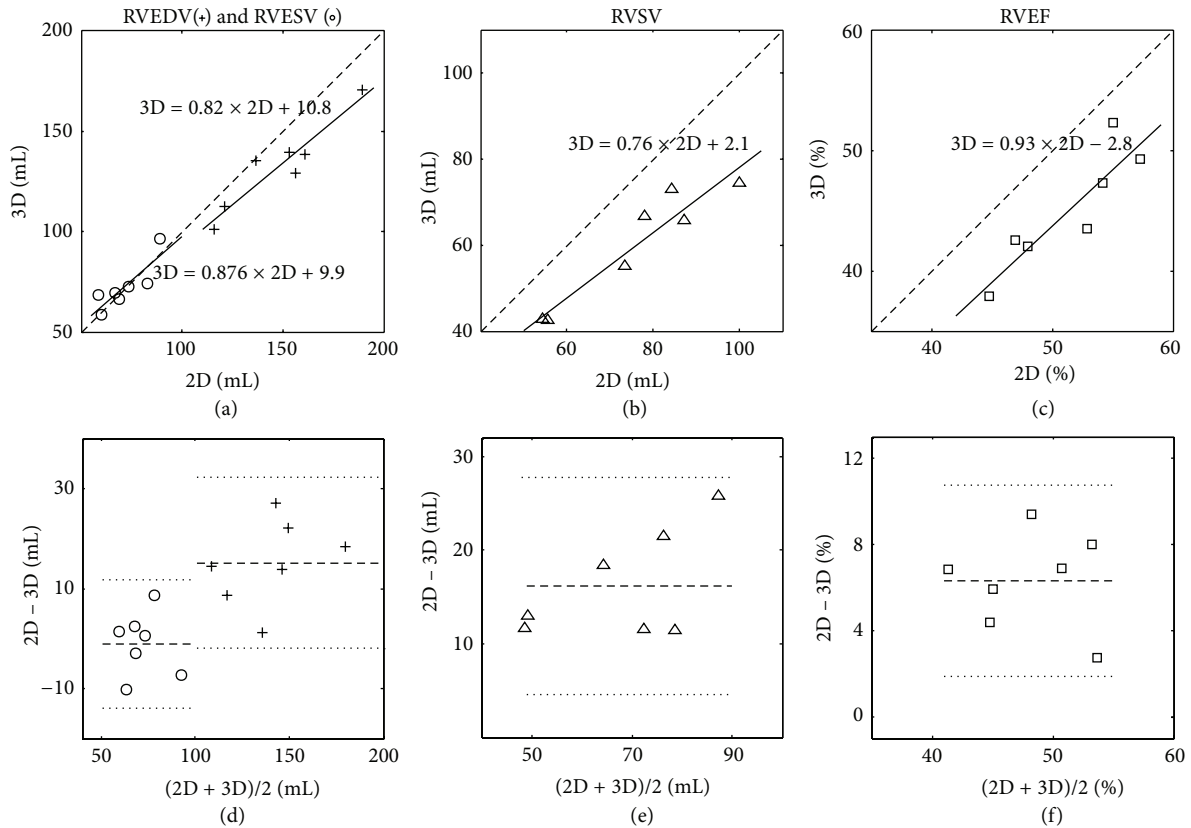


FIGURE 7: Linear regression and Bland-Altman analysis of RV quantification using 2D and 3D cine MRI. (a)–(c): RVEDV and RVESV, RVS, and RVEF measurements from seven volunteers with 3D self-gated free-breathing technique (y -axis) versus standard 2D breath-hold technique (x -axis), identical lines plotted as solid lines. (d)–(f): Bland-Altman plots of RVEDV and RVESV, RVS, and RVEF measurements. The central dashed lines show the mean bias and the upper and lower dotted lines show the variation limits (± 2 SD).

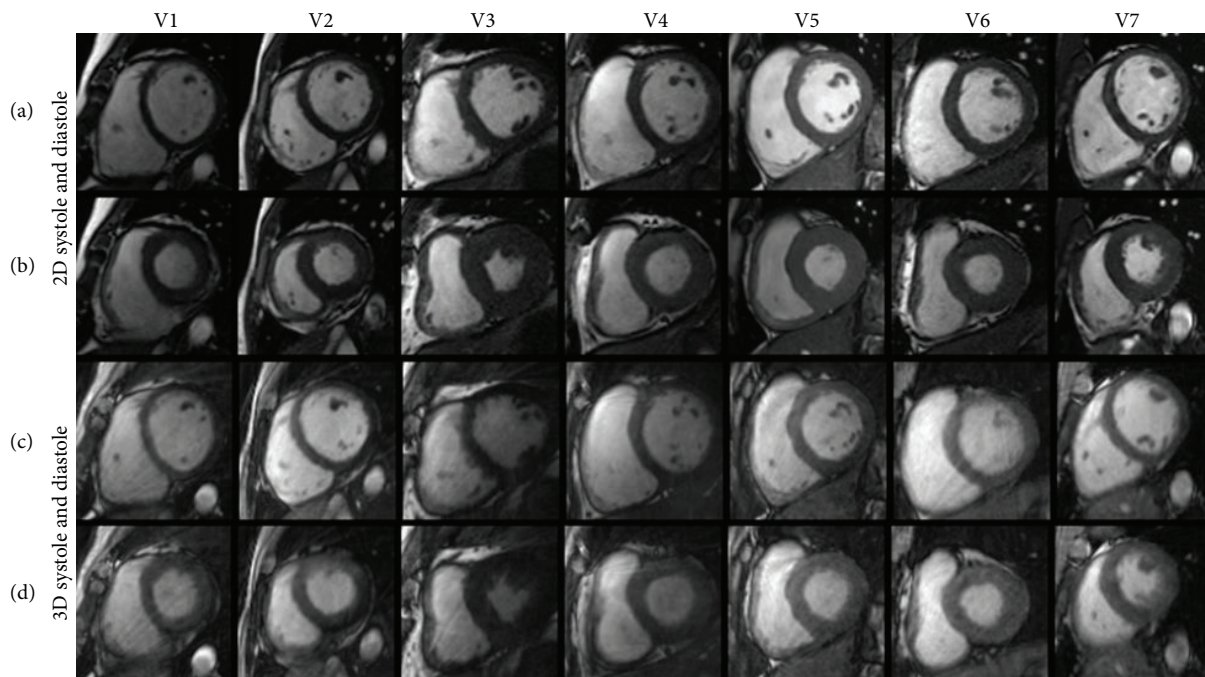


FIGURE 8: Images of mid-ventricular slices obtained with 2D and 3D cine imaging during end-diastole (a, c) and end-systole (b, d) in seven healthy volunteers.

TABLE 2: Image quality measurements of the standard breath-hold 2D and self-gated free-breathing 3D cine MRI ($N = 7$).

	SNR_{Blood}	$CNR_{\text{Blood-Myocardium}}$	$\text{Contrast}_{\text{Blood-Myocardium}}$	Image sharpness (mm^{-1})
2D diastole	105.1 ± 46.1	78.0 ± 29.2	61.9 ± 9.9	0.32 ± 0.03
3D diastole	90.0 ± 20.4	59.7 ± 12.9	49.8 ± 10.5	0.30 ± 0.08
<i>P</i> value	0.24	0.03	0.02	0.06
2D systole	104.7 ± 63.5	72.8 ± 44.3	55.4 ± 10.7	0.31 ± 0.04
3D systole	87.8 ± 9.3	60.0 ± 11.5	52.4 ± 12.5	0.23 ± 0.06
<i>P</i> value	1.00	0.61	0.61	0.50

data demonstrate that free-breathing 3D cine MRI can comprehensively assess RV structure and function. The proposed technique that derives respiratory and cardiac self-gating motion signals from original image data is feasible.

RVESV values between the two techniques were similar, with a difference of 1.8% between 3D and 2D, while RVEDV for 3D was 10% lower than it was for 2D. The volumes were calculated from the RV areas of each slice, which were demonstrated in Figure 5. Except for small differences around middle slices, which were mainly caused by bigger areas and slice gaps around the slices, the RV systole areas between 2D and 3D coincide well. On the contrary, the RV diastole area difference was found not only in middle slices but also in apex and basal slices. Besides, the difference of RVEDV was statistically significant ($P = 0.02$). Therefore, the difference between the two methods was not due to segmentation error. Because there are more slices obtained in the diastole phase, gaps between slices in 2D (3 mm) will increase the measurement error, especially around apical and basal slices. Differences between both methods may also be attributable to differences in temporal resolution or misregistration between 2D and 3D cine images of the apical and basal RV. Higher spatial resolution in slice direction could minimize the measurement error. Future study is necessary to improve spatial resolution in slice-direction of 3D cine MRI and test performance for RV assessment in routine clinical practice.

The 2D multiple breath-hold method is usually regarded as the gold standard for cardiac functional measurement. However, it suffers from slice misregistration and therefore has limited accuracy in cardiac chamber volume quantification. The 3D free-breathing self-gated method provides strongly correlated RV functional measurements compared to the 2D technique (Figure 6). However, significant differences were found between the RVEDV, RVSV, and RVEF results. Since it is difficult to choose between the two methods in accurate functional evaluation, other techniques are needed. 3D echocardiography has been shown to be accurate and reproducible for cardiac function measurements [21, 22]. Further study comparing these three techniques would be useful.

The radial trajectory based 3D k -space sampling method causes streaking artifacts when data is undersampled, which was found in the RV blood pool in Figures 7(c) and 7(d). In the fixed total scan time of 5 min, 5000 profiles were sampled. Each cardiac phase was assigned a smaller number of profiles (~150) when the respiratory self-gating window was chosen to be 50%. Tornado temporal filter (Figure 3)

could remove streaking artifacts using substantial cardiac phases at the cost of increasing cardiac motion blurring. Streaking artifacts may be removed using nonlinear inverse reconstruction [23]. 3D imaging generally provides higher SNR than 2D imaging in radial trajectory. However, thick slab saturation in 3D imaging reduces the inflow effect, so blood SNR and blood-to-myocardium CNR usually degrade when compared to 2D imaging [24]. Therefore, image quality measurements in Table 2 were smaller in the 3D method than in the 2D. In addition, lower SNR and CNR may also be caused by streaking artifacts presented as background noise. The myocardium-blood contrast directly reflects the contrast of two tissues omitting the background noise. However, the myocardium-blood contrast in 3D was still lower than in 2D and statistically significant in end-diastole images. The lower image sharpness in 3D is mainly due to respiratory motion and temporal filtering. Iterative image reconstruction was presented to decrease streaking artifacts and improve image quality [25] compared to regridding reconstruction. Future study is necessary to optimize the image reconstruction method and improve image temporal resolution.

Assessment of the RV in the short axis orientation also has important limitations: the position of the pulmonary and tricuspid valves cannot be clearly identified and therefore it is not usually possible to be certain of the basal boundary of the RV. This process requires manual segmentation of the RV endocardium which previous studies have shown to have a low reproducibility [26, 27]. Yet no further improvements have been reported in recent years and the reproducibility of RV manual RV segmentation remains lower than that of the LV [28]. A reproducibility study of 3D self-gated cine MRI is also needed.

In conclusion, free-breathing 3D cine SSFP imaging was achieved with simultaneous respiratory and cardiac self-gating at SA view for assessment of RV structure and function. Compared with 2D breath-hold method, the 3D RV functional measurements show a reduction of RVEDV by 10%, increase of RVESV by 1.8%, reduction of RVSV by 21%, and reduction of RVEF by 12%. High correlations between the two techniques were found (RVEDV: 0.94; RVESV: 0.85; RVSV: 0.95; and RVEF: 0.89). Compared with 2D, the 3D image quality measurements show a small reduction in blood SNR, myocardium-blood CNR, myocardium contrast, and image sharpness. The 3D SA cine imaging with the proposed technique provides image quality and functional measurements comparable to those acquired with the multiple breath-hold 2D Cartesian SSFP technique.

Ethical Approval

Approval for this study was granted by the local ethics committee.

Consent

All enrolled volunteers gave their informed consent prior to their inclusion in the study.

Conflict of Interests

All authors of the paper have no conflict of interests except Dr. Martin Prince who has a patent agreement with GE Healthcare.

Acknowledgments

This work is supported in part by grants from the National Basic Research Program 973 (Grant nos. 2011CB707701 and 2010CB732606), the National Key Technologies R&D Program (Grant no. 2012BAI23B07), the National Science Foundation of China (Grant no. 81171402), the NSFC Joint Research Fund for Overseas Research Chinese, Hong Kong and Macao Young Scholars (Grant no. 30928030), the Guangdong Innovative Research Team Program of China (Grant no. 2011S013), and the Strategic Partnership Program between Guangdong Province and Chinese Academy of Sciences Program (Grant no. 2011B090300079).

References

- [1] M. J. Campbell, "Cardiac MRI examination: an overview," in *Cardiac CT and MR for Adult Congenital Heart Disease*, pp. 23–53, Springer, Berlin, Germany, 2014.
- [2] W. Lee and E.-A. Park, "Pediatric cardiac imaging I: CT and MR techniques," in *Radiology Illustrated: Pediatric Radiology*, pp. 525–551, Springer, 2014.
- [3] L. E. Hudsmith, S. E. Petersen, J. M. Francis, M. D. Robson, and S. Neubauer, "Normal human left and right ventricular and left atrial dimensions using steady state free precession magnetic resonance imaging," *Journal of Cardiovascular Magnetic Resonance*, vol. 7, no. 5, pp. 775–782, 2005.
- [4] M. S. Florentine, C. L. Grosskreutz, W. Chang et al., "Measurement of left ventricular mass in vivo using gated nuclear magnetic resonance imaging," *Journal of the American College of Cardiology*, vol. 8, no. 1, pp. 107–112, 1986.
- [5] H. Sakuma, N. Fujita, T. K. F. Foo et al., "Evaluation of left ventricular volume and mass with breath-hold cine MR imaging," *Radiology*, vol. 188, no. 2, pp. 377–380, 1993.
- [6] E. S. Mackey, M. P. Sandler, R. M. Campbell et al., "Right ventricular myocardial mass quantification with magnetic resonance imaging," *The American Journal of Cardiology*, vol. 65, no. 7, pp. 529–532, 1990.
- [7] J. Mogelvang, M. Stubgaard, C. Thomsen, and O. Henriksen, "Evaluation of right ventricular volumes measured by magnetic resonance imaging," *European Heart Journal*, vol. 9, no. 5, pp. 529–533, 1988.
- [8] P. M. T. Pattynama, H. J. Lamb, E. A. van der Velde, R. J. van der Geest, E. E. van der Wall, and A. de Roos, "Reproducibility of MRI-derived measurements of right ventricular volumes and myocardial mass," *Magnetic Resonance Imaging*, vol. 13, no. 1, pp. 53–63, 1995.
- [9] A. C. Larson, R. D. White, G. Laub, E. R. McVeigh, D. Li, and O. P. Simonetti, "Self-gated cardiac cine MRI," *Magnetic Resonance in Medicine*, vol. 51, no. 1, pp. 93–102, 2004.
- [10] A. O. Leung, I. Paterson, and R. B. Thompson, "Free-breathing cine MRI," *Magnetic Resonance in Medicine*, vol. 60, no. 3, pp. 709–717, 2008.
- [11] C. H. Lorenz, E. S. Walker, T. P. Graham Jr., and T. A. Powers, "Right ventricular performance and mass by use of cine MRI late after atrial repair of transposition of the great arteries," *Circulation*, vol. 92, pp. Ii233–Ii239, 1995.
- [12] J. Liu, P. Spincemaille, N. C. F. Codella, T. D. Nguyen, M. R. Prince, and Y. Wang, "Respiratory and cardiac self-gated free-breathing cardiac CINE imaging with multiecho 3D hybrid radial SSFP acquisition," *Magnetic Resonance in Medicine*, vol. 63, no. 5, pp. 1230–1237, 2010.
- [13] J. Liu, O. Wieben, Y. Jung, A. A. Samsonov, S. B. Reeder, and W. F. Block, "Single breathhold cardiac CINE imaging with multiecho three-dimensional hybrid radial SSFP acquisition," *Journal of Magnetic Resonance Imaging*, vol. 32, no. 2, pp. 434–440, 2010.
- [14] S. Winkelmann, T. Schaeffter, T. Koehler, H. Eggers, and O. Doessel, "An optimal radial profile order based on the golden ratio for time-resolved MRI," *IEEE Transactions on Medical Imaging*, vol. 26, no. 1, pp. 68–76, 2007.
- [15] M. Buehrer, J. Curcic, P. Boesiger, and S. Kozerke, "Prospective self-gating for simultaneous compensation of cardiac and respiratory motion," *Magnetic Resonance in Medicine*, vol. 60, no. 3, pp. 683–690, 2008.
- [16] A. V. Barger, W. F. Block, Y. Toropov, T. M. Grist, and C. A. Mistretta, "Time-resolved contrast-enhanced imaging with isotropic resolution and broad coverage using an undersampled 3D projection trajectory," *Magnetic Resonance in Medicine*, vol. 48, no. 2, pp. 297–305, 2002.
- [17] J. I. Jackson, C. H. Meyer, D. G. Nishimura, and A. Macovski, "Selection of a convolution function for Fourier inversion using gridding," *IEEE Transactions on Medical Imaging*, vol. 10, no. 3, pp. 473–478, 1991.
- [18] J. M. Bland and D. G. Altman, "Statistical methods for assessing agreement between two methods of clinical measurement," *The Lancet*, vol. 1, no. 8476, pp. 307–310, 1986.
- [19] D. W. McRobbie, E. A. Moore, M. J. Graves, and M. R. Prince, *MRI from Picture to Proton*, Cambridge University Press, 2006.
- [20] A. C. Larson, P. Kellman, A. Arai et al., "Preliminary investigation of respiratory self-gating for free-breathing segmented cine MRI," *Magnetic Resonance in Medicine*, vol. 53, no. 1, pp. 159–168, 2005.
- [21] A. S. Gopal, Z. Shen, P. M. Sapin et al., "Assessment of cardiac function by three-dimensional echocardiography compared with conventional noninvasive methods," *Circulation*, vol. 92, no. 4, pp. 842–853, 1995.
- [22] J. Grewal, D. Majdalany, I. Syed, P. Pellikka, and C. A. Warnes, "Three-dimensional echocardiographic assessment of right ventricular volume and function in adult patients with congenital heart disease: comparison with magnetic resonance imaging," *Journal of the American Society of Echocardiography*, vol. 23, no. 2, pp. 127–133, 2010.
- [23] M. Uecker, S. Zhang, and J. Frahm, "Nonlinear inverse reconstruction for real-time MRI of the human heart using undersampled radial FLASH," *Magnetic Resonance in Medicine*, vol. 63, no. 6, pp. 1456–1462, 2010.

- [24] R. Nezafat, D. Herzka, C. Stehning, D. C. Peters, K. Nehrke, and W. J. Manning, "Inflow quantification in three-dimensional cardiovascular MR imaging," *Journal of Magnetic Resonance Imaging*, vol. 28, no. 5, pp. 1273–1279, 2008.
- [25] J. Liu, M. J. Redmond, E. K. Brodsky et al., "Generation and visualization of four-dimensional MR angiography data using an undersampled 3-D projection trajectory," *IEEE Transactions on Medical Imaging*, vol. 25, no. 2, pp. 148–157, 2006.
- [26] J. Sandstede, C. Lipke, M. Beer et al., "Age- and gender-specific differences in left and right ventricular cardiac function and mass determined by cine magnetic resonance imaging," *European Radiology*, vol. 10, no. 3, pp. 438–442, 2000.
- [27] S. E. Luijnenburg, D. Robbers-Visser, A. Moelker, H. W. Vliegen, B. J. M. Mulder, and W. A. Helbing, "Intra-observer and interobserver variability of biventricular function, volumes and mass in patients with congenital heart disease measured by CMR imaging," *The International Journal of Cardiovascular Imaging*, vol. 26, no. 1, pp. 57–64, 2010.
- [28] P. Beerbaum, P. Barth, S. Kropf et al., "Cardiac function by MRI in congenital heart disease: impact of consensus training on interinstitutional variance," *Journal of Magnetic Resonance Imaging*, vol. 30, no. 5, pp. 956–966, 2009.

Review Article

Use of Contrast-Enhanced Ultrasound in Carotid Atherosclerotic Disease: Limits and Perspectives

Gianfranco Varetto, Lorenzo Gibello, Claudio Castagno, Simone Quaglino, Matteo Ripepi, Emilio Benintende, Andrea Gattuso, Paolo Garneri, Stefano Zan, Giacomo Capaldi, Ugo Bertoldo, and Pietro Rispoli

Division of Vascular Surgery, Department of Surgical Sciences, University of Turin, Azienda Ospedaliera Universitaria Città della Salute e della Scienza, Molinette Corso Bramante 88, 10126 Torino, Italy

Correspondence should be addressed to Pietro Rispoli; pietro.rispoli@unito.it

Received 14 August 2014; Revised 6 November 2014; Accepted 11 November 2014

Academic Editor: Marco Francone

Copyright © 2015 Gianfranco Varetto et al. This is an open access article distributed under the Creative Commons Attribution License, which permits unrestricted use, distribution, and reproduction in any medium, provided the original work is properly cited.

Contrast-enhanced ultrasound (CEUS) has recently become one of the most versatile and powerful diagnostic tools in vascular surgery. One of the most interesting fields of application of this technique is the study of the carotid atherosclerotic plaque vascularization and its correlation with neurological symptoms (transient ischemic attack, minor stroke, and major stroke) and with the characteristics of the “vulnerable plaque” (surface ulceration, hypochoic plaques, intraplaque hemorrhage, thinner fibrous cap, and carotid plaque neovascularization at histopathological analysis of the sample after surgical removal). The purpose of this review is to collect all the original studies available in literature (24 studies with 1356 patients enrolled) and to discuss the state of the art, limits, and future perspectives of CEUS analysis. The results of this work confirm the reliability of this imaging study for the detection of plaques with high risk of embolization; however, a shared, user-friendly protocol of imaging analysis is not available yet. The definition of this operative protocol becomes mandatory in order to compare results from different centers and to validate a cerebrovascular risk stratification of the carotid atherosclerotic lesions evaluated with CEUS.

1. Introduction

CEUS represents one of the major breakthroughs in the field of diagnostic ultrasound. In fact, the contrast medium, injected intravenously, passes through the vascular region of interest generating an enhanced ultrasound signal that allows a better morphological and functional imaging resolution [1]. Moreover the simplicity and rapidity of execution even at the patient's bedside encouraged its application for different vascular purposes: the definition of the degree of stenosis and plaque surface (i.e., higher sensitivity for plaque ulceration or near-occlusion stenosis), the diagnosis of intrastent restenosis, the detection of type II endoleaks (even those with low flow rate), the assessment of organ perfusion (i.e., kidney transplantation), or the assessment of tumor perfusion (important prognostic parameter in metastatic tumors) [2]. Another interesting field of application of CEUS is the study of the carotid atherosclerotic plaque vascularization and its

correlation with cerebrovascular neurological events (stroke, transient ischemic attack). Data available from large study population in literature reveal a 5-year risk for ipsilateral stroke of 5% of patients with asymptomatic carotid artery stenosis of 70% or greater [3–5]. The traditional parameters for the description of a carotid atherosclerotic plaque (degree of stenosis, systolic peak velocity) are insufficient predictors of the risk of embolization while the vascularization of the atherosclerotic plaque, evaluated with CEUS, is correlated with a more accurate “qualitative” analysis of the carotid disease [2]. Differently from what happens for the other fields of application of CEUS, the study of the carotid plaque vascularization requires a more precise quantification of the enhancement which is obtained by a visual or semiautomated method [6]. The objective of this review is to analyze the application of CEUS for the study of plaque microvascularization in carotid atherosclerosis and to define the strengths and limits of this technique.

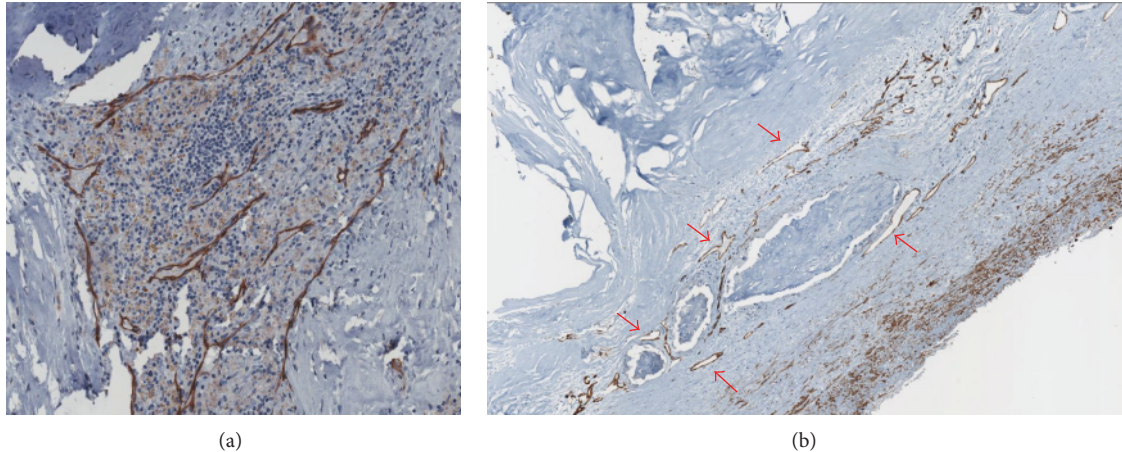


FIGURE 1: (a) Histopathological preparation of a carotid atherosclerotic plaque colored with CD31 endothelial-specific stain (brown) showing the close correlation between plaque vascularization and the inflammatory response. (b) Histopathological preparation of a carotid atherosclerotic plaque colored with CD31 endothelial-specific stain (brown) showing larger microvessels (red arrows) and areas of plaque hemorrhage.

2. Correlation between Plaque Microvascularization and Potentially Symptomatic Atherosclerotic Lesions

The inflammatory etiopathogenesis of atherosclerosis has been widely demonstrated in several animal models and later confirmed in human models [7]. In particular at the level of flow turbulence along the vascular tree (vessel bifurcation), the subintimal deposition of cholesterol and oxidized lipoproteins generates an inflammatory response with the recruitment of white blood cells, primarily macrophages, and the production of cytokines and enzymes. Among different cellular responses to the inflammatory stimulus there is the liberation from the smooth muscles cells of vascular endothelial growth factor (VEGF) with the consequent activation of neoangiogenesis of the vessel wall (Figure 1). The newly formed vessels inside the atherosclerotic plaque however are immature and leaky due to reduced gap junctions, thus serving as a port of entry for other inflammatory cells, lipids, and even red blood cells, which contribute to plaque growth. In the same contest macrophages produce metalloproteinases, like MMP-9 and other collagenases that destroy the connective fibrous tissue, thus stimulating the neovessels growth [8]. All these plaque changes lead to a vulnerable atherosclerotic plaque [7]. It is common experience in clinical practice that irregular, ulcerated plaque surfaces, lipid necrotic core, thin fibrous cap, anechoic-hypoechoic appearance, and intraplaque neovessels characterize potentially unstable atherosclerotic lesions with high risk of embolization and thrombosis. However, it is common experience that not all the atherosclerotic lesions behave in the same way. In fact some of them react to the inflammation stimulus with the precipitation of calcium salts (calcific plaques) and others with the simple transformation of muscular cells into connective cells (fibrous plaques). The exact mechanism of differentiation of the plaque is still partially unknown but some factors, such as genetic predisposition, uncontrolled

risk factors like smoke, diabetes mellitus, hypertension, and dyslipidemia, may influence the process.

3. Methods

3.1. Search Strategy. This review included all available original studies reporting the use of CEUS for the evaluation of the vascularization of the carotid atherosclerotic plaque and its correlation with ipsilateral neurological events and with other indicators of plaque “vulnerability”. Data were collected from the online MEDLINE database in July 2014 using PubMed (National Center for Biotechnology Information, US National Library of Medicine, Bethesda, MD). The search strategy included the words “carotid,” “atherosclerosis,” and “contrast-enhanced.” No time restriction for publication date was used. The search was restricted to articles published in English and to studies in humans.

3.2. Study Selection, Data Extraction, and Analysis. All abstracts were reviewed online and articles meeting the inclusion criteria were identified and downloaded for data extraction. In addition, a manual search of the reference lists of the identified studies was performed, and references were evaluated. Data collected from the selected studies were registered into a specific database and analyzed with Microsoft Excel 2010 (Microsoft Corporation, Redmond, WA). Despite the heterogeneity of the studies it was possible to create different macrocategories of correlation between the degree of the enhancement of the atherosclerotic lesion and neurological symptoms (transient ischemic attack, minor stroke, and major stroke) or other plaque characteristics: histology (quantification of the microvascularization of the carotid plaque after surgical removal), echogenicity with Doppler ultrasound (evaluated with a visual assessment according to the Gray Weale scale—GW scale—or with a software analysis according to the Gray Scale Median—GSM), signs

of microembolization, or plaque instability (plaque surface ulceration, cerebral ipsilateral microembolization detected with transcranial Doppler ultrasonography in absence of other possible causes).

4. Results

The search identified 24 original studies (100% single-center studies) suitable for revision from 2007 to 2014 (Table 1) [9–32]. The review population consisted of 1356 patients with carotid atherosclerosis examined with CEUS; 946 patients (70%) were asymptomatic. In 19 studies (76%) the contrast medium used was SonoVue (Bracco, Altana Pharma, Konstanz, Germany), 2 studies (7%) used Definity (Bristol-Myers Squibb Medical Imaging, Billerica, Massachusetts), and 3 studies (7%) used Optison (GE Healthcare, Little Chalfont, Buckinghamshire, UK). CEUS imaging of the carotid artery was performed using linear array vascular probe with transmission frequencies ranging from 3 to 15 MHz and mechanical index ranging from 0.06 to 1.4. The analysis of the contrast enhancement was performed with a semiautomated software in 16 studies (often home-made software). In 15 studies, a visual classification of the plaque enhancement was performed by two different operators (nonuniformity in scoring methods). In 7 studies (29%) plaques were evaluated with both methods. The correlation between data obtained with CEUS and histopathologic results was performed in 12 studies (50%, 433 patients) and all the studies found a statistical significant correlation: plaques with higher enhancement have a highly significant vascularization of the plaque. Ten studies (41%, 578 patients) evaluated the correlation between CEUS images and the presence of ipsilateral neurological symptoms: in three cases (30%, 91 patients) results did not reach statistical significance to demonstrate that plaques with greater contrast enhancement are more frequently related to clinical symptoms. In 7 studies (29%, 331 patients) CEUS analysis was compared to the plaque echogenicity; all the studies found a statistically significant correlation: plaques with high contrast enhancement have a low echogenicity. Six studies (25%, 351 patients) compared CEUS with other indicators of “vulnerable plaque” (surface ulceration, cerebral microembolization detected with transcranial Doppler); all the studies found a statistically significant correlation: the increased vascularization of carotid atherosclerotic plaques evaluated with CEUS is more frequently related to cerebral microembolization or surface ulceration. One study (4%, 143 patients) compared CEUS to the patient’s gender with a statistically significant correlation ($P = 0.03$): women have a higher contrast enhancement of the carotid plaque.

5. Discussion

5.1. Correlation between CEUS and the Characteristics of the Vulnerable Carotid Plaque. Data collected from an overall review population of 1356 patients demonstrate that information obtained by CEUS imaging is strictly dependent not only on the plaque microvascularization (histological analysis) but also correlated to the plaque echogenicity, the surface

ulceration, and the intraplaque hemorrhage (100% agreement among the studies). All these parameters together define an atherosclerotic plaque with high risk of embolization. In detail plaques with low echogenicity, surface ulceration, and histopathological findings of intraplaque hemorrhage have a greater enhancement with CEUS compared to calcific or fibrous plaques. Results on the correlation between CEUS and clinical neurological symptoms do not reach statistical evidence in all the studies; in fact 7 studies (487 patients) established a significant relationship between the two parameters while 3 studies (91 patients) did not reach statistical significance. The reason of this finding is not completely clear: according to the general agreement among the studies on the reliability of CEUS for the detection of a “vulnerable plaque,” it would be logical to expect also a correlation with neurological symptoms. However these results could be partially explained with the low single-center study population or with silent neurological damage among asymptomatic patients. From the results obtained, CEUS appears to be one of the most reliable imaging studies for the detection of atherosclerotic lesions with high risk of embolization because of the correlation with every single expression of the plaque instability (intraplaque hemorrhage, surface ulceration, low echogenicity, and plaque microvascularization). In current literature there is not a specific indication for the “suitable patient” for CEUS analysis; however, the strong relationship between the plaque enhancement and the echogenicity of the carotid plaque led some authors to select a subgroup of the population (asymptomatic with an hypoechoic carotid plaque) that would benefit most from this investigation [19].

5.2. CEUS Imaging Analysis. The acquisition of CEUS images was made with different ultrasound hardware and different presettings (i.e., mechanical index, linear probes). The majority of the studies used a linear probe with frequencies between 3 MHz and 10 MHz. The mechanical index as well differs among the studies; however, many authors agree that a lower mechanical index (between 0.06 and 0.2) is preferred to obtain a better image resolution and to reduce the risk of rupture of the microbubbles of contrast agent [33].

The analysis of the images obtained with CEUS can be performed in two ways: the semiautomated method and the visual score of the enhancement; often they are used together. The semiautomated assessment is performed with a software (usually a home-made software) that analyzes the variation of enhancement intensity over time in a region of interest (ROI). The timing of the analysis differs among the studies (i.e., evaluation of maximum signal intensity [19], evaluation of the late phase of contrast enhancement [23]) as well as the unit of measurements (i.e., dB-enhanced [20], percentage ratio between area of plaque captation and silent areas [19]). Strengths of this method are a better reproducibility over time with the same software and presetting and the reduction of the operator-related bias. Some limits of this method are the need of reprocessing the images (not immediate result) and the need of a motion tracking algorithm (not simple implementation) to reduce errors of interpretation on the luminal side of the plaque. On the other hand, the visual

TABLE I: Summary of studies on carotid contrast-enhanced ultrasound (CEUS) for the detection of intraplaque neovascularization. The results of each study are expressed with the statistical significance (P value) of the correlation between the parameters.

Author	Year	Number of patients	Symptomatic	Asymptomatic	Histology	Contrast agent	Ultrasound apparatus	Vascular probe	Mechanical index	CEUS analysis					Results			
										Semiatomated analysis	Visual assessment	CEUS and carotid symptoms	CEUS and echogenicity	CEUS and other vulnerable characteristics	CEUS and gender	Software and visual assessment		
Li et al. [9]	2014	17	13	4	1	SonoVue	Philips iU-22 ultrasound system	L 9-3	0,07	1	1	0,002	0	0	0	0	0	0
Hjelmgren et al. [10]	2014	13	7	6	0	SonoVue	Siemens S2000 system	L 9-4	0,06	1	1	0	0,05	0,01	0	0	0	0,001
Kim et al. [11]	2014	89	0	89	1	SonoVue	Sequoia 512 Siemens system	L 15-8	0,19	0	1	0,021	0	0	0	0	0	0
van den Oord et al. [12]	2014	143	0	143	0	SonoVue	Philips iU-22 ultrasound system	L 9-3	0,06-0,08	1	1	0	0	0	0	0	0	0,03
Müller et al. [13]	2014	33	17	16	1	SonoVue	Antares Siemens system	nn	nn	1	1	0,01	Not significant	0	0	0	0	0,02
Vavuranakis et al. [14]	2013	14	0	14	1	SonoVue	Acuson Sequoia 512 Siemens system	L 15-8	nn	1	0	0,002	0	0	0	0	0	0
Ritter et al. [15]	2013	41	41	0	0	SonoVue	GE Logiq 7 system	L 9-3	nn	0	1	0	0	0	0	0,02	0	0
Hjelmgren et al. [16]	2013	52	10	42	0	SonoVue	Siemens S2000 system	L 9-4	0,06	1	0	0	Not significant	0,02	0	0	0	0
van den Oord et al. [17]	2013	69	0	69	0	SonoVue	Philips iU-22 ultrasound system	L 9-3	0,06-0,08	1	1	0	0	0	0	0,05	0	0
Zhou et al. [18]	2013	46	24	22	0	SonoVue	Acuson Sequoia 512 Siemens system	L 2	0,07	0	1	0	Not significant	0	0,05	0	0	0
Varetto et al. [19]	2012	51	12	39	1	SonoVue	Esaote MyLab 25 Gold system	L 9-2	nn	1	0	0,001	0,01	0,02	0	0	0	0
Faggioli et al. [20]	2011	22	7	15	1	SonoVue	Philips iU-22 ultrasound system	L 9-3	0,13	1	0	0,003	0,006	0	0	0	0	0
Hoogi et al. [21]	2011	27	8	19	1	Definity	Philips iU-22 ultrasound system	L 8-4	nn	1	0	0,01	0	0	0	0	0	0
Shalhoub et al. [22]	2011	31	16	15	1	SonoVue	Philips iU-22 ultrasound system	L 12-5	0,34	1	0	0,004	0	0	0	0	0	0
Owen et al. [23]	2010	37	16	21	0	SonoVue	Philips iU-22 ultrasound system	L 12-5	0,34	1	0	0	0,005	0	0	0	0	0

TABLE 1: Continued.

Author	Year	Number of patients	Symptomatic	Asymptomatic	Histology	Contrast agent	Ultrasound apparatus	Vascular probe	Mechanical index	CEUS analysis				Results			
										Semiatomated analysis	Visual assessment	CEUS and histology	CEUS and carotid symptoms	CEUS and echogenicity	CEUS and other vulnerable characteristics	CEUS and gender	Software and visual assessment
Huang et al. [24]	2010	183	86	97	0	SonoVue	Acuson Sequoia 512 Siemens system	L 15-8	0,35	1	1	0	0,001	0	0	0	0,001
Staub et al. [25]	2010	147	17	130	0	Definity	ATL HDI 5000 Philips system	L 7-4	0,06-0,1	0	1	0	0	0	0,034	0	0
Giannoni et al. [26]	2009	77	64	9	1	SonoVue	Acuson Sequoia 512 Siemens system	L 9-3	0,4-1,4	1	1	>0,05	0,001	0,001	0	0	0
Magnoni et al. [27]	2009	25	0	25	0	Optison	GE Vivid 7 system	L 7	0,08-0,1	0	1	0	0	0	0,001	0	0
Xiong et al. [28]	2009	104	35	69	0	SonoVue	GE Logiq 9 system	L 9-3	0,13	1	0	0	0,001	0	0	0	0
Huang et al. [29]	2008	63	0	63	0	SonoVue	Acuson Sequoia 512 Siemens system	L 15-8	0,35	1	0	0	0	0,01	0	0	0
Coli et al. [30]	2008	32	28	4	1	Optison	GE Vivid 7 system	L 7	0,08-0,1	0	1	0,005	0,001	0	0	0	0
Vicenzini et al. [31]	2007	23	0	23	1	SonoVue	Acuson Sequoia 512 Siemens system	L 6-15	0,4-1,4	0	1	>0,05	0	>0,05	>0,05	0	0
Shah et al. [32]	2007	17	5	12	1	Optison	ATL HDI 5000 Philips system	L 7-4	0,06-0,1	0	1	0,002	0	0	0	0	0
Total		1356	406	946	12					16	15						

score allows a direct interpretation of the CEUS examination (easier applicability in a clinical setting) but with an increased risk of operator-related bias and less accurate confrontation of the results obtained. Moreover a univocal visual scale is still not defined. Currently no data are available on the superiority of the semiautomated analysis compared to the visual assessment for CEUS. From the data collected in literature it becomes mandatory to create a generally shared operative protocol for the interpretation of CEUS results in order to compare experiences from different centers.

5.3. Tolerability of CEUS. The contrast medium injected intravenously consists of microbubbles filled with gasses (air or high molecular weight gasses) and it has been shown to have a good safety profile. In literature the three most common side effects observed in clinical trials were headache (2,3%), injection site pain (1,4%), and injection site bruising, burning, or paresthesia (1,7%) [34]. Among the studies evaluated in this review, 19 used SonoVue (Bracco), 3 used Optison (GE Healthcare), and 2 studies performed CEUS with Definity (Bristol-Myers). None of the studies reported severe side effects, procedural complication, or anaphylactic reactions to the contrast medium.

5.4. Limits and Future Perspectives of CEUS for the Study of Carotid Atherosclerosis. Despite the excellent results described above, some limits are still evident. Firstly CEUS remains an operator dependent imaging technique; for this reason the creation of a common semiautomated software for the image elaboration could increase the reproducibility and the homogeneity among different operators. Moreover the sensibility of CEUS decreases in heavy calcified plaques with important acoustic shadow. Lastly the bidimensional analysis of the plaque enhancement assumes that the longitudinal cross section of the plaque analyzed is representative of the whole carotid plaque. For this reason it could be interesting to apply the emerging technique of 3D and 4D Doppler ultrasonography to CEUS for a global evaluation of the carotid atherosclerotic lesion.

6. Conclusion

This review confirms the great potential of CEUS for the detection of carotid atherosclerotic plaques with high risk of embolization. However the different procedures used for the analysis of the contrast enhancement limit the possibility to compare results from different centers. The creation of a common, well-established, user-friendly, and operative protocol is essential to overcome this limit to create multicentric studies in order to define a cerebrovascular risk stratification with accurate enhancement cut-offs.

Conflict of Interests

The authors declare that there is no conflict of interests regarding the publication of this paper.

References

- [1] R. Badea and L. Ciobanu, "Contrast enhanced and doppler ultrasonography in the characterization of the microcirculation. Expectancies and performances," *Medical Ultrasonography*, vol. 14, no. 4, pp. 307–313, 2012.
- [2] D. Staub, S. Partovi, S. Imfeld et al., "Novel applications of contrast-enhanced ultrasound imaging in vascular medicine," *Vasa*, vol. 42, no. 1, pp. 17–31, 2013.
- [3] D. Jonas, C. Feltner, and H. Amick, "Screening for asymptomatic carotid artery stenosis: a systematic review and meta-analysis for the U.S. preventive services task force," *Annals of Internal Medicine*, vol. 161, no. 5, pp. 336–346, 2014.
- [4] A. Nicolaides, S. Kakkos, E. Kyriacou et al., "Asymptomatic internal carotid artery stenosis and cerebrovascular risk stratification," *Journal of Vascular Surgery*, vol. 52, no. 6, pp. 1486–1496, 2010.
- [5] S. K. Kakkos, M. B. Griffin, A. N. Nicolaides et al., "The size of juxtaluminous hypoechoic area in ultrasound images of asymptomatic carotid plaques predicts the occurrence of stroke," *Journal of Vascular Surgery*, vol. 57, no. 3, pp. 609.e1–618.e1, 2013.
- [6] G. L. ten Kate, S. C. H. van den Oord, E. J. G. Sijbrands et al., "Current status and future developments of contrast-enhanced ultrasound of carotid atherosclerosis," *Journal of Vascular Surgery*, vol. 57, no. 2, pp. 539–546, 2013.
- [7] A. C. Langheinrich, M. Kampschulte, T. Buch, and R. M. Bohle, "Vasa vasorum and atherosclerosis—quid novi?" *Thrombosis and Haemostasis*, vol. 97, no. 6, pp. 873–879, 2007.
- [8] H. Nagase, R. Visse, and G. Murphy, "Structure and function of matrix metalloproteinases and TIMPs," *Cardiovascular Research*, vol. 69, no. 3, pp. 562–573, 2006.
- [9] C. Li, W. He, D. Guo et al., "Quantification of carotid plaque neovascularization using contrast-enhanced ultrasound with histopathologic validation," *Ultrasound in Medicine and Biology*, vol. 40, pp. 1827–1833, 2014.
- [10] O. Hjelmgren, L. Johansson, U. Prael, C. Schmidt, J. Fredén-Lindqvist, and G. M. L. Bergström, "A study of plaque vascularization and inflammation using quantitative contrast-enhanced US and PET/CT," *European Journal of Radiology*, vol. 83, no. 7, pp. 1184–1189, 2014.
- [11] H. S. Kim, J. S. Woo, B. Y. Kim et al., "Biochemical and clinical correlation of intraplaque neovascularization using contrast-enhanced ultrasound of the carotid artery," *Atherosclerosis*, vol. 233, no. 2, pp. 579–583, 2014.
- [12] S. C. H. van den Oord, J. van der Burg, Z. Akkus et al., "Impact of gender on the density of intraplaque neovascularization: a quantitative contrast-enhanced ultrasound study," *Atherosclerosis*, vol. 233, no. 2, pp. 461–466, 2014.
- [13] H. Müller, A. Viacoz, I. Kuzmanovic et al., "Contrast-enhanced ultrasound imaging of carotid plaque neo-vascularization: accuracy of visual analysis," *Ultrasound in Medicine & Biology*, vol. 40, no. 1, pp. 18–24, 2014.
- [14] M. Vavuranakis, F. Sigala, D. A. Vrachatis et al., "Quantitative analysis of carotid plaque vasa vasorum by CEUS and correlation with histology after endarterectomy," *Vasa*, vol. 42, no. 3, pp. 184–195, 2013.
- [15] M. A. Ritter, K. Theismann, M. Schmiedel, E. B. Ringelstein, and R. Dittrich, "Vascularization of carotid plaque in recently symptomatic patients is associated with the occurrence of transcranial microembolic signals," *European Journal of Neurology*, vol. 20, no. 8, pp. 1218–1221, 2013.

- [16] O. Hjelmgren, P. Holdfeldt, L. Johansson et al., "Identification of vascularised carotid plaques using a standardised and reproducible technique to measure ultrasound contrast uptake," *European Journal of Vascular and Endovascular Surgery*, vol. 46, no. 1, pp. 21–28, 2013.
- [17] S. C. H. van den Oord, Z. Akkus, J. E. Roeters van Lennep et al., "Assessment of subclinical atherosclerosis and intraplaque neovascularization using quantitative contrast-enhanced ultrasound in patients with familial hypercholesterolemia," *Atherosclerosis*, vol. 231, no. 1, pp. 107–113, 2013.
- [18] Y. Zhou, Y. Xing, Y. Li et al., "An assessment of the vulnerability of carotid plaques: a comparative study between intraplaque neovascularization and plaque echogenicity," *BMC Medical Imaging*, vol. 13, article 13, 2013.
- [19] G. Varetto, L. Gibello, L. Bergamasco et al., "Contrast enhanced ultrasound in atherosclerotic carotid artery disease," *International Angiology*, vol. 31, no. 6, pp. 565–571, 2012.
- [20] G. L. Faggioli, R. Pini, R. Mauro et al., "Identification of carotid "Vulnerable Plaque" by contrast-enhanced ultrasonography: correlation with plaque histology, symptoms and cerebral computed tomography," *European Journal of Vascular and Endovascular Surgery*, vol. 41, no. 2, pp. 238–248, 2011.
- [21] A. Hoogi, D. Adam, A. Hoffman, H. Kerner, S. Reisner, and D. Gaitini, "Carotid plaque vulnerability: quantification of neovascularization on contrast-enhanced ultrasound with histopathologic correlation," *American Journal of Roentgenology*, vol. 196, no. 2, pp. 431–436, 2011.
- [22] J. Shalhoub, C. Monaco, D. R. J. Owen et al., "Late-phase contrast-enhanced ultrasound reflects biological features of instability in human carotid atherosclerosis," *Stroke*, vol. 42, no. 12, pp. 3634–3636, 2011.
- [23] D. R. Owen, J. Shalhoub, S. Miller et al., "Inflammation within carotid atherosclerotic plaque: assessment with late-phase contrast-enhanced US," *Radiology*, vol. 255, no. 2, pp. 638–644, 2010.
- [24] P. Huang, C. Chen, W. Aronow et al., "Assessment of neovascularization within carotid plaques in patients with ischemic stroke," *World Journal of Cardiology*, vol. 26, pp. 89–97, 2010.
- [25] D. Staub, M. B. Patel, A. Tibrewala et al., "Vasa vasorum and plaque neovascularization on contrast-enhanced carotid ultrasound imaging correlates with cardiovascular disease and past cardiovascular events," *Stroke*, vol. 41, no. 1, pp. 41–47, 2010.
- [26] M. F. Giannoni, E. Vicenzini, M. Citone et al., "Contrast carotid ultrasound for the detection of unstable plaques with neoangiogenesis: a pilot study," *European Journal of Vascular and Endovascular Surgery*, vol. 37, no. 6, pp. 722–727, 2009.
- [27] M. Magnoni, S. Coli, M. M. Marrocco-Trischitta et al., "Contrast-enhanced ultrasound imaging of periadventitial vasa vasorum in human carotid arteries," *European Journal of Echocardiography*, vol. 10, no. 2, pp. 260–264, 2009.
- [28] L. Xiong, Y.-B. Deng, Y. Zhu, Y.-N. Liu, and X.-J. Bi, "Correlation of carotid plaque neovascularization detected by using contrast-enhanced US with clinical symptoms," *Radiology*, vol. 251, no. 2, pp. 583–589, 2009.
- [29] P.-T. Huang, F.-G. Huang, C.-P. Zou et al., "Contrast-enhanced sonographic characteristics of neovascularization in carotid atherosclerotic plaques," *Journal of Clinical Ultrasound*, vol. 36, no. 6, pp. 346–351, 2008.
- [30] S. Coli, M. Magnoni, G. Sangiorgi et al., "Contrast enhanced ultrasound imaging of intraplaque neovascularization in carotid arteries. Correlation with histology and plaque echogenicity," *Journal of the American College of Cardiology*, vol. 52, no. 3, pp. 223–230, 2008.
- [31] E. Vicenzini, M. F. Giannoni, F. Puccinelli et al., "Detection of carotid adventitial vasa vasorum and plaque vascularization with ultrasound cadence contrast pulse sequencing technique and echo-contrast agent," *Stroke*, vol. 38, no. 10, pp. 2841–2843, 2007.
- [32] F. Shah, P. Balan, M. Weinberg et al., "Contrast-enhanced ultrasound imaging of atherosclerotic carotid plaque neovascularization: a new surrogate marker of atherosclerosis?" *Vascular Medicine*, vol. 12, no. 4, pp. 291–297, 2007.
- [33] D. Staub, A. F. L. Schinkel, B. Coll et al., "Contrast-enhanced ultrasound imaging of the vasa vasorum: from early atherosclerosis to the identification of unstable plaques," *JACC: Cardiovascular Imaging*, vol. 3, no. 7, pp. 761–771, 2010.
- [34] S. Partovi, M. Loebe, M. Aschwanden et al., "Contrast-enhanced ultrasound for assessing carotid atherosclerotic plaque lesions," *American Journal of Roentgenology*, vol. 198, no. 1, pp. W13–W19, 2012.

Research Article

Validation and Development of a New Automatic Algorithm for Time-Resolved Segmentation of the Left Ventricle in Magnetic Resonance Imaging

Jane Tufvesson,^{1,2} Erik Hedström,^{1,3} Katarina Steding-Ehrenborg,¹ Marcus Carlsson,¹
Håkan Arheden,¹ and Einar Heiberg^{1,2,4}

¹Department of Clinical Physiology, Lund University Hospital, Lund University, 221 85 Lund, Sweden

²Department of Numerical Analysis, Centre for Mathematical Sciences, Faculty of Engineering, Lund University, 221 00 Lund, Sweden

³Department of Diagnostic Radiology, Lund University Hospital, Lund University, 221 85 Lund, Sweden

⁴Department of Biomedical Engineering, Faculty of Engineering, Lund University, 221 00 Lund, Sweden

Correspondence should be addressed to Einar Heiberg; enar.heiberg@med.lu.se

Received 1 August 2014; Accepted 12 January 2015

Academic Editor: Peter M. A. Van Ooijen

Copyright © 2015 Jane Tufvesson et al. This is an open access article distributed under the Creative Commons Attribution License, which permits unrestricted use, distribution, and reproduction in any medium, provided the original work is properly cited.

Introduction. Manual delineation of the left ventricle is clinical standard for quantification of cardiovascular magnetic resonance images despite being time consuming and observer dependent. Previous automatic methods generally do not account for one major contributor to stroke volume, the long-axis motion. Therefore, the aim of this study was to develop and validate an automatic algorithm for time-resolved segmentation covering the whole left ventricle, including basal slices affected by long-axis motion. **Methods.** Ninety subjects imaged with a cine balanced steady state free precession sequence were included in the study (training set $n = 40$, test set $n = 50$). Manual delineation was reference standard and second observer analysis was performed in a subset ($n = 25$). The automatic algorithm uses deformable model with expectation-maximization, followed by automatic removal of papillary muscles and detection of the outflow tract. **Results.** The mean differences between automatic segmentation and manual delineation were EDV -11 mL, ESV 1 mL, EF -3% , and LVM 4 g in the test set. **Conclusions.** The automatic LV segmentation algorithm reached accuracy comparable to interobserver for manual delineation, thereby bringing automatic segmentation one step closer to clinical routine. The algorithm and all images with manual delineations are available for benchmarking.

1. Introduction

Cardiovascular magnetic resonance (CMR) imaging can provide diagnostic information about the left ventricle (LV) with clinical parameters such as end-diastolic volume (EDV), end-systolic volume (ESV), ejection fraction (EF), left ventricular mass (LVM), stroke volume (SV), cardiac output (CO), peak ejection rate, peak filling rate, and regional wall thickening. To extract these clinical parameters current clinical practice is to perform endocardial and epicardial delineations manually, which is time consuming and therefore often only performed in end-diastole and end-systole [1]. However, delineations in two frames only will not give peak filling rate and peak ejection rate which require time-resolved segmentation. There is

also a need for segmentation throughout the cardiac cycle in the evaluation of patients with dyssynchrony, for example, to determine first and last segments with contraction [2]. With a typical time resolution of 30 frames per heartbeat, time-resolved manual delineation thus requires 15 times longer than manual delineation in only end-diastole and endsystole.

Automatic segmentation is desirable to reduce both analysis time and observer dependency. The continued need for manual delineation indicates that previously suggested automatic methods do not give satisfactory results. Often they do not cover the whole LV and there is a need for much manual interaction. Petitjean and Dacher [3] pointed out that it is hard to conclude on superiority of any of the previously proposed methods since the results are obtained

on images with different quality and in different patient populations. Also, the methods are validated using different error measurements, both clinical parameters and image processing error measurements. In midventricular slices the errors were by Petitjean and Dacher concluded to be generally satisfactory [3]. However, basal and apical slices generally yield higher errors [4].

Inclusion of all basal slices in the segmentation is important since the atrioventricular plane displacement is a major contributor to cardiac pumping [5, 6]. The long-axis motion causes the outflow tract to move in and out of the imaging plane during a cardiac cycle. Thereby, segmentation of endocardial and epicardial borders become more difficult in the most basal slices and an automatic detection of the long-axis motion is needed. To our knowledge three studies have included slices with outflow tract [4, 7, 8]. However, in the study by Jolly et al. [4] the detection of outflow tract was not defined, in the study by Hu et al. [7] the outflow tract was detected but the detection of long-axis motion was not defined, and finally in the study by Codella et al. [8] the user defined the most basal slice in both end-diastole and end-systole and thus the long-axis motion was not detected by the algorithm.

The aims of this study were (1) to develop an algorithm for time-resolved LV segmentation covering the whole LV, from the basal slices with outflow tract to the apex, and (2) to validate this new algorithm with regard to clinical parameters and image processing errors for comparison to previous algorithms, and (3) to provide software as well as images with manual delineation to enable benchmarking for future algorithms.

2. Methods

2.1. Study Population and Design. In total 90 subjects were included in the study, both patients referred for clinical evaluation of known or suspected coronary artery disease as well as healthy subjects and athletes. The subjects were scanned using a 1.5T MR scanner (Philips Intera CV, Philips, Best, The Netherlands) with a cardiac synergy coil. The sequence used was a balanced steady state free precession (bSSFP) sequence with retrospective ECG triggering. Typical imaging parameters were repetition time 2.8 ms, echo time 1.4 ms, flip angle 60°, SENSE factor of 2, spatial reconstructed resolution of $1.4 \times 1.4 \times 8$ mm, and 30 reconstructed time frames per cardiac cycle (acquired spatial resolution $2.3 \times 2.7 \times 8$ mm and temporal resolution 50 ms).

The subjects were divided into a training set ($n = 40$) and a test set ($n = 50$). The training set was used for the development and optimization of the algorithm, and the test set was used to validate the algorithm. The training set consists of 20 patients, 13 healthy volunteers, and 7 athletes. The test set consists of 20 patients, 20 healthy volunteers, and 10 athletes. Manual segmentation was performed for all slices in end-diastole and end-systole in both the training set and the test set by an experienced clinician (ErH with 14 years of CMR experience). The training set was reviewed for consensus by another experienced clinician (HA with 20 years of CMR experience). A subset of 25 subjects from the

test set (10 patients, 10 healthy volunteers, and 5 athletes) was used for second observer analysis, by another experienced clinician (MC with 14 years of CMR experience).

Image quality was representative of images likely found in daily clinical routine. Differences in clinical left ventricular parameters EDV, ESV, EF, LVM, SV, and CO between patients and healthy subjects in the test set were nonsignificant for all parameters except SV. The training set and test set with manual delineations are available upon request to the corresponding author to enable direct comparison to other methods.

2.2. Automatic Segmentation Algorithm. An automatic algorithm was developed for time-resolved segmentation of the endocardial and epicardial borders of the LV covering all ventricular slices from the most basal slices with outflow tract to the apex. The user input required by the algorithm is the definition of slices to analyze as the most basal slice and most apical slice containing any myocardium. The slices to analyze were in this study automatically selected to be the same as selected for the reference manual delineation. The algorithm was implemented in the freely available cardiac image analysis software Segment (<http://segment.heiberg.se/>) [9].

The algorithm is based on a deformable model framework. Deformable model is a segmentation method based on the idea of deforming a model to the location and shape of minimal energy in a force field. The model to deform is in this study a model of either the endocardial or the epicardial border. The initialization of the model is based on the image to segment and the initialization is further described in Step 3 of the algorithm. The force field which deforms the model consists of a weighted sum of image-dependent and model-dependent forces. The image-dependent forces are a balloon force image, calculated from image intensities and an edge force image, based on edge detection. The model-dependent forces are based on the curvature within the slice, between adjacent slices and between time frames of the cardiac cycle. The weighting of the forces in the deformable model was optimized based on the training set to obtain parameters suitable for the image type and quality in the training set. The optimization is further described in Deformable Model Optimization section.

Step 1 of the automatic segmentation algorithm is to define the center of the left ventricle, which is needed to calculate the balloon images in Step 2 and to initialize the deformable model in Step 3. Steps 4 and 5 use the deformable model for endocardial and epicardial segmentation. In Steps 6–8 the segmentation resulting from the deformable model is modified to account for the papillaries and the outflow tract. All steps are further described below.

The steps of the algorithm are as follows:

- (1) definition of the left ventricular center point,
- (2) calculation of balloon image,
- (3) initialization of segmentation,
- (4) endocardial segmentation,
- (5) epicardial segmentation,

- (6) exclusion of detached papillaries,
- (7) detection of outflow tract,
- (8) exclusion of attached papillaries.

Definition of the Left Ventricular Center Point (Step 1). First the center of the whole heart is defined from the largest bright region by smoothing and thresholding the image. The center of the left ventricular cavity is then defined as the center of gravity of the large, bright region closest to the right of the whole heart center point.

Calculation of Balloon Image (Step 2). The balloon force, which is the most important part of the deformable model, is defined using an expectation maximization (EM) algorithm. The balloon force drives the expansion and contraction of the curve and thereby should be a distinction between what to include and exclude in the endocardial and epicardial segmentations. The balloon image is mapped from the image intensities by estimating the distribution of intensities in the images. For endocardial segmentation the intensity distributions for blood and myocardium are estimated. In addition for epicardial segmentation, the intensity distribution of tissues surrounding the left ventricle is estimated. An EM-algorithm was utilized to estimate assumed Gaussian distribution of intensities for blood, myocardium, and surrounding tissues. As an initialization to the EM-algorithm, the mean and standard deviation for the intensity of blood were estimated in a cylinder with radius of 10 mm placed at the left ventricular center point. The endocardial balloon image was calculated as the Gaussian distribution for blood divided by the sum of the Gaussian distributions for blood and myocardium. The epicardial balloon image was calculated as the Gaussian distribution for myocardium divided by the sum of the Gaussian distributions for blood, myocardium, and surrounding tissues. The balloon force is positive for intensity values to include and negative for intensities to exclude and the balloon force was rescaled to the interval -1 to 1 . Figure 1 shows the results from calculation of the balloon image.

Initialization of Segmentation (Step 3). To initialize both the endocardial and epicardial segmentations the endocardial balloon image is used. The endocardium is initialized at an estimated midmural center line and the epicardium is initialized as an estimate of the epicardial border. The initialization is divided into five substeps.

- (1) Thresholding the endocardial balloon image at zero to find regions representative of blood. Balloon force zero is representative of the probability of myocardium being equal to the probability of blood.
- (2) Finding the left ventricular blood pool as a region in the thresholded image which surrounds the left ventricular center point.
- (3) Estimating the endocardial border as the convex hull of the left ventricular blood pool. The convex hull is an estimation of the endocardial border excluding papillaries.

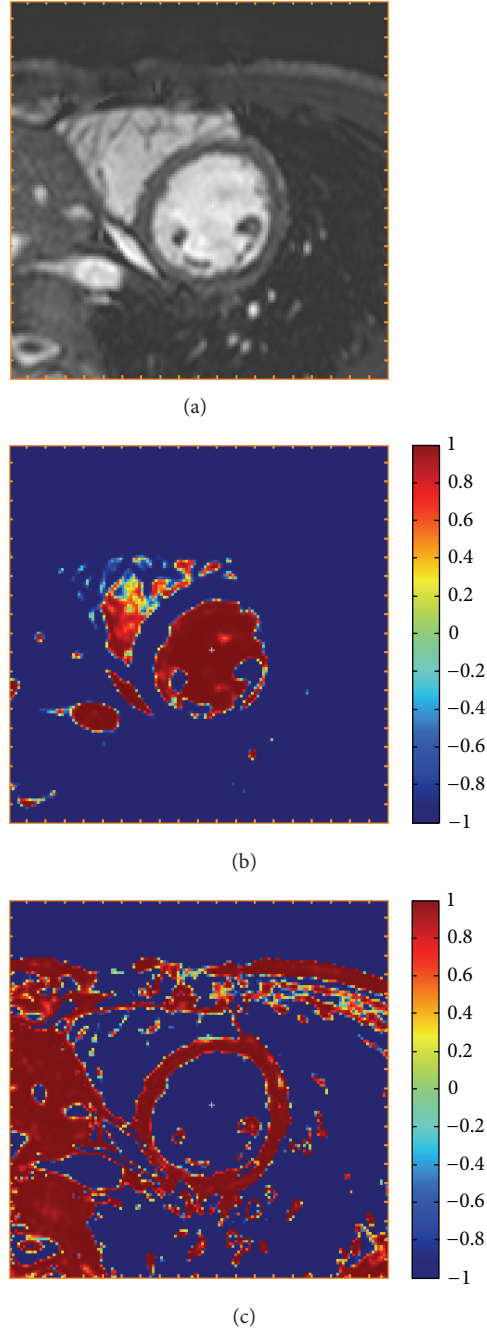


FIGURE 1: Calculation of balloon force (Step 2). A midventricular slice of a short-axis stack (a) and the endocardial (b) and epicardial (c) balloon force images calculated in Step 2 with the automatic algorithm. The color scale indicates how the deformable model should expand to include pixels with positive values (red) and contract to exclude pixels with negative values (blue).

- (4) Estimating the left ventricular wall thickness in each time frame by finding the mean distance from the initial curve to the right ventricular blood pool.
- (5) (a) Expanding the endocardial border estimated in Step 3 by a half wall thickness to get the endocardial initialization.

(b) Expanding the endocardial border estimated in Step 3 by one full wall thickness to get the epicardial initialization.

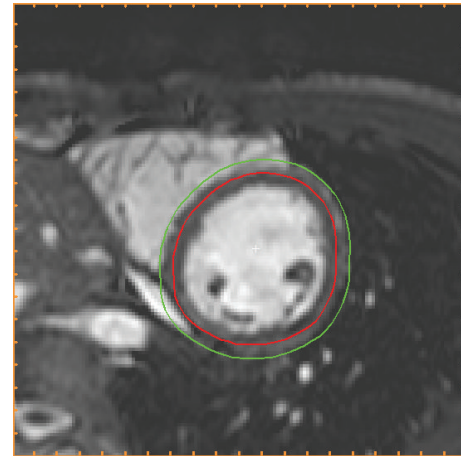
Figure 2 shows the initialization of endocardium and epicardium.

Endocardial Segmentation (Step 4). For endocardial segmentation, the deformable model is used with endocardial initialization, endocardial balloon force, and weighting of the forces optimized for endocardial segmentation. The deformable model formalism used has previously been described [10]. In short, in the deformable model, the node forces are normalized and projected onto the curve normal and the parameterization of the node points is kept equidistant. The deformable model includes balloon force, edge force, curvature force, temporal acceleration, and damping forces.

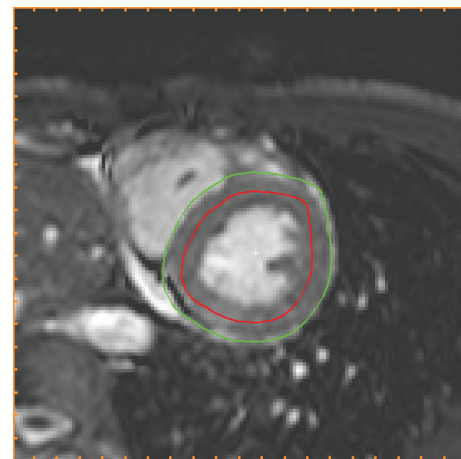
Epicardial Segmentation (Step 5). For epicardial segmentation, the deformable model is used with epicardial initialization, epicardial balloon force, and weighting of the forces optimized for epicardial segmentation. The epicardial balloon force is negative for blood and other tissues surrounding the myocardium and hence the deformable model will contract to not include any blood. To get an epicardial segmentation which expands outwards from the endocardial segmentation the epicardial balloon force was modified to be zero for all pixels inside the endocardium.

Exclusion of Detached Papillaries (Step 6). For measurement of ventricular volumes, the clinical standard is to exclude the papillaries from the myocardium and therefore the algorithm should also exclude the papillaries. Since papillary muscles have the same intensity as myocardium and the main driving force in the deformable model, the balloon force, is based on intensity, the algorithm may have difficulties with excluding the papillaries from the myocardium hence including the papillaries within the endocardial segmentation. The exclusion of papillaries is divided into two steps, this step and Step 8. In this step, detached papillaries are included inside the endocardial segmentation by taking the convex hull of the endocardial segmentation and refining the segmentation. The segmentation is refined by using the deformable model with a modified endocardial balloon force. The endocardial balloon force is modified by setting the balloon force to zero for papillaries, which are detected as pixels inside the convex hull with a negative balloon force.

Detection of Outflow Tract (Step 7). The deformable model gives endocardial and epicardial segmentation in all selected slices and time frames. Thereafter, long-axis motion and outflow tract are detected and in the basal slices the segmentation is adjusted accordingly. The detection of the long-axis motion is based on detecting sectors in the basal slices for which the intensities between the endocardial and epicardial segmentation are not typical for myocardium and sectors with a mean wall thickness of less than 2 millimeters. Basal slices were for detection of outflow tract defined as the most basal 40% of the ventricular length in end-diastole and all slices were divided into 24 sectors circumferentially.



(a)



(b)

FIGURE 2: Initialization of segmentation (Step 3). The initializations of endocardial (red) and epicardial (green) borders resulting from Step 3 in the algorithm, shown in end-diastole (a) and end-systole (b) in the midventricular slice also used for Figure 1. The endocardial initialization is an estimation of the midmural line and the epicardial initialization is an estimation of the epicardial border.

The intensities in basal slices are compared to intensities in all slices. Sectors with a mean intensity 2 SD above the mean are marked as sectors to remove. Sectors can only be marked as sectors to remove if the sectors are also removed in a more basal slice. Sectors to be removed are smoothed over time and circumferentially in each slice and a morphological opening is performed to get a cohesive region to remove. To remove the marked sectors a straight line is drawn for both endocardium and epicardium. Thereby a D-shaped segmentation is obtained after adjustment for presence of outflow tract. Figure 3 shows the segmentation in a basal slice before and after the detection of outflow tract.

Exclusion of Attached Papillaries (Step 8). To exclude papillaries which are closely attached to the left ventricular wall in the segmentation, it is not sufficient to take convex hull and refine as in Step 6 since there is no blood volume which

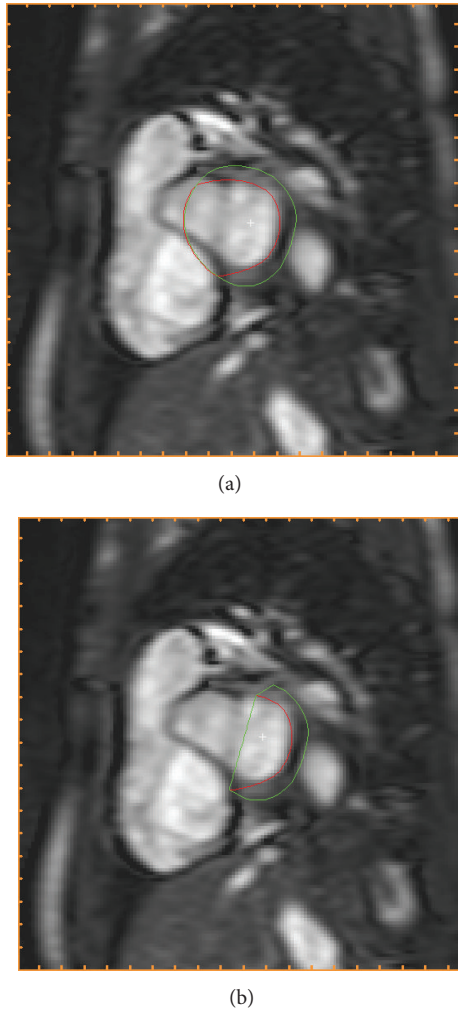


FIGURE 3: Detection of outflow tract (Step 7). The endocardial (red) and epicardial (green) segmentations are shown prior to the detection of outflow tract in Step 7 (a) and after adjustment of segmentation for presence of outflow tract (b) in the same basal slice in end-diastole.

can guide the deformable model on where to expand the segmentation. Therefore, in this step an expansion of the endocardial segmentation is calculated based on a constant papillary volume over time and a similar position of the papillary muscles over time. Sectors with a lower papillary volume inside the endocardial segmentation than in end-diastole are expanded to include more papillary volume. The long-axis displacement found when detecting the outflow tract in Step 7 is used to map slices in end-diastole to the corresponding slice in all other timeframes. Expansion of the endocardial segmentation is restricted to slices below the outflow tract in order to not falsely take the mitral valve into account as papillary muscle.

2.3. Deformable Model Optimization. Weighting of the forces in the deformable model was optimized with a steepest-descent method in a 2-factorial design by using the images in the training set with manual delineation as reference

standard. For the endocardial segmentation the error to minimize was the sum of the relative errors of the end-diastolic volume, and the relative number of falsely segmented pixels in end-diastole by comparing the automatic segmentation to manual delineation. Only the end-diastolic errors were included since the errors in end-systole are largely influenced by the presence of papillary muscles which is not especially accounted for within the deformable model.

For the epicardial segmentation the error to minimize in the optimization was the sum of the relative errors of left ventricular mass, in end-diastole and end-systole, and the relative number of falsely segmented pixels, in end-diastole and end-systole. In order to not take into account any volumetric errors in left ventricular mass given by the automatic endocardial segmentation, the left ventricular mass was during optimization calculated using the manual delineation of endocardium.

2.4. Statistical Analyses. In the test set the difference between manual delineation and automatic segmentation was computed for the clinical parameters EDV, ESV, EF, LVM, SV, and CO as well as the image processing error measurements dice similarity coefficient (DSC) [11] and point to curve distance (P2C).

The errors for clinical parameters are given both as absolute errors and as percentage of the result from the manual delineation. Paired t -test was performed with significance level $P < 0.05$ to test for difference compared to manual delineations. A linear regression was performed for the clinical parameters and a regression R -value and corresponding P -value were calculated. The DSC is calculated as two times the volume of the intersection of two regions divided by the sum of the volume for those regions [11]. The DSC is therefore 0 if the regions do not overlap and 1 if the regions overlap perfectly. The P2C error was calculated as the distance between two borders in each slice and time frame where both borders were present. To calculate the distance both borders were resampled to be represented by 80 points spaced at every 4.5 degrees. The DSC and P2C errors were calculated between automatic segmentation and manual delineation for both endocardial and epicardial segmentation separately. The DSC and P2C error were calculated as a mean over all slices in both end-diastole and end-systole as well as separately for end-diastole and end-systole and separately for basal, midventricular, and apical slices. Basal, midventricular, and apical slices were defined as one third each of the ventricular length in both end-diastole and end-systole. All errors were reported as mean \pm SD.

In the subset for which second observer manual delineation was performed the same error calculations as for the full test set were performed for automatic segmentation versus reference manual delineation and for second observer manual delineation versus reference manual delineation.

3. Results

Automatic segmentation was performed and compared to manual delineation in the test and compared to interobserver variability in a second observer subset. In one patient

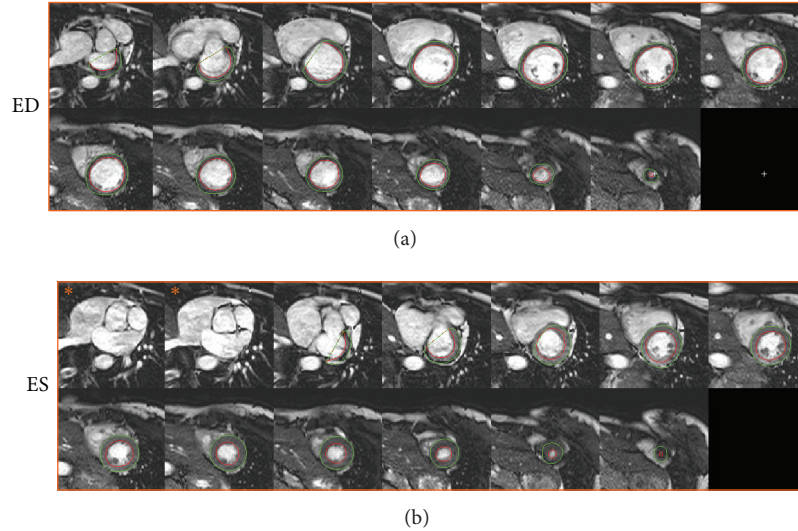


FIGURE 4: Example of segmentation in end-diastole and end-systole. An example of automatic segmentation is shown in end-diastole (a) and end-systole (b). Each panel shows the short axis stack covering the left ventricle from base to apex with endocardial (red) and epicardial (green) segmentations. Note how the outflow tract has moved out of the two most basal slices in end-systole (b, images marked *), compared to end-diastole (a) and that the algorithm has automatically corrected for this long-axis motion.

the automatic segmentation failed due to a severe bright fold-in artifact connecting the right and left ventricle. This patient was excluded from further analysis resulting in a test set of 49 patients and a second observer subset of 24 patients. Figure 4 shows an example of automatic segmentation in all slices in end-diastole and end-systole. A comparison between automatic segmentation and manual delineation can be seen in Figure 5 for a basal, midventricular, and apical slice in end-diastole and end-systole. In the additional file a time-resolved 3D-rendering of left ventricle shows the long-axis motion of the epicardial surface resulting from the automatic segmentation algorithm. The differences between automatic segmentation and manual delineation for clinical parameters were EDV -11 ± 11 mL ($R = 0.96$), ESV 1 ± 10 mL ($R = 0.95$), EF $-3 \pm 4\%$ ($R = 0.86$), LVM 4 ± 15 g ($R = 0.87$), SV -12 ± 8 mL ($R = 0.92$), and CO -0.7 ± 0.5 L/min ($R = 0.94$) (Table 1, Figures 6 and 7). The image processing error measurements were for endocardial segmentation DSC = 0.91 ± 0.03 and P2C = 2.1 ± 0.5 mm and for epicardial segmentation DSC = 0.93 ± 0.02 and P2C = 2.1 ± 0.5 mm as mean over all slices and both end-diastole and end-systole (Table 2). End-diastolic image processing error measurements performed better than end-systolic (Table 2). Midventricular slices performed better than basal and apical slices (Table 3).

In the subset for second observer analysis the differences between second observer manual delineation and reference manual delineation were EDV 10 ± 4 mL, ESV 5 ± 5 mL, EF $0 \pm 2\%$, LVM -7 ± 9 g, SV 5 ± 6 mL, and CO 0.3 ± 0.4 L/min compared to the differences between automatic segmentation and the reference manual delineation which were EDV -9 ± 10 mL, ESV 3 ± 8 , EF $-3 \pm 3\%$, LVM 2 ± 16 g, SV -12 ± 8 mL, and CO -0.7 ± 0.4 L/min (Table 4). The results for the image processing error measurements DSC and P2C for the second observer subset are given in Tables 5 and 6.

TABLE 1: Clinical parameters in test set. Results for clinical parameters in the full test set ($n = 49$) as differences between automatic segmentation and manual delineation.

	Absolute difference	Relative difference	P value
EDV	-11 ± 11 mL	$-6 \pm 6\%$	<0.01
ESV	1 ± 10 mL	$1 \pm 13\%$	0.57
EF	$-3 \pm 4\%$	$-5 \pm 7\%$	<0.01
LVM	4 ± 15 g	$4 \pm 14\%$	0.07
SV	-12 ± 8 mL	$-11 \pm 8\%$	<0.01
CO	-0.7 ± 0.5 L/min	$-11 \pm 8\%$	<0.01

Absolute and relative values are expressed as mean \pm SD. EDV = end-diastolic volume, ESV = end-systolic volume, EF = ejection fraction, and LVM = left ventricular mass.

TABLE 2: Image processing error measurement in test set. Image processing error measurements in the full test set ($n = 49$) as dice similarity coefficient (DSC) and point to curve (P2C) between automatic segmentation and manual delineation.

	Dice similarity coefficient (DSC)	Point to curve (P2C)
Endocardium overall	0.91 ± 0.03	2.1 ± 0.5 mm
Endocardium ED	0.93 ± 0.03	1.9 ± 0.6 mm
Endocardium ES	0.85 ± 0.04	2.3 ± 0.5 mm
Epicardium overall	0.93 ± 0.02	2.1 ± 0.5 mm
Epicardium ED	0.94 ± 0.02	2.1 ± 0.6 mm
Epicardium ES	0.91 ± 0.03	2.2 ± 0.7 mm

Differences are expressed as mean \pm SD. For a perfect overlap between the regions DSC should be 1 and P2C should be 0. ED = end diastole, ES = end systole.

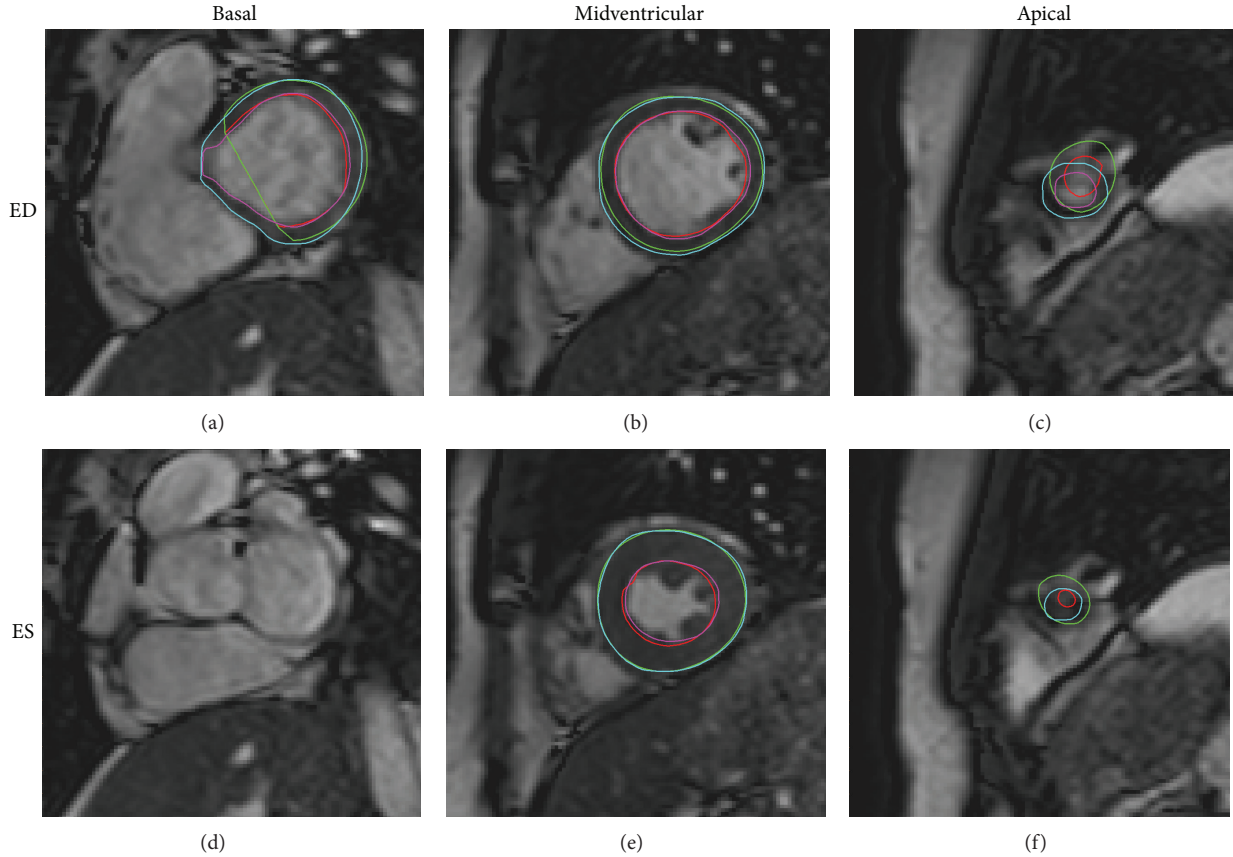


FIGURE 5: Automatic segmentation compared to manual delineation in a basal, midventricular and apical slice. Automatic segmentation (endocardium in red and epicardium in green) and manual delineation (endocardium in pink and epicardium in light blue) shown in end-diastole ((a), (b), and (c)) and end-systole ((d) (e), and (f)) for the most basal slice with outflow tract moving out of the imaging plane ((a), (d)), a midventricular slice with papillaries ((b), (e)) and an apical slice with minimal lumen in end-systole ((c), (f)).

TABLE 3: Image processing error measurements in test set divided into slice sections. Image processing error measurements in the full test set ($n = 49$) as dice similarity coefficient (DSC) and point to curve (P2C) between automatic segmentation and manual delineation.

	Dice similarity coefficient (DSC)	Point to curve (P2C)
Endocardium basal	0.88 ± 0.06	2.7 ± 1.0 mm
Endocardium midventricular	0.94 ± 0.02	1.6 ± 0.4 mm
Endocardium apical	0.89 ± 0.03	2.1 ± 0.7 mm
Epicardium basal	0.89 ± 0.05	3.3 ± 1.2 mm
Epicardium midventricular	0.96 ± 0.02	1.3 ± 0.5 mm
Epicardium apical	0.92 ± 0.03	2.2 ± 0.8 mm

Differences are expressed as mean \pm SD. For a perfect overlap between the regions DSC should be 1 and P2C should be 0. Basal, midventricular, and apical sections are defined as 1/3 each of the ventricular length in end diastole and end systole separately.

4. Discussion

We have developed an automatic algorithm for time-resolved LV segmentation in magnetic resonance cine balanced steady

state free precession (MRSSFP) images. The segmentation is performed in all time frames and all ventricular slices including the slices in which the mitral valve plane and outflow tract move in and out of the slice during a heartbeat. The only manual user input is definition of the most basal and most apical slices including any myocardium in end-diastole. This study brings a state-of-the-art left ventricle segmentation tool to applied clinical research, as the software and source code are provided in open access to researchers. Furthermore, both algorithm and images with ground truth manual delineations are made available for benchmark against future LV segmentation algorithms.

The major algorithmic contributions towards a clinically applicable automatic segmentation method in this study is (1) the use of an EM-algorithm to calculate the distinction between blood, myocardium, and tissues surrounding the heart, (2) removal of papillary muscles by convex hull expansion and expansion to get constant papillary volume, (3) the detection of the outflow tract when moving in and out of the imaging plane, and (4) usage of an optimization step to tune otherwise arbitrary set parameters to the images used.

The algorithm was validated in a test set of 49 subjects and both the clinical parameters, EDV, ESV, EF, and LVM, and the image processing error measurements, DSC and P2C, were

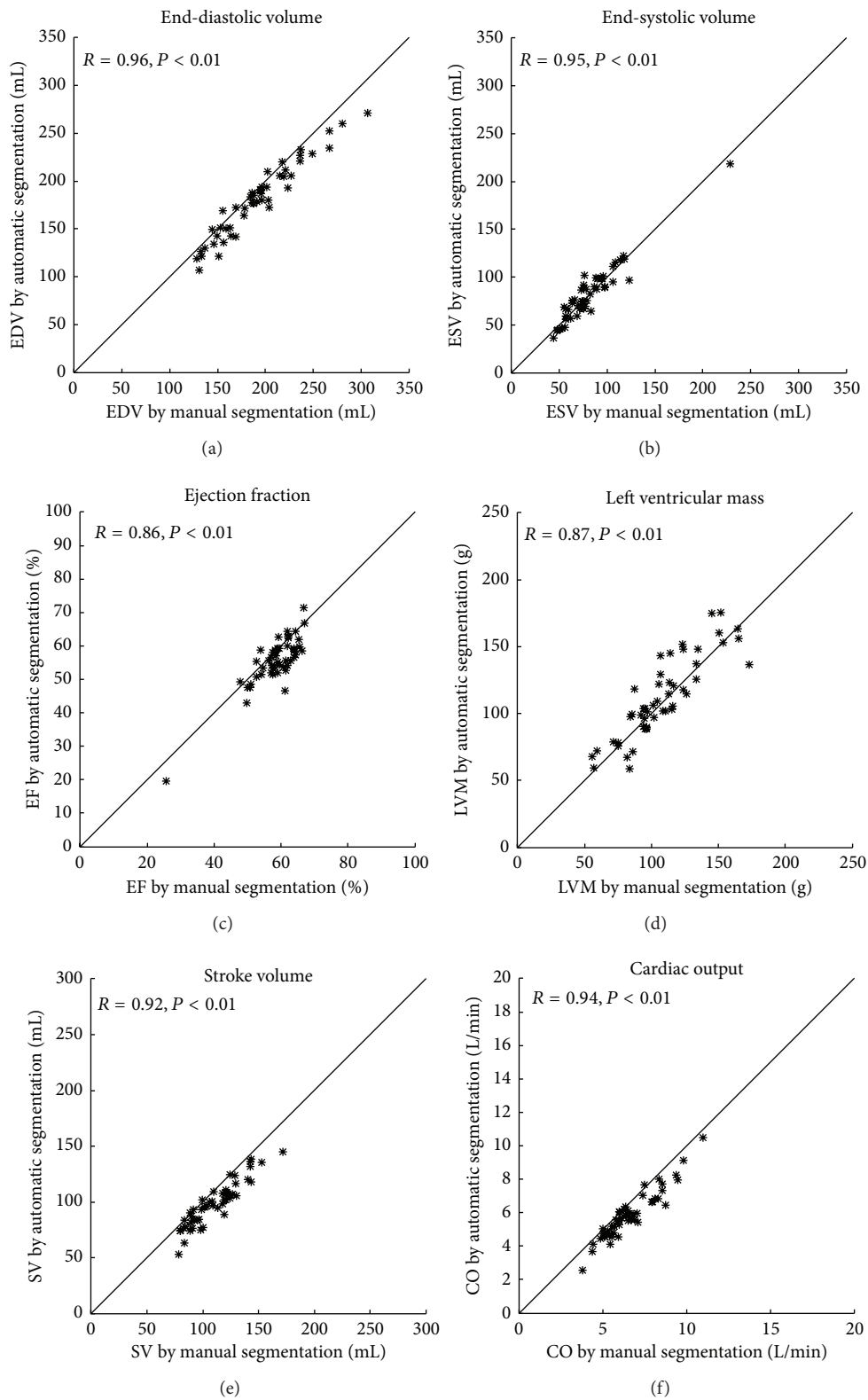


FIGURE 6: Correlations between automatic segmentation and manual delineation in the test set. Automatic segmentation plotted against manual delineation for end-diastolic volume (EDV, (a)), end-systolic volume (ESV, (b)), ejection fraction (EF, (c)), left ventricular mass (LVM, (d)), stroke volume (SV, (e)) and cardiac output (CO, (f)). The line indicates the line of identity.

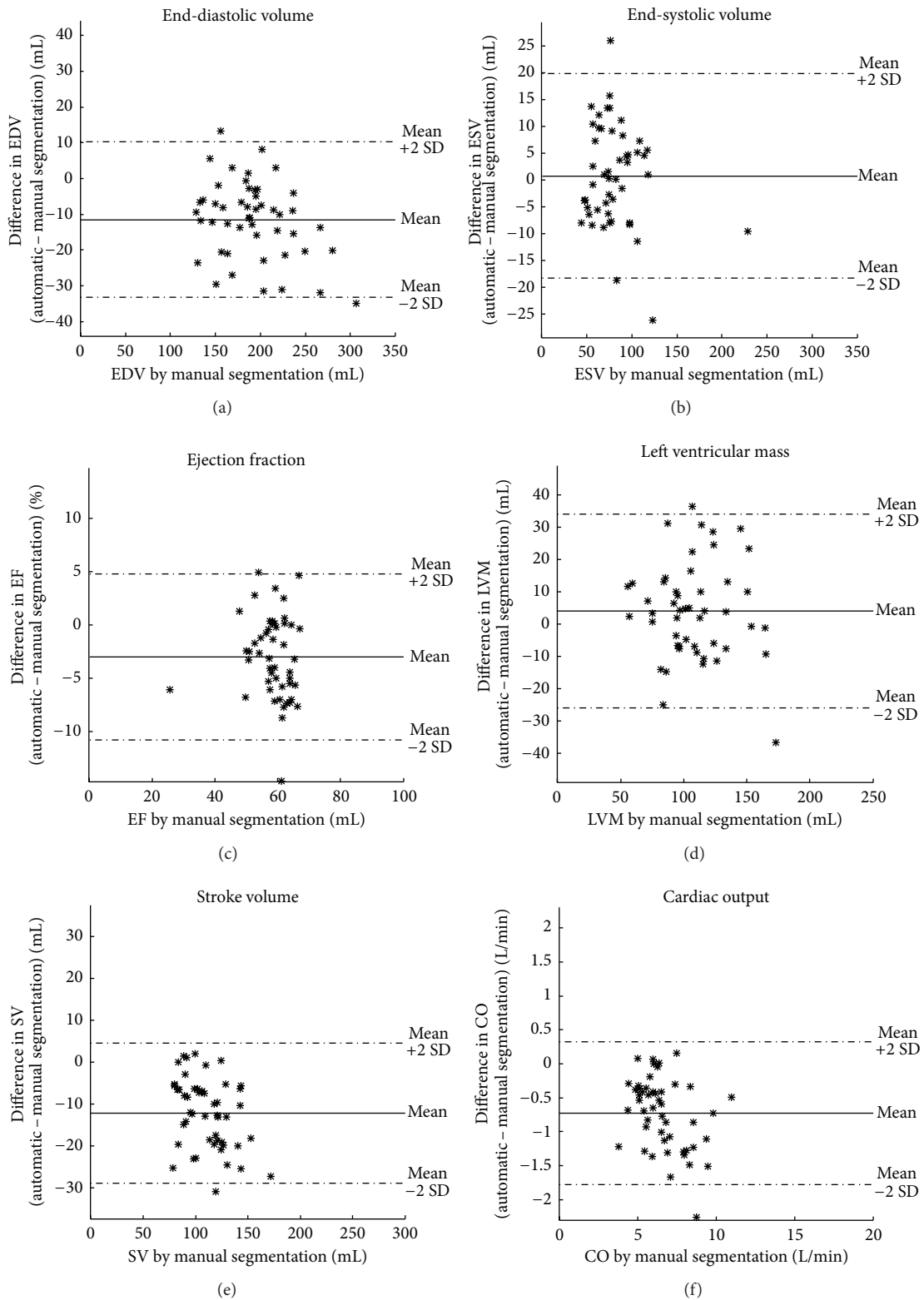


FIGURE 7: Bias between automatic segmentation and manual delineation in the test set. Differences between automatic segmentation and manual delineation plotted against manual delineation for end-diastolic volume (EDV, (a)), end-systolic volume (ESV, (b)), ejection fraction (EF, (c)), left ventricular mass (LVM, (d)), stroke volume (SV, (e)) and cardiac output (CO, (f)). Solid line indicates mean and dashed lines indicate mean \pm 2SD.

TABLE 4: Clinical parameters in second observer subset. Differences for clinical parameters in the second observer subset ($n = 24$) for second observer manual delineation versus manual reference delineation and for automatic segmentation versus manual reference delineation.

	Automatic segmentation versus manual reference			Second observer versus manual reference		
	Absolute difference	Relative difference	<i>P</i> value	Absolute difference	Relative difference	<i>P</i> value
EDV	-9 ± 10 mL	$-5 \pm 5\%$	<0.01	10 ± 4 mL	$6 \pm 2\%$	<0.01
ESV	3 ± 8 mL	$4 \pm 12\%$	0.1	5 ± 5 mL	$6 \pm 6\%$	<0.01
EF	$-3 \pm 3\%$	$-6 \pm 6\%$	<0.01	$0 \pm 2\%$	$-1 \pm 4\%$	0.44
LVM	2 ± 16 g	$3 \pm 13\%$	0.55	-7 ± 9 g	$-7 \pm 8\%$	<0.01
SV	-12 ± 8 mL	$-10 \pm 6\%$	<0.01	5 ± 6 mL	$5 \pm 5\%$	<0.01
CO	-0.7 ± 0.4 L/min	$-10 \pm 6\%$	<0.01	0.3 ± 0.4 L/min	$5 \pm 5\%$	<0.01

Absolute and relative difference expressed as mean \pm SD. EDV = end-diastolic volume, ESV = end-systolic volume, EF = ejection fraction, and LVM = left ventricular mass.

TABLE 5: Image processing error measurements in second observer subset. Image processing error measurements in the second observer subset ($n = 24$) as dice similarity coefficient (DSC) and point to curve (P2C) for second observer manual delineation versus manual reference delineation and for automatic segmentation versus manual reference delineation.

	Automatic segmentation versus manual reference		Second observer versus manual reference	
	DSC	P2C	DSC	P2C
Endocardium overall	0.91 ± 0.02	2.0 ± 0.4 mm	0.95 ± 0.01	1.2 ± 0.2 mm
Endocardium ED	0.93 ± 0.02	1.8 ± 0.5 mm	0.96 ± 0.01	1.1 ± 0.3 mm
Endocardium ES	0.85 ± 0.04	2.4 ± 0.5 mm	0.92 ± 0.03	1.4 ± 0.3 mm
Epicardium overall	0.93 ± 0.01	2.2 ± 0.4 mm	0.96 ± 0.01	1.2 ± 0.33 mm
Epicardium ED	0.94 ± 0.01	2.0 ± 0.5 mm	0.97 ± 0.01	1.1 ± 0.4 mm
Epicardium ES	0.91 ± 0.02	2.4 ± 0.6 mm	0.95 ± 0.01	1.4 ± 0.4 mm

Difference are expressed as mean \pm SD. For a perfect overlap between the regions DSC should be 1 and P2C should be 0. ED = end diastole, ES = end systole.

TABLE 6: Image processing error measurements in second observer set divided into slice sections. Image processing error measurements in the second observer subset ($n = 24$) as dice similarity coefficient (DSC) and point to curve (P2C) for second observer manual delineation versus manual reference delineation and for automatic segmentation versus manual reference delineation.

	Automatic segmentation versus manual reference		Second observer versus manual reference	
	DSC	P2C	DSC	P2C
Endocardium basal	0.88 ± 0.06	2.7 ± 1.1 mm	0.94 ± 0.02	1.5 ± 0.4 mm
Endocardium midventricular	0.94 ± 0.01	1.6 ± 0.4 mm	0.96 ± 0.01	1.1 ± 0.3 mm
Endocardium apical	0.90 ± 0.03	2.0 ± 0.7 mm	0.94 ± 0.01	1.1 ± 0.3 mm
Epicardium basal	0.89 ± 0.05	3.3 ± 1.2 mm	0.95 ± 0.02	1.5 ± 0.6 mm
Epicardium midventricular	0.96 ± 0.01	1.3 ± 0.4 mm	0.97 ± 0.01	0.8 ± 0.2 mm
Epicardium apical	0.92 ± 0.02	2.3 ± 0.7 mm	0.95 ± 0.01	1.4 ± 0.5 mm

Difference are expressed as mean \pm SD. For a perfect overlap between the regions DSC should be 1 and P2C should be 0. Basal, midventricular, and apical sections are defined as 1/3 each of the ventricular length in end diastole and end systole separately.

reported to allow comparison to errors reported in previous studies. The proposed algorithm has a DSC and P2C error similar to the ones reported in previous studies [3, 4, 12–14]. However, direct comparison between studies is difficult due to differences in methodology. In previous studies it is not defined either how the basal slices were selected, or if the basal slices were excluded or defined separately for end-diastole and end-systole thereby not including the long-axis motion. Furthermore, results may not be directly comparable due to differences in patient population and sequences used for imaging. For instance the test set in the MICCAI challenge [3] was acquired without parallel acquisition techniques which is now clinical standard. In the sequel challenge STACOM [14] not all results were derived using manual delineation as

ground truth. A new test set and training set were therefore acquired for this study in order to have images with parallel acquisition, covering all slices and with manual delineation as ground truth. In comparison to the present study, Codella et al. [8, 15] reported better results for all clinical parameters, which is expected with the higher level of user input used in their algorithm LV-METRIC. The present study has a low level of user input with only a selection of slices to include in segmentation. Hu et al. [7] developed a detection of the outflow tract and reported DSC and P2C similar to the present study. However, their method description does not define detection of the outflow tract moving out of the imaging plane. Since the long-axis motion is a major contributor to cardiac pumping [5] it is important to include

the basal slices and account for the contraction along the long-axis. Segmentation of the most basal slices with outflow tract becomes more difficult when the myocardium moves in and out of the imaging plane. The proposed algorithm includes all slices with results similar to previous studies not including all basal slices, which brings the algorithm one step closer to automatic LV segmentation applicable for the clinical routine.

The proposed algorithm was compared to interobserver variability of manual delineation in a subset as a major goal of automatic segmentation methods is to reduce observer dependency. The proposed method showed a bias comparable to interobserver variability by manual delineation for the clinical parameters, lower or similar bias for EDV, ESV, and LVM and higher bias for EF, SV, and CO. The SD for the clinical parameters was approximately twice the value found for interobserver variability. The interobserver variability measured as P2C error was overall 1.2 mm compared to 2 mm reported in a previous study [16]. The interobserver variability measured as clinical parameters was overall comparable to those reported in previous studies [17–19]. The standard deviation of LVM for interobserver variability was in this study 7 g which falls within the range of published values from 5 g in a normal material for gradient echo images [20] to 14 g in a study where bSSFP short axis delineations were compared to long-axis delineations [21]. The large range in interobserver variability measurements reported in the literature can most likely be explained by differences in methodology used in the basal regions, differences in image quality, and amount of consensus training. Again many of the studies report differences differently and direct comparisons are difficult.

In order for the algorithm to reach results fully comparable to interobserver variability between two experienced observers, further improvement is needed. By improving the use of the EM-algorithm and by improving the detection of papillary muscles and outflow tract both the accuracy and precision may be reduced. The algorithm might also be further improved to have a smoother segmentation over the cardiac cycle by using more than two time frames in the optimization of parameters and hence possibly get a higher weight on the time dependent parameter. As for all automatic segmentation algorithms a manual approval and possibly manual corrections are needed in a clinical setting.

A limitation to the study is that the training and test set used only patients with coronary artery disease. Other patient categories with, for example, left ventricular dyssynchrony or pronounced trabeculations may need special consideration in the algorithm and further validation.

5. Conclusion

We have developed an automatic algorithm for time-resolved segmentation of all LV slices containing any myocardium in magnetic resonance balanced steady state free precession images. The algorithm was quantitatively validated in 49 subjects and both algorithm and images with reference manual delineations are available for benchmark against future LV segmentation algorithms. The algorithm showed a bias comparable to interobserver variability between two

experienced observers for the clinical parameters EDV, ESV, EF, LVM, SV, and CO. With a dice and P2C error similar to previous studies the proposed algorithm is favorable due to low level of user input and automatic correction for long-axis motion. The algorithm is one step closer to an automatic segmentation applicable for clinical routine.

Disclosure

Einar Heiberg is the founder of Medviso AB, Lund, Sweden, which sells a commercial version of the otherwise freely available software Segment. Jane Tufvesson is employed by Medviso AB on a part-time basis.

Conflict of Interests

All other authors declare that there is no conflict of interests regarding the publication of this paper.

Authors' Contribution

All authors contributed to concept and design of the study, input to the development of the automatic segmentation algorithm, and revised the paper. All authors read and approved the final paper. Jane Tufvesson developed and implemented the automatic segmentation algorithm, analyzed and interpreted segmentation results, and drafted the paper. Erik Hedström performed manual delineation in training set and test set. Katarina Steding-Ehrenborg included normal subjects and athletes to the study. Marcus Carlsson performed second observer manual delineation. Håkan Arheden performed consensus reading of the manual delineation in training set. Einar Heiberg conceived the study.

Acknowledgments

The authors would like to acknowledge Ann-Helen Arvidsson and Christel Carlander, both with the Lund Cardiac MR Group, for their skillful assistance with image acquisition, and Joey Ubachs for inclusion of patients to the study. This study has been funded by the Swedish Research Council (2011-3916, 2008-2949, and 2012-4944), The Swedish Heart and Lung Foundation, The Medical Faculty of Lund University, Sweden, and Region of Scania, Sweden.

References

- [1] J. Schulz-Menger, D. A. Bluemke, J. Bremerich et al., "Standardized image interpretation and post processing in cardiovascular magnetic resonance: Society for Cardiovascular Magnetic Resonance (SCMR) Board of Trustees Task Force on Standardized Post Processing," *Journal of Cardiovascular Magnetic Resonance*, vol. 15, no. 1, article 35, 2013.
- [2] P. Foley, K. Khadjooi, J. Ward et al., "Radial dyssynchrony assessed by cardiovascular magnetic resonance in relation to left ventricular function, myocardial scarring and QRS duration in patients with heart failure," *Journal of Cardiovascular Magnetic Resonance*, vol. 11, no. 1, article 50, 2009.

- [3] C. Petitjean and J.-N. Dacher, "A review of segmentation methods in short axis cardiac MR images," *Medical Image Analysis*, vol. 15, no. 2, pp. 169–184, 2011.
- [4] M. P. Jolly, H. Xue, L. Grady, and J. Guehring, "Combining registration and minimum surfaces for the segmentation of the left ventricle in cardiac cine MR images," in *Medical Image Computing and Computer-Assisted Intervention*, vol. 12, pp. 910–918, Springer, Berlin, Germany, 2009.
- [5] M. Carlsson, M. Ugander, H. Mosén, T. Buhre, and H. Arheden, "Atrioventricular plane displacement is the major contributor to left ventricular pumping in healthy adults, athletes, and patients with dilated cardiomyopathy," *The American Journal of Physiology—Heart and Circulatory Physiology*, vol. 292, no. 3, pp. H1452–H1459, 2007.
- [6] K. Steding-Ehrenborg, M. Carlsson, S. Stephensen, and H. Arheden, "Atrial aspiration from pulmonary and caval veins is caused by ventricular contraction and secures 70% of the total stroke volume independent of resting heart rate and heart size," *Clinical Physiology and Functional Imaging*, vol. 33, no. 3, pp. 233–240, 2013.
- [7] H. Hu, H. Liu, Z. Gao, and L. Huang, "Hybrid segmentation of left ventricle in cardiac MRI using gaussian-mixture model and region restricted dynamic programming," *Magnetic Resonance Imaging*, vol. 31, no. 4, pp. 575–584, 2013.
- [8] N. C. F. Codella, M. D. Cham, R. Wong et al., "Rapid and accurate left ventricular chamber quantification using a novel CMR segmentation algorithm: a clinical validation study," *Journal of Magnetic Resonance Imaging*, vol. 31, no. 4, pp. 845–853, 2010.
- [9] E. Heiberg, J. Sjögren, M. Ugander, M. Carlsson, H. Engblom, and H. Arheden, "Design and validation of segment—freely available software for cardiovascular image analysis," *BMC Medical Imaging*, vol. 10, article 1, 2010.
- [10] E. Heiberg, L. Wigstrom, M. Carlsson, A. F. Bolger, and M. Karlsson, "Time resolved three-dimensional automated segmentation of the left ventricle," in *Proceedings of the Computers in Cardiology*, pp. 599–602, Lyon, France, September 2005.
- [11] L. R. Dice, "Measures of the amount of ecologic association between species," *Ecology*, vol. 26, no. 3, pp. 297–302, 1945.
- [12] D. Grosgeorge, C. Petitjean, J. Caudron, J. Fares, and J. N. Dacher, "Automatic cardiac ventricle segmentation in MR images: a validation study," *International Journal of Computer Assisted Radiology and Surgery*, vol. 6, no. 5, pp. 573–581, 2011.
- [13] Y. Huang, X. Zhou, B. Miao et al., "An image based system biology approach for Alzheimer's disease pathway analysis," in *Proceedings of the Life Science Systems and Applications Workshop (LiSSA '09)*, pp. 128–132, 2009.
- [14] A. Suinesiaputra, B. Cowan, J. P. Finn et al., "Left ventricular segmentation challenge from cardiac MRI: a collation study," in *Statistical Atlases and Computational Models of the Heart. Imaging and Modelling Challenges*, O. Camara, E. Konukoglu, M. Pop, K. Rhode, M. Sermesant, and A. Young, Eds., vol. 7085 of *Lecture Notes in Computer Science*, pp. 88–97, Springer, Berlin, Germany, 2012.
- [15] N. C. F. Codella, H. Y. Lee, D. S. Fieno et al., "Improved left ventricular mass quantification with partial voxel interpolation in vivo and necropsy validation of a novel cardiac MRI segmentation algorithm," *Circulation: Cardiovascular Imaging*, vol. 5, no. 1, pp. 137–146, 2012.
- [16] H. C. van Assen, M. G. Danilouchkine, A. F. Frangi et al., "SPASM: a 3D-ASM for segmentation of sparse and arbitrarily oriented cardiac MRI data," *Medical Image Analysis*, vol. 10, no. 2, pp. 286–303, 2006.
- [17] N. C. F. Codella, J. W. Weinsaft, M. D. Cham, M. Janik, M. R. Prince, and Y. Wang, "Left ventricle: automated segmentation by using myocardial effusion threshold reduction and intravoxel computation at MR imaging," *Radiology*, vol. 248, no. 3, pp. 1004–1012, 2008.
- [18] S. Plein, W. H. T. Smith, J. P. Ridgway et al., "Qualitative and quantitative analysis of regional left ventricular wall dynamics using real-time magnetic resonance imaging: comparison with conventional breath-hold gradient echo acquisition in volunteers and patients," *Journal of Magnetic Resonance Imaging*, vol. 14, no. 1, pp. 23–30, 2001.
- [19] R. J. van der Geest, B. P. F. Lelieveldt, E. Angelié et al., "Evaluation of a new method for automated detection of left ventricular boundaries in time series of magnetic resonance images using an active appearance motion model," *Journal of Cardiovascular Magnetic Resonance*, vol. 6, no. 3, pp. 609–617, 2004.
- [20] P. A. Cain, R. Ahl, E. Hedstrom et al., "Age and gender specific normal values of left ventricular mass, volume and function for gradient echo magnetic resonance imaging: a cross sectional study," *BMC Medical Imaging*, vol. 9, article 2, 2009.
- [21] H. Childs, L. Ma, M. Ma et al., "Comparison of long and short axis quantification of left ventricular volume parameters by cardiovascular magnetic resonance, with ex-vivo validation," *Journal of Cardiovascular Magnetic Resonance*, vol. 13, no. 1, article 40, 2011.

Research Article

Development of an *Ex Vivo*, Beating Heart Model for CT Myocardial Perfusion

Gert Jan Pelgrim,¹ Marco Das,² Ulrike Haberland,³ Cees Slump,⁴
Astri Handayani,¹ Sjoerd van Tuijl,⁵ Marco Stijnen,⁵ Ernst Klotz,³ Matthijs Oudkerk,⁶
Joachim E. Wildberger,² and Rozemarijn Vliegenthart¹

¹University of Groningen, University Medical Center Groningen, Center for Medical Imaging-North East Netherlands, Department of Radiology, Hanzeplein 1, 9713 GZ Groningen, Netherlands

²Department of Radiology and Cardiovascular Research Institute Maastricht (CARIM), Maastricht University Medical Center, Postbus 5800, 6202 AZ Maastricht, Netherlands

³Siemens AG Healthcare, Forchheim, Germany

⁴University of Twente, Drienerlolaan 5, 7522 NB Enschede, Netherlands

⁵LifeTec Group BV, Den Dolech 2, 5612 AZ Eindhoven, Netherlands

⁶University of Groningen, University Medical Center Groningen, Center for Medical Imaging-North East Netherlands, Hanzeplein 1, 9713 GZ Groningen, Netherlands

Correspondence should be addressed to Rozemarijn Vliegenthart; r.vliegenthart@umcg.nl

Received 11 September 2014; Accepted 23 December 2014

Academic Editor: Marco Francone

Copyright © 2015 Gert Jan Pelgrim et al. This is an open access article distributed under the Creative Commons Attribution License, which permits unrestricted use, distribution, and reproduction in any medium, provided the original work is properly cited.

Objective. To test the feasibility of a CT-compatible, *ex vivo*, perfused porcine heart model for myocardial perfusion CT imaging. **Methods.** One porcine heart was perfused according to Langendorff. Dynamic perfusion scanning was performed with a second-generation dual source CT scanner. Circulatory parameters like blood flow, aortic pressure, and heart rate were monitored throughout the experiment. Stenosis was induced in the circumflex artery, controlled by a fractional flow reserve (FFR) pressure wire. CT-derived myocardial perfusion parameters were analysed at FFR of 1 to 0.10/0.0. **Results.** CT images did not show major artefacts due to interference of the model setup. The pacemaker-induced heart rhythm was generally stable at 70 beats per minute. During most of the experiment, blood flow was 0.9–1.0 L/min, and arterial pressure varied between 80 and 95 mm/Hg. Blood flow decreased and arterial pressure increased by approximately 10% after inducing a stenosis with $FFR \leq 0.50$. Dynamic perfusion scanning was possible across the range of stenosis grades. Perfusion parameters of circumflex-perfused myocardial segments were affected at increasing stenosis grades. **Conclusion.** An adapted Langendorff porcine heart model is feasible in a CT environment. This model provides control over physiological parameters and may allow in-depth validation of quantitative CT perfusion techniques.

1. Introduction

Computed tomography (CT) has become the premier non-invasive imaging modality for the noninvasive evaluation of the coronary arteries. For the functional assessment of coronary artery disease (CAD), the sole diagnosis of coronary luminal narrowing is often limited, especially in case of 30–70 percent (intermediate) grade stenosis [1]. Usually, additional testing on the impact of stenosis on myocardial perfusion is needed. To date, CT is not commonly used in daily clinical practice worldwide, except for several leading clinics in CT

imaging. However, recent evidence suggests that state-of-the-art CT scanners allow evaluation of myocardial blood supply, on top of the interrogation of coronary morphology [2]. This includes quantification of myocardial perfusion using dynamic perfusion techniques in second-generation dual source CT (DSCT) scanning [3, 4]. Measurement of absolute myocardial perfusion can enhance the diagnostic accuracy for hemodynamically significant CAD, compared to visual analysis of perfusion maps [4–6]. At present, only positron emission tomography (PET) imaging is capable of true perfusion quantification [7]. Morton et al. recently demonstrated

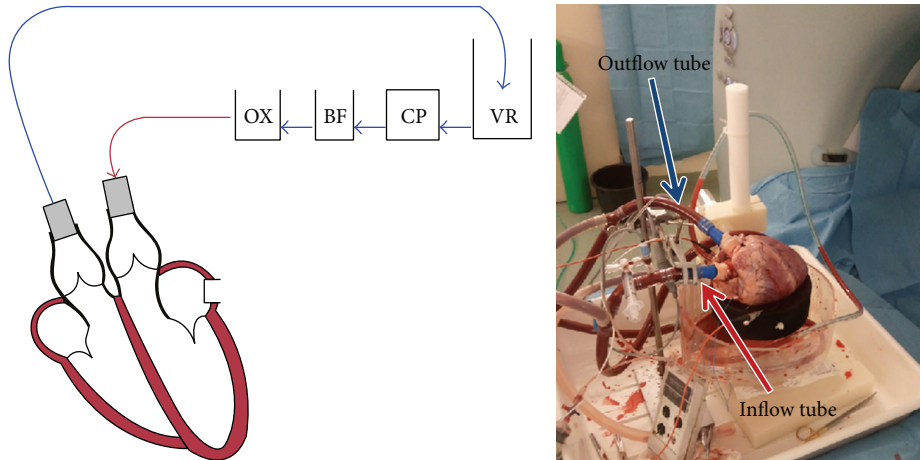


FIGURE 1: From the venous reservoir (VR), the blood first passed the cardiac pump CP. Then, the blood was pumped through the blood filter (BF) into the oxygenator (OX) and, from there, through the aorta into the coronary arteries. The setup was placed on the scanner table; all parts which could possibly interfere with the signal were placed outside the field of view.

potential for CMR to derive semiquantitative parameters of perfusion [8].

Before quantitative CT perfusion imaging can be implemented in clinical practice, systematic validation is mandatory. Therefore, an *ex vivo* model of a perfused, isolated heart of a slaughterhouse pig was used for this systematic analysis.

The aim of this study was to develop an explanted, perfused porcine heart model in a CT environment. We hypothesized that this model allows for standardized validation of CT perfusion parameters.

2. Materials and Methods

2.1. Heart Acquisition and Preparation. In this experiment, one *ex vivo* porcine heart model was used. The current study was designed to purely show the feasibility of the model. The heart was obtained from a pig, slaughtered for human consumption. Protocols at the slaughterhouse and laboratory were in accordance with EC regulations 1069/2009 regarding the use of slaughterhouse animal material for diagnosis and research, supervised by the Dutch Government (Dutch Ministry of Agriculture, Nature and Food Quality) and approved by the associated legal authorities of animal welfare (Food and Consumer Product Safety Authority).

A Dutch Landrace hybrid pig of approximately 110 kg live weight was used. After exsanguination, the thorax was opened by a parasternal incision. The pulmonary artery was cut just before the bifurcation. The aorta was cut before the supra-aortic vessels. The heart was immediately cooled topologically in ice slurry. To arrest the heart, the aorta was cannulated to administer 2 L of cold cardioplegic solution (4°C Custodiol histidine-tryptophan-ketoglutarate (HTK), Essential Pharmaceuticals, Pennsylvania, USA) to the coronary arteries at a pressure of 60 mmHg. The ischemic time at body temperature did not exceed 5 minutes. From subsequently slaughtered pigs, 20 L of fresh blood was collected for reperfusion. The heart and blood (heparinized with 5000 IU/L) were stored cold during transportation. Preparations of the heart

were executed in the laboratory under cold and cardioplegic conditions until resuscitation. First, the pericardial sack was discarded. The azygos vein and the inferior and superior caval vein were ligated. A cannula was inserted into the aorta and fixed approximately 40 mm distal to the valve annulus. The pulmonary veins were cut at the left atrium and ligated. A perforated drain cannula was inserted into the left atrium and ventricle allowing sufficient venting after resuscitation. Similarly, a cannula was inserted into the pulmonary artery. Around the proximal circumflex (Cx) coronary artery, an inflatable cuff was placed, providing the possibility of mimicking stenosis under controlled circumstances. By measuring pressure distal to the stenosis and calculating the ratio between this pressure and the aortic pressure, the fractional flow reserve (FFR) was determined, a measure for the hemodynamic severity of the stenosis. In clinical practice, FFR measurements are performed under maximal hyperaemic conditions, using adenosine or dipyridamole. The heart in this experiment was already in maximal hyperaemic state, because of its removal from the pig body [9]. The Cx artery was chosen because it is easily accessible (in contrast to the right coronary artery) and perfuses an identifiable, but not too large, part of the left ventricle (in contrast to the left anterior descending artery). During the experiment, FFR measurements were used to verify the cuff-induced stenosis grade. CT perfusion scanning was first performed without stenosis, followed by scanning at FFR values of 0.7, 0.5, 0.3, and 0.1/0.0. Scanning was repeated three times at each FFR. A deviation of 0.05 from the goal FFR was considered acceptable. To prevent the contrast agent from building up in the circulating blood pool and thus causing differential baseline enhancement, the blood pool was refreshed with new blood after each stenosis grade situation.

2.2. Heart Perfusion. After preparation, the aorta and pulmonary artery were connected to the circulation loop using the cannulas (Figure 1). A bed of flexible cloth provided epicardial suspension. The heart was aligned in the scanner

in supine position. A modified Langendorff perfusion model was used, with an artificial heart-lung loop. In 1895, Langendorff et al. proposed a model of retrograde perfusion of mammalian hearts in which a Krebs-Henseleit solution circulated via the aorta [10, 11]. This Langendorff model was refined by circulation of whole blood [12]. Whole blood was pumped by a centrifugal pump (BioMedicus, Medtronic, Minneapolis, MN, USA) from a venous reservoir into the aorta towards the aortic sinus and the coronary arteries. The flow in the coronaries is pulsatile and pressure dependent. A pressure is present at the aortic root, causing the flow of blood into the coronaries. When the myocardium contracts during systole, the coronary vasculature is compressed and therefore the vascular resistance increases, resulting in reduced coronary flow. During diastole the myocardium relaxes, which opens the vascular bed and thereby lowers vascular resistance with higher coronary flow as a result. In a normally functioning heart, the aortic blood pressure pulse varies in pressure between 120 and 80 mmHg, resulting in a pressure pulse of 40 mmHg. However, in the Langendorff experiments the pressure pulse is only in the order of magnitude of 10 mmHg.

The coronary venous blood returned to the venous reservoir via the coronary sinus, right atrium, right ventricle, and pulmonary artery. The reperfusion medium circulated through a filter (AFFINITY Arterial 38 μ m blood filter; Medtronic, Minneapolis, Minnesota, USA) and an oxygenator-heat exchanger (AFFINITY NT Oxygenator; Medtronic, Minneapolis, Minnesota, USA). The blood was oxygenated with 20% O₂, 75% N₂, and 5% CO₂ carbogen gas. Blood glucose level was maintained between 5 and 7 mmol/L by addition of glucose-insulin mixture. The temperature of the circulating blood was 38°C. The blood flow through the coronary arteries was approximately 1.5 mL/g per minute and controlled with the centrifugal pump. The mean coronary flow was measured with an ultrasound flow probe (LifeTec Group, Eindhoven, Netherlands) at the pump, and the pressure was measured at the aortic root with a pressure sensor (PI0EZ-1; Becton Dickinson Medical, Franklin Lakes, New Jersey, USA).

When reperfusion of the coronary system was started, total ischemic time was approximately 4 hours. After coronary perfusion was reinstated, the heart showed spontaneous contractions while warming up by the circulating whole blood and gradually regained sinus rhythm. Some defibrillations were performed, of 10–30 Joules, to restore sinus rhythm. The heart was kept in this condition for at least 15 minutes, to allow stabilisation at the membranous level. If the heart rhythm did not stabilize, or if rhythm became irregular during the experiment, a Medtronic external pacemaker model 5375 (Medtronic, Minneapolis, Minnesota, USA) was used to induce a stable heart rate at approximately 70 beats per minute (see movie in Supplementary Material available online at <http://dx.doi.org/10.1155/2015/412716>). After obtaining a stable heart rate, the imaging protocols were started. ECG clips were placed on the “wet” flexible cloth and connected to the scanner ECG leads to feed signal to the scanner and allow ECG-synchronized image acquisition. During the entire experiment, the heart rate, pacing status (heart paced yes or no), aortic pressure, and blood flow were monitored.

This enabled analysis of model stability and influence of luminal narrowing on the model.

2.3. CT Imaging Protocol. CT acquisitions were performed on a second-generation DSCT scanner (SOMATOM Definition Flash, Siemens Healthcare, Forchheim, Germany). Scans were acquired in caudocranial direction. At each stenosis grade, the protocol consisted of a noncontrast enhanced CT scan, three dynamic CT perfusion (CTP) acquisitions, and one coronary CT angiography (CTA) scan. First, scout images were obtained to determine the area of interest and a non-contrast enhanced CT scan was performed to determine baseline enhancement of the heart and blood pool. The unenhanced scan was made at tube voltage of 100 kV and tube current of 100 mAs. Next, perfusion series were performed at 5-minute intervals, to allow mixing of contrast agent in the blood pool and thus minimize the influence of contrast buildup. Dynamic perfusion image acquisitions were performed during end-systole (300 ms delay after the R-wave) in shuttle mode, with ECG-triggering. Given a detector width of 38.4 mm and an overlap of 10%, the anatomical coverage was 7.3 cm [13]. The scan area was determined based on the scout scan. The entire left ventricle of the heart was selected as image field of view (FOV), from the aortic root to the apex. The heart was placed parallel to the z-axis of the table. Matrix size was 512 \times 512. Due to a heart frequency of >70 per minute, images were acquired every second heartbeat. Image acquisition parameters were 2 \times 2 \times 64 detector rows, 3.0 mm collimation, 2 \times 100 kV tube voltage, and 350 mAs per rotation with a rotation time of 285 ms. The CM concentration was 300 mg iodine/mL (Ultravist 300, Bayer, Berlin, Germany), which was diluted to a mixture of 40 percent contrast and 60 percent saline for the injections. CM was injected into the blood stream 200 cm from the coronary arteries, allowing mixing of the perfusate and the CM but preserving the bolus shape of the injection. A CM volume of 15 mL, with a contrast to saline ratio of 40/60, was used at an injection rate of 3 mL/sec. Imaging was started 5 seconds prior to start of CM injection, with a total scan time of 35 seconds. After the perfusion series, coronary CTA scanning was performed. First, scan timing was determined by administering additional 10 mL of diluted (40/60 contrast/saline ratio) iodine contrast. Image acquisition was initiated 3 seconds after peak enhancement in the aortic root. Then, CTA was performed with another 15 mL of diluted contrast at an injection rate of 3 mL/sec. Coronary CTA data were acquired with retrospective ECG-gating, to analyse best-systolic and best-diastolic phase reconstructions. Scan parameters were 2 \times 2 \times 64 detectors rows, 0.6 mm detector collimation, 2 \times 100 kV, 350 mAs per rotation, and 285 ms gantry rotation time. CTA data were acquired to analyse the stenosis severity related to the FFR measurements.

2.4. Image Reconstruction. Coronary CTA datasets were reconstructed with 0.75 mm slice thickness, 0.3 mm increment, and I26F (iterative) reconstruction kernel to reduce image noise. Coronary evaluation was performed in Syngo.via, based on curved multiplanar reformat series. The degree of luminal narrowing of the different stenosis grades

TABLE 1: Arterial blood flow (L/min) and blood pressure (mm/Hg) in 5 different stenosis grades.

	Normal perfusion	FFR 0.70	FFR 0.50	FFR 0.30	Total occlusion
Arterial blood flow (SD)	1.0 L/min (constant)	1.0 L/min (constant)	1.0 L/min (constant)	0.93 L/min (SD 0.05)	0.90 L/min (constant)
Arterial blood pressure (SD)	82.7 mm/Hg (SD 0.6)	80.7 mm/Hg (SD 1.2)	86.7 mm/Hg (SD 1.2)	88.7 mm/Hg (SD 1.5)	94 mm/Hg (SD 2.7)

SD: standard deviation.

was assessed by measuring the remaining luminal area on cross-sections. Mean diameter and area of the induced stenosis were compared to the FFR measurement to provide information on the severity of luminal narrowing. For myocardial evaluation, CT perfusion datasets were reconstructed in short-axis images with 3.0 mm slice thickness, 1.5 mm increment, and B23f (filtered back) reconstruction kernel for quantitative myocardial assessment, including an iodine beam hardening correction algorithm. Perfusion datasets were analysed using commercially available software, volume perfusion CT (VPCT) myocardium (VA41A, Siemens Healthcare, Forchheim, Germany). The AHA segmental model was used to label the segments of the heart [14]. The flow territory of the Cx was determined based on the total occlusion scan. Segments in the Cx territory were defined as Cx segments, others as non-Cx segments. Perfusion parameters for Cx myocardial segments and non-Cx segments were calculated. The FOV included the short-axis view of the heart. The inflow tube of the perfusate to the heart was looped through the FOV to allow calculation of an input function as reference for the perfusion of individual myocardial segments. The VPCT software uses the input function and the enhancement in the segments of the heart to calculate myocardial blood flow and blood volume in mL/100 mL/min and mL/100 mL, respectively, 100 mL being a measure for the volume of the myocardial tissue.

2.5. Statistical Analysis. Data management and statistical analysis were performed using Excel and SPSS 19 (IBM Corp, Armonk, NY). Independent variance tests were carried out to analyse whether the Cx and non-Cx segment groups showed normal distribution of perfusion measurements. Thereafter, the Mann-Whitney U test for equality was performed. Median values of myocardial blood flow and volume were compared between segments with normal perfusion and segments with induced stenosis at different stenosis grades.

3. Results

The pacemaker-induced heart rhythm was stable at approximately 70 beats per minute (supplementary movie). Arterial blood flow and blood pressure were kept constant as much as possible at 1 L/min and 80 mm/Hg, respectively. Blood flow was 1.0 L/min at FFR values of 1.0, 0.7, and 0.5 and slightly lower, 0.9 L/min, at FFRs of 0.3 and 0.1/0.0 (Table 1). Mean arterial pressure gradually increased from 80 to 95 mm/Hg over the course of the experiment. Stenosis induction with FFR pressures of 0.3 and 0.0 caused the arterial pressure to increase with 10 mm/Hg and blood flow to decrease with

TABLE 2: Diameter of stenosis divided by the artery diameter before stenosis, and the area stenosis divided by the area before stenosis, for the FFR-based stenosis grades.

	FFR 0.70	FFR 0.50	FFR 0.30
Mean diameter on CTA	74%	47%	31%
Area stenosis on CTA	49%	22%	12%

0.1 L/min. The FFR measurements at each stenosis grade were stable. Occasionally, the pressure of the inflatable cuff lowered, recognisable as a rise in the FFR value. Then, the cuff was inflated again to maintain FFR within the 0.05 boundary from the goal stenosis grade. CTA measurements of the stenosis diameter and stenosis area are shown in Table 2. A 0.70 FFR-based stenosis corresponded with a 50 percent area stenosis on CTA.

Image quality of the coronary CTA scans was high, with HU values of over 325 in the coronary arteries (Figure 2). In the dynamic scans, the heart could be imaged in total (Figure 3). Based on the total occlusion scan, the flow territory of the Cx was found to be limited to segment 5 (Figures 2 and 4). The relatively limited extent of ischemia was due to a small size Cx artery in this porcine heart.

At every stenosis grade, three scans with one stenotic Cx segment and 15 normally perfused segments were analysed, a total of 48 segments per stenosis grade. In Table 3 the median values of myocardial blood flow and blood volume are shown for Cx- and non-Cx-perfused segments. Myocardial blood flow and volume for the Cx segment were lower at stenosis grades with FFR of ≤ 0.50 compared to non-Cx segments.

4. Discussion

This study shows the feasibility of myocardial perfusion analysis in a Langendorff pig heart model in a CT environment. This experimental setup enables detailed and systematic study of myocardial perfusion under standardized conditions and at differing degrees of blood flow, allowing for qualitative and quantitative evaluation of myocardial perfusion. Preliminary results suggest that newly developed CT perfusion imaging techniques can be validated with this model under controlled conditions, with hemodynamic settings relatively similar to the *in vivo*, clinical situation.

The Langendorff model is a retrograde perfusion model established in 1895 [11]. In 2007, Skrzypiec-Spring et al. reviewed the use of this model throughout a century of existence and concluded that it can be used to study ischaemia,

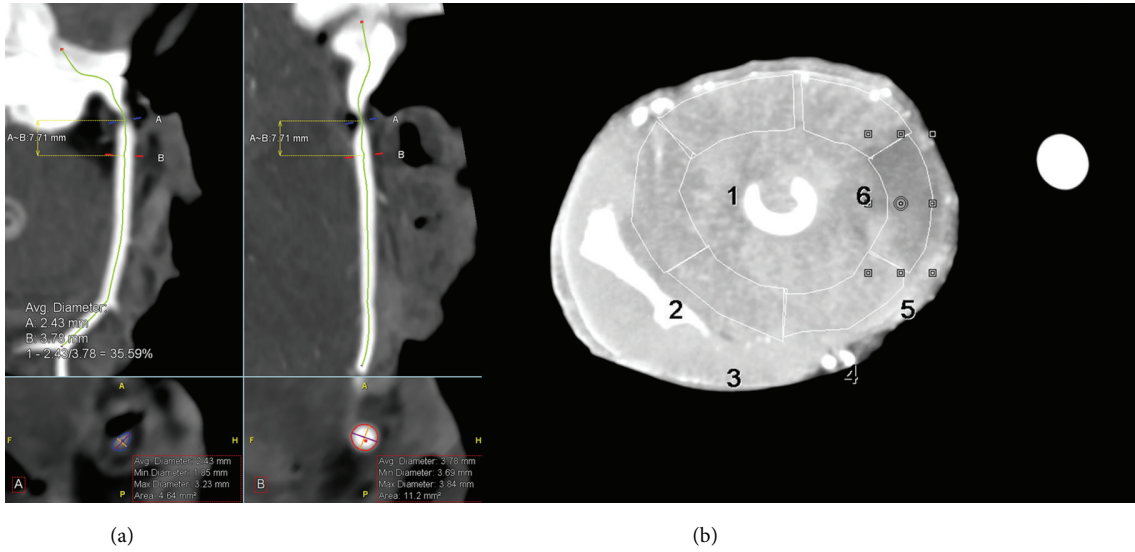


FIGURE 2: Example of images of the Cx artery with an FFR of 0.30. (a) The computed tomography angiography (CTA) image in curved multiplanar reformat shows the luminal narrowing. (b) The resulting perfusion defect in segment 5 as visible on maximum intensity projection (MIP) image.

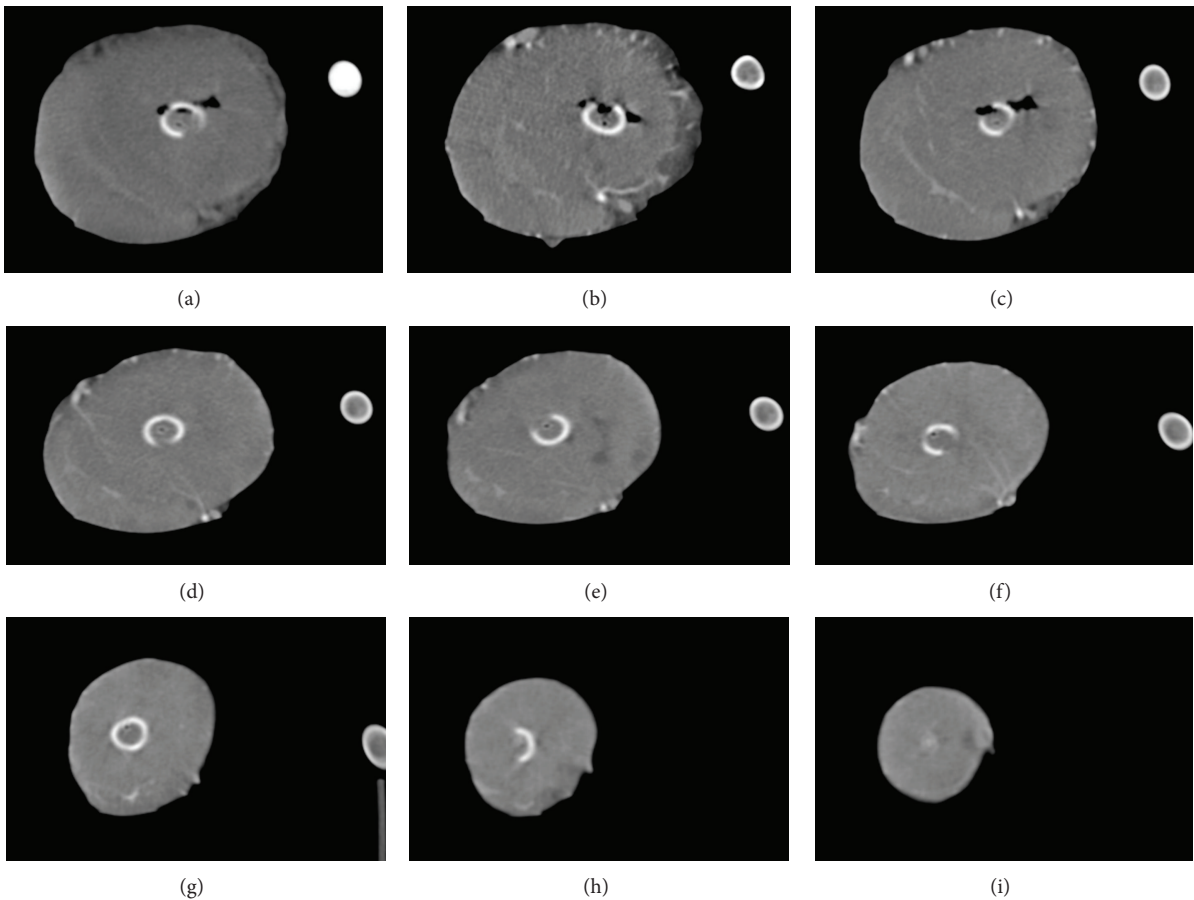


FIGURE 3: Image (a) shows the inflow of CM bolus through the inflow tube. Images (b)–(i) show the contrast inflow in the myocardium at short-axis cross-sections from basal to apical.

TABLE 3: Median blood flow (L/min) in normal and defected segments for multiple stenosis grades.

	No stenosis	FFR 0.70	FFR 0.50	FFR 0.30	Total occlusion
Calculated normal segments (min–max)	151 mL/100 mL/min (113–205)	173 mL/100 mL/min (122–260)	162 mL/100 mL/min (133–247)	124 mL/100 mL/min (70–207)	108 mL/100 mL/min (43–167)
Calculated defect segments (min–max)	133 mL/100 mL/min (127–139)	157 mL/100 mL/min (129–183)	121 mL/100 mL/min (96–125)	74 mL/100 mL/min (66–78)	34 mL/100 mL/min (34–39)

Minimum and maximum blood flow for each group are shown in brackets.

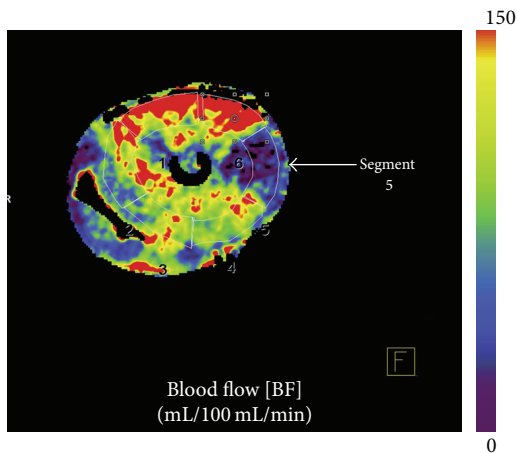


FIGURE 4: Blood flow map of the porcine heart at complete Cx occlusion: red color meaning higher/normal flow and blue indicating reduced flow.

stunning, hibernation, and arrhythmias and for drug testing [10]. In several studies the Langendorff model has been used to investigate, for instance, cardiac physiology and donor heart preservation methods [15, 16]. In our study, arterial blood flow and pressure were stable and controllable during most of our experiment. Part of the controllable circumstances included the confirmation of the stenosis degree by FFR assessment. The decrease in blood flow and increase in blood pressure during the experiment can be explained by the increase in peripheral resistance due to the induced stenosis. Because the heart was explanted, it was already in stress state and no compensatory mechanisms were present [9]. Thus, induction of a stenosis directly influenced coronary blood flow and pressure. A stenosis with a 0.7 pressure drop, however, did not influence blood flow and blood pressure in this single experiment. We hypothesize that the lumen area may still be too large for peripheral resistance to increase, and, therefore, blood flow and arterial pressure will not be influenced.

Schuster et al. showed potential for the Langendorff model for perfusion analysis in MRI environment [17]. They showed consistent blood flow and pressure over time for hearts without stenosis. However, they did not evaluate the effect of increasing coronary stenosis on model stability (RCA in one heart was occluded but only to compare first pass perfusion area to infarct size).

Small clinical studies have shown that adenosine stress dynamic perfusion CT testing can detect hemodynamically

significant stenosis [3, 4, 18–20]. Quantitative evaluation of myocardial perfusion may have incremental value to detect flow-limiting stenosis compared to visual analysis. Prior to clinical implementation, the relationship between CT-derived perfusion parameters across the range of coronary stenosis needs validation against reference standards. Ethically, it is difficult to justify comparison of two modalities with associated radiation dose in patients. Also, there is little control over hemodynamic parameters in a human model especially regarding degree of stenosis. Conversely, a phantom model only allows limited conclusions with regard to the *in vivo* situation. An animal model mimicking human cardiac circulation may be of great help. Pigs have been researched extensively in cardiac imaging, since the porcine model provides excellent comparison to the human heart in size and physiology [21–24]. The porcine heart is especially well suited for myocardial perfusion imaging studies, because it cannot develop collateral flow. Thus, there is a direct relationship between stenosis grade and the decrease in downstream perfusion.

In *in vivo* porcine experiments CT allowed quantification of coronary flow [5, 22–25]. The advantage of *in vivo* experiments is that the physiology and cardiac function is intact providing cardiac features comparable to human studies. However, *in vivo* experiments are often more complex than single-heart experiments, because whole pigs cannot as easily and directly be manipulated as explanted hearts. Physiologically, the explanted heart is not as complex as the heart in living animals, offering more control and possibly better reproducibility. An extension of the present experiment could lie in imaging the porcine heart with different modalities to directly compare perfusion techniques at different stenosis grades.

Summarizing, our model has several benefits compared to other experimental models. A major advantage of the Langendorff model is the control of myocardial blood flow. A stenosis can be directly induced, and its severity can easily be altered. Because the heart is disconnected from the body, it is free of neural/hormonal influences. The heart is already in stress state, because of the prior explantation. Thus, the coronary arteries are at maximum dilation, mimicking the situation of adenosine stress perfusion imaging. Furthermore, after otherwise fatal events such as arrhythmias and infarction-induced cardiac arrest, introducing a pacemaker or reinstating sinus rhythm with defibrillations of 10–30 J can prolong the experiment. Compared to scanning and subsequent sacrificing of living pigs, a model using slaughterhouse pigs provides an alternative where no additional animals are sacrificed.

Our model also has some disadvantages. Due to the fact that physiological processes were no longer intact, the model is less comparable to the clinical situation. The setup platform and fixation as well as contrast protocol and left ventricular pressure are not like *in vivo* situations. The setup was mostly made of plastic, because metal would induce large artifacts. Furthermore, the heart experienced an ischaemic period directly after removal, which may alter its condition and influence perfusion. During the experiment, some difficulties in ECG-triggering were experienced. This could be due to the usage of the pacemaker. The signal transduction of the pacemaker spike within the heart can differ between beats, possibly resulting in phase irregularities. Even so, signal transduction during the experiment was generally good, with good image quality and limited motion artifacts. Pacemaker-induced rhythm is generally stable; however premature ventricular contractions may occur. Another possible bias is the fixed pacemaker-induced heart rate in this heart. Previous studies in humans have shown an increase in heart rate when stressed using adenosine [18, 19]. This increase is not simulated in this particular pig heart experiment. Therefore, our Langendorff experiment could be less prone to heart rate dependent artefacts compared to human studies when heart rates are higher. The stenosis induced in the Cx artery did not cause a large perfusion defect, because of a rudimentary Cx artery. There is a natural distribution in the size and perfusion areas of the coronary arteries in pigs, comparable to humans. We intend to repeat this experiment in a number of pig hearts to gain more information on variability of the model. Compared to an entire pig, the current model is relatively expensive. A last limitation is that the study was performed in one pig heart, only. The current study was designed to purely show the feasibility of the model. The model should be repeated in a larger number of explanted hearts to confirm stability of the setup and to optimize the experimental protocol.

5. Conclusion

This study demonstrates the feasibility of *ex vivo* myocardial perfusion imaging and quantification in a CT environment at different grades of coronary stenosis. The Langendorff model provides control over physiological parameters such as blood flow and stenosis grade. The described model shows promise for validation of CT perfusion imaging techniques under controlled circumstances.

Abbreviations

CAD: Coronary artery disease
 CM: Contrast media
 CT: Computed tomography
 CTA: Computed tomography angiography
 CTP: Computed tomography perfusion
 Cx: Circumflex artery
 FOV: Field of view
 FFR: Fractional flow reserve
 MRI: Magnetic resonance imaging
 DSCT: Dual source computed tomography
 PET: Positron emission tomography

RCA: Right coronary artery
 VPCT: Volume perfusion CT.

Conflict of Interests

Ulrike Haberland and Ernst Klotz are employees of the CT Division of Siemens Healthcare Sector (Forchheim, Germany) which manufactured the CT equipment used in this study. Sjoerd van Tuijl and Marco Stijnen are employees of LifeTec Group (Eindhoven, Netherlands) which provided the Langendorff porcine heart setup as well as the porcine heart itself.

Acknowledgment

Rozemarijn Vliegthart is supported by a grant from the Netherlands Organisation for Scientific Research.

References

- [1] J. D. Schuijff, W. Wijns, J. W. Jukema et al., "A comparative regional analysis of coronary atherosclerosis and calcium score on multislice CT versus myocardial perfusion on SPECT," *Journal of Nuclear Medicine*, vol. 47, no. 11, pp. 1749–1755, 2006.
- [2] A. Rossi, D. Merkus, E. Klotz, N. Mollet, P. J. de Feyter, and G. P. Krestin, "Stress myocardial perfusion: imaging with multidetector CT," *Radiology*, vol. 270, no. 1, pp. 25–46, 2014.
- [3] Y. Wang, L. Qin, X. Shi et al., "Adenosine-stress dynamic myocardial perfusion imaging with second-generation dual-source CT: comparison with conventional catheter coronary angiography and SPECT nuclear myocardial perfusion imaging," *American Journal of Roentgenology*, vol. 198, no. 3, pp. 521–529, 2012.
- [4] F. Bamberg, A. Becker, F. Schwarz et al., "Detection of hemodynamically significant coronary artery stenosis: incremental diagnostic value of dynamic CT-based myocardial perfusion imaging," *Radiology*, vol. 260, no. 3, pp. 689–698, 2011.
- [5] A. H. Mahnken, E. Klotz, H. Pietsch et al., "Quantitative whole heart stress perfusion CT imaging as noninvasive assessment of hemodynamics in coronary artery stenosis: preliminary animal experience," *Investigative Radiology*, vol. 45, no. 6, pp. 298–305, 2010.
- [6] A. M. Huber, V. Leber, B. M. Gramer et al., "Myocardium: dynamic versus single-shot CT perfusion imaging," *Radiology*, vol. 269, no. 2, pp. 378–386, 2013.
- [7] P. A. Kaufmann and P. G. Camici, "Myocardial blood flow measurement by PET: technical aspects and clinical applications," *Journal of Nuclear Medicine*, vol. 46, no. 1, pp. 75–88, 2005.
- [8] G. Morton, A. Chiribiri, M. Ishida et al., "Quantification of absolute myocardial perfusion in patients with coronary artery disease: comparison between cardiovascular magnetic resonance and positron emission tomography," *Journal of the American College of Cardiology*, vol. 60, no. 16, pp. 1546–1555, 2012.
- [9] S. Schampaert, M. van 't Veer, M. C. M. Rutten et al., "Autoregulation of coronary blood flow in the isolated beating pig heart," *Artificial Organs*, vol. 37, no. 8, pp. 724–730, 2013.
- [10] M. Skrzypiec-Spring, B. Grothaus, A. Szlag, and R. Schulz, "Isolated heart perfusion according to Langendorff—still viable in the new millennium," *Journal of Pharmacological and Toxicological Methods*, vol. 55, no. 2, pp. 113–126, 2007.

- [11] O. Langendorff, "Untersuchungen am überlebenden Säugethi-erherzen," *Pflüger, Archiv für die Gesammte Physiologie des Menschen und der Thiere*, vol. 61, no. 6, pp. 291–332, 1895.
- [12] D. Modersohn, S. Eddicks, C. Grosse-Siestrup, I. Ast, S. Holinski, and W. Konertz, "Isolated hemoperfused heart model of slaughterhouse pigs," *International Journal of Artificial Organs*, vol. 24, no. 4, pp. 215–221, 2001.
- [13] F. Bamberg, E. Klotz, T. Flohr et al., "Dynamic myocardial stress perfusion imaging using fast dual-source CT with alternating table positions: initial experience," *European Radiology*, vol. 20, no. 5, pp. 1168–1173, 2010.
- [14] M. D. Cerqueira, N. J. Weissman, V. Dilsizian et al., "Standardized myocardial segmentation and nomenclature for tomographic imaging of the heart. A statement for healthcare professionals from the Cardiac Imaging Committee of the Council on Clinical Cardiology of the American Heart Association," *Circulation*, vol. 105, no. 4, pp. 539–542, 2002.
- [15] W. F. Fearon, L. B. Balsam, H. M. O. Farouque et al., "Novel index for invasively assessing the coronary microcirculation," *Circulation*, vol. 107, no. 25, pp. 3129–3132, 2003.
- [16] H. Aupperle, J. Garbade, C. Ullmann et al., "Comparing the ultrastructural effects of two different cardiac preparation- and perfusion-techniques in a porcine model of extracorporeal long-term preservation," *European Journal of Cardio-Thoracic Surgery*, vol. 31, no. 2, pp. 214–221, 2007.
- [17] A. Schuster, I. Grünwald, A. Chiribiri et al., "An isolated perfused pig heart model for the development, validation and translation of novel cardiovascular magnetic resonance techniques," *Journal of Cardiovascular Magnetic Resonance*, vol. 12, article 53, 2010.
- [18] G. Bastarrika, L. Ramos-Duran, M. A. Rosenblum, D. K. Kang, G. W. Rowe, and U. J. Schoepf, "Adenosine-stress dynamic myocardial CT perfusion imaging: initial clinical experience," *Investigative Radiology*, vol. 45, no. 6, pp. 306–313, 2010.
- [19] K. T. Ho, K. C. Chua, E. Klotz, and C. Panknin, "Stress and rest dynamic myocardial perfusion imaging by evaluation of complete time-attenuation curves with dual-source CT," *JACC: Cardiovascular Imaging*, vol. 3, no. 8, pp. 811–820, 2010.
- [20] M. Weininger, U. J. Schoepf, A. Ramachandra et al., "Adenosine-stress dynamic real-time myocardial perfusion CT and adenosine-stress first-pass dual-energy myocardial perfusion CT for the assessment of acute chest pain: initial results," *European Journal of Radiology*, vol. 81, no. 12, pp. 3703–3710, 2012.
- [21] D. J. Hearse and F. J. Sutherland, "Experimental models for the study of cardiovascular function and disease," *Pharmacological Research*, vol. 41, no. 6, pp. 597–603, 2000.
- [22] A. Rossi, A. Uitterdijk, M. Dijkshoorn et al., "Quantification of myocardial blood flow by adenosine-stress CT perfusion imaging in pigs during various degrees of stenosis correlates well with coronary artery blood flow and fractional flow reserve," *European Heart Journal Cardiovascular Imaging*, vol. 14, no. 4, pp. 331–338, 2013.
- [23] F. Schwarz, R. Hinkel, E. Baloch et al., "Myocardial CT perfusion imaging in a large animal model: comparison of dynamic versus single-phase acquisitions," *JACC: Cardiovascular Imaging*, vol. 6, no. 12, pp. 1229–1238, 2013.
- [24] A. So, J. Hsieh, J. Y. Li, J. Hadway, H. F. Kong, and T. Y. Lee, "Quantitative myocardial perfusion measurement using CT Perfusion: a validation study in a porcine model of reperfused acute myocardial infarction," *International Journal of Cardiovascular Imaging*, vol. 28, no. 5, pp. 1237–1248, 2012.
- [25] F. Bamberg, R. Hinkel, F. Schwarz et al., "Accuracy of dynamic computed tomography adenosine stress myocardial perfusion imaging in estimating myocardial blood flow at various degrees of coronary artery stenosis using a porcine animal model," *Investigative Radiology*, vol. 47, no. 1, pp. 71–77, 2012.

Research Article

Importance of Reference Muscle Selection in Quantitative Signal Intensity Analysis of T2-Weighted Images of Myocardial Edema Using a T2 Ratio Method

Iacopo Carbone,^{1,2,3} Helene Childs,⁴ Ahmed Aljizeeri,⁵
Naeem Merchant,^{3,6} and Matthias G. Friedrich^{1,3}

¹CMR Centre, Montreal Heart Institute, University of Montreal, Montreal, QC, Canada HIT 1C8

²Department of Radiological, Onchological and Pathological Sciences, Sapienza, University of Rome, 00161 Rome, Italy

³Stephenson CMR Centre, Libin Cardiovascular Institute of Alberta, University of Calgary, Calgary, AB, Canada T2N 2T9

⁴Western College of Veterinary Medicine, University of Saskatchewan, Saskatoon, SK, Canada S7N 5B4

⁵King Abdulaziz Cardiac Center, Riyadh 11426, Saudi Arabia

⁶Department of Diagnostic Imaging, Libin Cardiovascular Institute of Alberta, University of Calgary, Calgary, AB, Canada T2N 2T9

Correspondence should be addressed to Iacopo Carbone; iacopo.carbone@uniroma1.it

Received 7 August 2014; Revised 2 February 2015; Accepted 11 March 2015

Academic Editor: Volker Rasche

Copyright © 2015 Iacopo Carbone et al. This is an open access article distributed under the Creative Commons Attribution License, which permits unrestricted use, distribution, and reproduction in any medium, provided the original work is properly cited.

Objectives. The purpose of our study was to identify the suitability of various skeletal muscles as reference regions for calculating the T2 SI ratio for a semiautomated quantification of the extent of myocardial edema with T2-weighted images. **Methods.** Thirty-four patients with acute myocardial infarction (MI) were enrolled. The extent of myocardial edema was determined by T2 SI ratio map, using 4 different muscles as reference: major and minor pectoralis, serratus anterior, teres minor-infraspinatus, and subscapularis. The size of myocardial edema as visually quantified was used as the standard of truth. The control group consisted of 15 patients with chronic MI. Intra- and interobserver variability were assessed. **Results.** Due to poor image quality four patients were excluded from the analysis. In acute MI patients, serratus anterior muscle showed the strongest correlation with the visual analysis ($r = 0.799$; $P < 0.001$) and low inter- and intraobserver variability, while the other muscles resulted in a significant interobserver variability. In contrast, the use of other muscles as a reference led to overestimating edema size. **Conclusions.** In acute MI patients, serratus anterior resulted to be the most reliable and reproducible muscle for measuring the extent of myocardial edema.

1. Introduction

Myocardial edema has evolved as a novel noninvasive tool for assessing the acuity of heart diseases in experimental [1–3] and clinical [4, 5] studies. Acute myocardial injury leads to increased tissue free water content, partly because of protein disruption as well as net inflow through leaky capillaries. Because free water has a much (about 40-fold) longer T2 relaxation time, the affected tissue has a higher signal intensity in T2-weighted (T2-w) images. This has been reported in experimental models [1, 2] and in patients with acute coronary syndrome [3], acute myocardial infarction (MI) [4], acute myocarditis [5, 6], and stress-induced Takotsubo

cardiomyopathy [7]. Depending on the underlying pathology, myocardial edema can be a regional or diffuse process.

The most frequently used CMR sequence for assessing myocardial edema is the segmented Fast Spin Echo technique with a triple inversion recovery preparation, which suppresses the signal from blood flow and fat [8]. Beyond its T2 sensitivity, this sequence has been shown to be particularly useful for visualizing tissue edema [9]. In such images, myocardial edema can be evaluated qualitatively by visual estimation, using signal intensity cut-off values based on specific thresholds above the mean signal of remote myocardium, or by normalizing the signal to skeletal muscle for quantifying global edema, as proposed for acute

myocarditis [5, 10, 11]. The latter approach, optimally obtained using a body coil, provides a signal intensity ratio, also referred to as the T2 signal intensity ratio (T2 SI ratio) and may overcome an important limitation of T2-weighted imaging: artifacts leading to an artificially low signal intensity of the tissue. The T2 SI ratio does not use low signal intensity areas as reference regions and thus is not sensitive to such artifacts. The selection of the skeletal muscle, in contrast, is under the discretion of the reader and thus is often a source of observer bias. Furthermore, different skeletal muscles may be more or less suitable as a reference.

We aimed to identify the suitability of various skeletal muscles as reference regions for calculating the T2 SI ratio using the edematous area measured visually on T2-weighted images as a standard of truth, in patients with acute myocardial infarction.

2. Methods

2.1. Subjects. We retrospectively selected 34 consecutive patients presenting with acute, first-time STEMI, who underwent CMR at 1.5 T within 5 days from onset of symptoms (mean time to reperfusion was 337 minutes). Patients were excluded if they were clinically unstable or had severe arrhythmias or known contraindications to CMR. A diagnosis of MI was based on infarct-typical ECG changes combined with a >2-fold elevation of creatine kinase and/or positive troponin T. Infarct localization was performed via coronary angiography which identified the territory of the culprit vessel.

The control group consisted of 15 patients who underwent a CMR follow-up 5 months after the acute myocardial infarction (chronic MI). The time between the first and the second CMR scan was 160 ± 25 days. None of the 15 patients had any clinical events between the two CMR studies.

Patients gave written informed consent and the study was approved by our internal review board.

2.2. CMR Protocol. CMR examinations were performed using a 1.5 T MRI system (Magnetom Avanto, Siemens Medical Systems, Erlangen, Germany). Localization was performed by using real-time, breath-hold, and steady state free precession images of true anatomic axes of the heart.

The CMR protocol included cine steady state free precession (SSFP) CMR images for left ventricular (LV) function in a short axis orientation from base to apex, for a total of 8 to 10 slices. Cine SSFP images were obtained using the following parameters: repetition time (TR) 3.2 ms, echo time (TE) 1.07 ms, flip angle 65° , slice thickness 10 mm, no interslice gap, matrix 125×192 , field of view ranging from 340 to 400 mm, and voxel size $1.7 \times 1.7 \times 10$ mm. T2-w images were obtained using a breath-hold, triple inversion recovery sequence (TR 2 RR intervals; echo time (TE) 61 ms, inversion time (TI) 170 ms, and flip angle 180°) in a short axis plane (slice thickness 10 mm; no interslice gap; field of view 340 to 400 mm; matrix 166×256) using a body coil in the same slice orientation as the cine SSFP images.

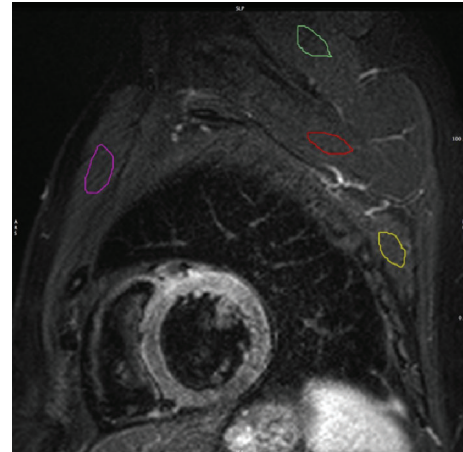


FIGURE 1: Short axis T2-w STIR image with 4 different ROI placed in 4 different skeletal muscles. The colored regions of interest mark the major and minor pectoralis muscles (purple), the serratus anterior muscle (yellow), the teres minor-infraspinatus muscle (green), and the subscapularis muscle (red).

2.3. Image Analysis. The T2 SI in T2-w images was quantified with certified software (cmr⁴², Circle Cardiovascular Imaging Inc., Calgary, AB, Canada), using cine images of the same cardiac phase for verifying wall thickness and the correct identification of the skeletal muscle. The endocardial and epicardial borders of the LV myocardium were manually traced in each T2-w slice excluding trabeculae and papillary muscles. The T2 SI ratio was calculated by dividing the SI of the myocardium by the SI of skeletal muscle in the same slice [5]. In a color-coded map of the T2 SI ratio, at least 10 conjoint pixels with a positive T2 SI ratio were considered evidence of edema. A hypointense core within a high SI area was included in the edematous volume. Four different muscles were selected for T2 SI ratio analysis: one anterior, one posterior, and two superior (one proximal and one distal) to the LV myocardium (Figure 1). For the anterior muscle, a combination of major and minor pectoralis muscles was used. The serratus anterior muscle (SA) served as the posterior muscle. For the superior muscle distal to the LV myocardium, a combination of infraspinatus (basal slices) and teres minor (apical slices) muscles was used. The subscapularis muscle was used for the superior muscle proximal to the LV myocardium. Using cine images as a reference each muscle group was identified on T2-w images and assessed for suitability based on the visible area and absence of fat.

Visual analysis of T2-w images was considered the reference standard for the quantification of the edema size. T2-w hyperintense areas were first defined by visual analysis during which the window settings could be freely adjusted to the personal preference of the observer and were manually contoured.

To test intraobserver variability the analysis of T2-w images was repeated in 20 randomly selected patients (10 patients with acute MI and 10 patients with chronic MI), after 4 weeks by the same reader (IC, 10 years of experience

TABLE 1: Patients population characteristics.

Time to reperfusion (min)	335,73 ± 259,91
Troponin peak (UI/mL)	4,09 ± 5,10
TIMI after revascularization	3
Infarct-related artery	
LAD	12 (40%)
LCX	3 (10%)
RCA	15 (50%)
	Risk factors
Arterial hypertension	9 (30%)
Hypercholesterolemia	10 (33,3%)
Diabetes mellitus	3 (10%)
Familiar history of CAD	10 (33,3%)
Cigarette smoking	
Yes	12 (40%)
No	6 (20%)
Ex-smoker	12 (40%)

in CMR). To test interobserver agreement a second reader (AA, 1 year of experience in CMR) performed the T2 analysis separately in the same 20 patients (10 patients with acute MI and 10 patients with chronic MI).

2.4. Statistical Analysis. The difference between measurements was assessed with paired *t*-tests using PASW Advanced Statistics 19.0.0 (SPSS, Chicago). Differences were considered significant if the two-tailed *P* value was less than 0.05. Pearson correlation coefficient calculations were used to determine the linear relationship between sample observations with a significant correlation occurring when the *P* value was less than 0.05. Anova analysis was performed to compare edema mass average values. Bland Altman plots [12] were generated to assess inter- and intraobserver agreement by plotting the difference and mean values for each method. Intraclass correlation coefficient was computed to assess reproducibility both for intra- and interobserver measurements.

Chronic patient data were also analyzed using paired *t*-tests.

3. Results

3.1. Acute MI. We studied 34 patients, four patients were excluded due to poor quality T2-w images, leaving 30 patients (24 men; mean age 52.7 ± 11 years) with 168 T2-w images considered suitable for analysis. Detailed patients population characteristics are reported in Table 1. Edema location perfectly matched with angiographic findings and resulted to be anterior in 12 patients (40%), lateral in 3 (10%), and inferior in 15 patients (50%). A combination of major and minor pectoralis muscles was visualized in 164/168 images (97.6%); the serratus anterior was visualized in 150/168 slices (89.2%); the subscapularis was visualized in 131/168 slices (77.9%); a combination of teres minor and infraspinatus muscles was visualized in 135/168 slices (80.3%).

The mean size of edematous area in patients with acute MI using the visual analysis was 34.8 ± 3 g. Using the T2 SI ratio, the quantification of myocardial edema was 27.9 ± 3 g with the serratus anterior, 39.9 ± 4.7 g with the subscapularis muscle, 45.1 ± 5.9 g with a combination of infraspinatus and teres minor muscles, and 36.7 ± 4.5 g using a combination of major and minor pectoralis muscles (Figure 3(a)). Anova analysis resulted in a very low *P* value (<0.01) confirming that average values are different. Quantified visually, the edematous area was strongly correlated with the area determined by the T2 SI ratio, when the muscles serratus anterior, the subscapularis, and a combination of major and minor pectoralis muscles were used ($P \leq 0.001$), while the serratus anterior showed the strongest correlation ($r = 0.799$) (Table 2, Figure 2). The area of increased T2-w SI measured by a combination of the teres minor and infraspinatus muscles was less correlated with the visual analysis ($P = 0.008$; $r = 0.578$). There was no significant difference between the extent of T2-w SI measured with the 4 different muscles and the visual analysis, although the serratus anterior showed a tendency to underestimate the edematous area (Table 2; Figure 3(a)).

For evaluations using the serratus anterior, the interobserver variability for the edematous area was low and there was no significant difference between readers ($P = 0.142$, Table 2). All other muscle groups resulted in a significant interobserver variability ($P < 0.005$, Table 2). Similarly, a low intraobserver variability was observed for high SI abnormalities as evaluated by the serratus anterior ($P = 0.389$, Table 2). While a combination of teres minor and infraspinatus also resulted in a very good agreement ($P = 0.715$, Table 2), the intraobserver variability was larger when a combination of major and minor pectoralis muscles or the subscapularis was used as a reference ($P = 0.059$ and 0.140 , resp., Table 2).

A Bland Altman analysis indicated the serratus anterior muscle was far superior with respect to reproducibility of the edematous area in patients with acute MI. In both the intra- and interobserver analysis the serratus anterior measurements deviated least from one another, compared to other muscle groups used (Figure 4). The agreement mentioned earlier for the teres minor and infraspinatus group can also be visualized in these graphs (Figure 4). The subscapularis was the most unreliable muscle group (Figure 4).

3.2. Chronic MI. In the 15 patients with chronic MI, a total of 111 T2-w images were considered suitable for analysis.

A combination of major and minor pectoralis muscles was visualized in 99/111 slices (89.2%), muscle serratus anterior was visualized in 95/111 slices (85.6%), muscle subscapularis was visualized in 98/111 slices (88.3%), and a combination of teres minor and infraspinatus muscles was visualized in 95/111 slices (85.6%).

The mean size of the T2-w hyperintense area in patients with chronic MI was 1.5 ± 0.6 g using serratus anterior muscle, whereas for the subscapularis muscle, a combination of infraspinatus and teres minor muscles, and a combination of major and minor pectoralis muscles, it was 21.6 ± 5.2 g, 44.5 ± 8.9 g, and 26.7 ± 7.6 g, respectively (Figure 3(b)). An

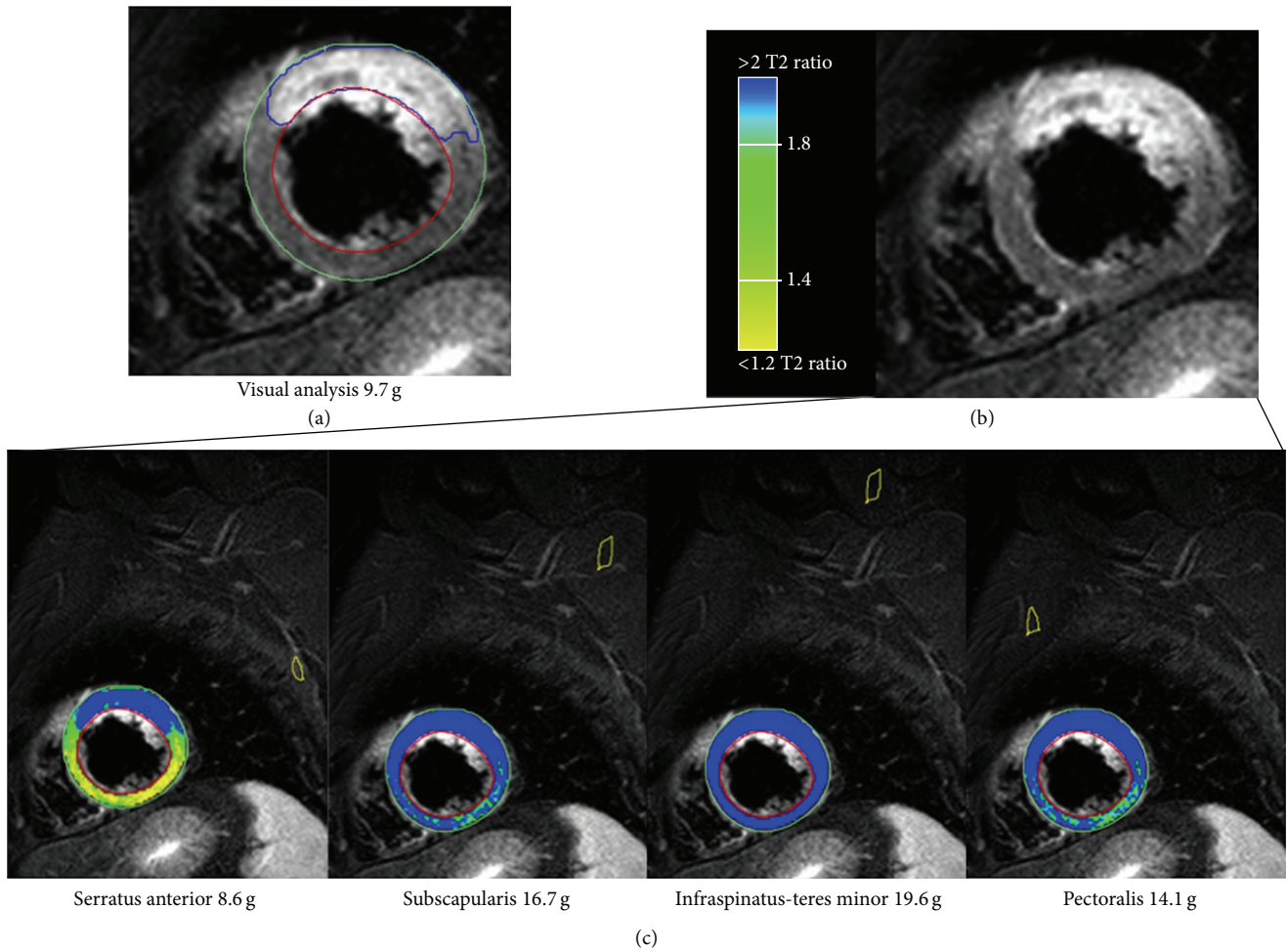


FIGURE 2: Results for quantitative assessment of the myocardium at risk in a patient with acute anterior myocardial infarction. (a) T2-w STIR image in a basal short axis view showing the quantification of the myocardial edema performed by the visual analysis, resulting in a mass of 9.7 g. (b) The same T2-w STIR without any contour. (c) Color-coded visualization of the automated sizing of the myocardial edema using the T2 SI ratio with four different muscle groups as reference regions. Despite a small overestimation, the serratus anterior resulted the most accurate for the size of the edematous myocardium (8.6 g).

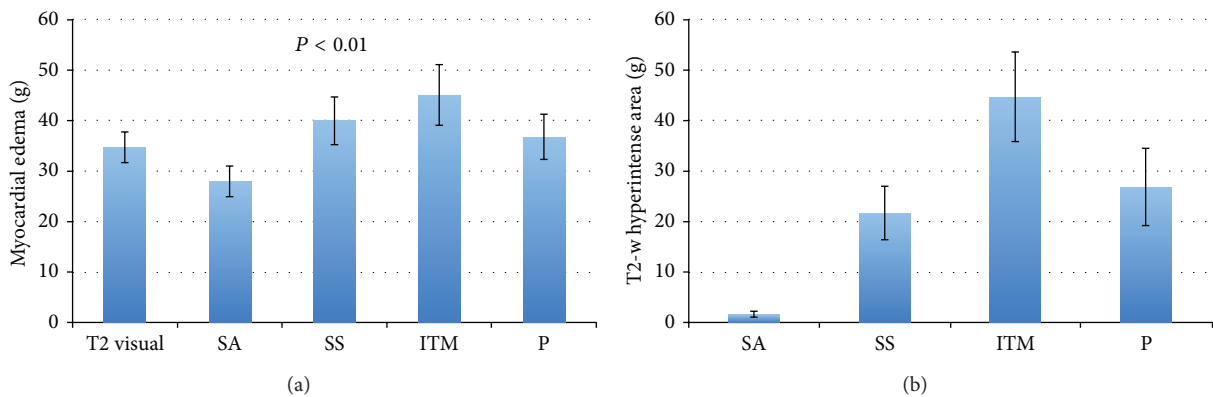


FIGURE 3: (a) Mean edema mass (\pm SE), obtained with the T2 SI ratio in different muscles in patients with acute MI. Increased T2-w SI area referenced to the serratus anterior muscle was closely correlated with myocardial edema measured visually. (b) Comparison between the mean T2-w hyperintense area (\pm SE), obtained with the T2 SI ratio, and other muscles in patients with chronic MI. False positive areas with increased T2-w SI area were very small, whereas with the use of other muscles they led to an apparent edematous area of more than 20 g. SA: serratus anterior; SS: subscapularis; ITM: infraspinatus-teres minor; P: major and minor pectoralis.

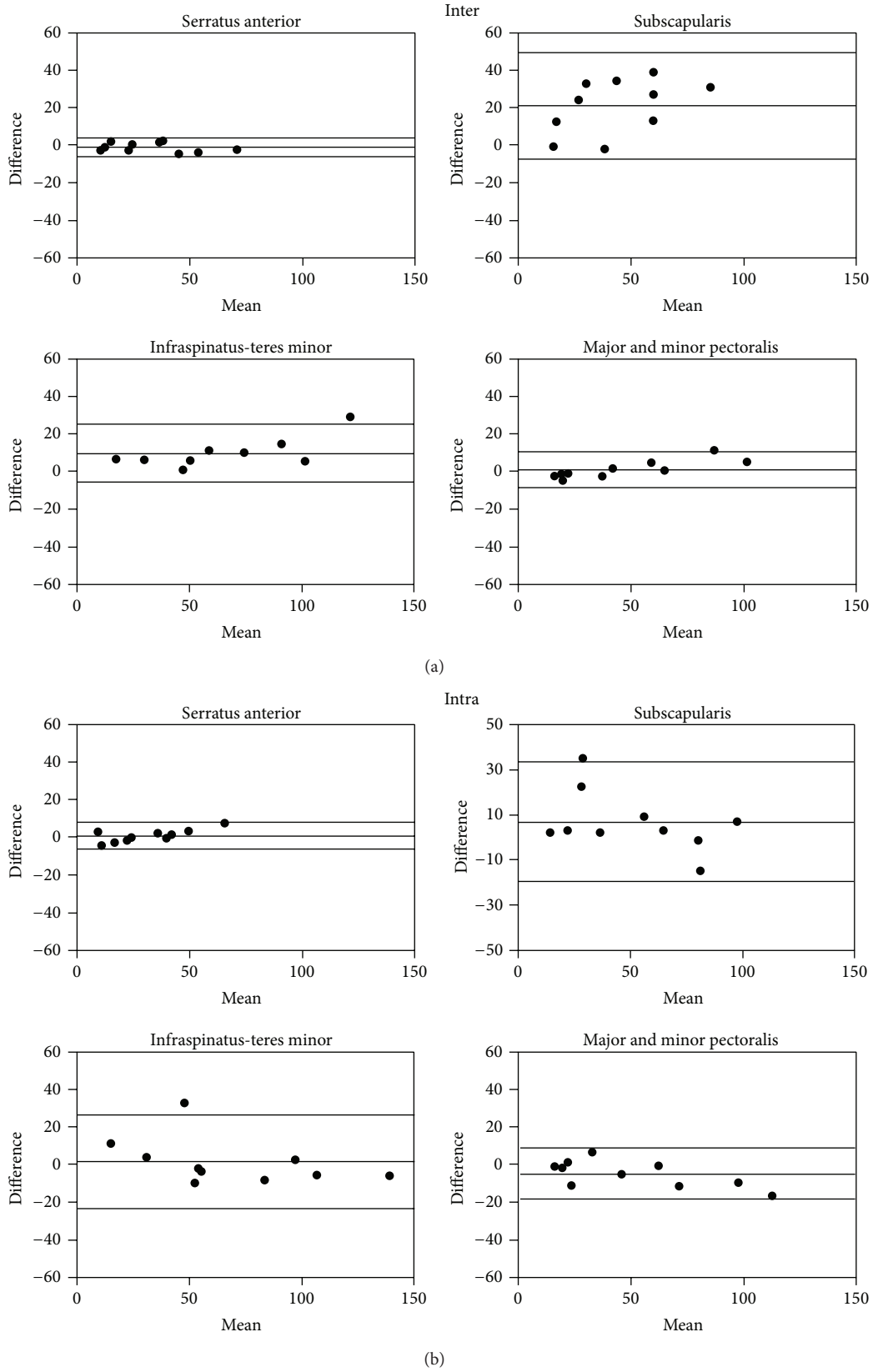


FIGURE 4: Bland Altman analysis of inter- (a) and intraobserver variability (b) of T2 SI ratio measurements with 95% confidence intervals using different muscle groups in acute MI in patients. Enhancement referenced to the serratus anterior muscle had the best inter- and intraobserver agreement.

TABLE 2: Correlation of edematous mass as measured by the T2 SI ratio in patients with acute MI in different muscle groups with infarct mass (5SD LGE); differences as per paired *t*-test with corresponding *P* value and Pearson's correlation coefficient with *P* value. Intraclass correlation coefficient for interrater reliability and intrarater agreement.

Acute reperfused MI	Difference T2-w versus visual analysis	Correlation with T2-w visual analysis	Interobserver difference	Interobserver correlation	Intraobserver difference	Intraobserver correlation
Muscle	Mean (<i>P</i>)	<i>r</i> (<i>P</i>)	Mean (<i>P</i>)	ICC	Mean (<i>P</i>)	ICC
Serratus anterior	-6.8 ± 4.3 (0.118)	0.799 (<0.001)	1.23 ± 2.4 (0.142)	0.993	1.02 ± 3.6 (0.389)	0.981
Subscapularis	5.2 ± 5.6 (0.358)	0.669 (<0.001)	21.0 ± 15, (0.001)	0.521	7.0 ± 14 (0.140)	0.879
Teres minor/infraspinatus	10.3 ± 6.7 (0.129)	0.579 (0.008)	9.6 ± 7.9 (0.004)	0.933	1.52 ± 13 (0.715)	0.943
Pectoralis	1.9 ± 5.4 (0.715)	0.675 (<0.001)	1.44 ± 5 (0.001)	0.988	4.83 ± 7 (0.059)	0.972

TABLE 3: Extent of false positive edematous mass as measured by the T2 SI ratio in patients with chronic MI in different muscle groups; differences as per paired *t*-test with corresponding *P* value and intraclass correlation coefficient for interrater reliability and intrarater agreement.

Chronic reperfused MI	Interobserver difference	IIC interobserver correlation	Intraobserver difference	ICC intraobserver correlation
Muscle	Mean (<i>P</i>)	ICC	Mean (<i>P</i>)	ICC
Serratus anterior	0.30 ± 0.50 (0.065)	0.954	0.12 ± 0.36 (0.313)	0.98
Subscapularis	23 ± 30.0 (0.039)	0.328	23.2 ± 28.0 (0.027)	0.259
Teres minor/infraspinatus	1.91 ± 11.0 (0.580)	0.966	3.43 ± 8.6 (0.239)	0.974
Pectoralis	0.78 ± 5.6 (0.672)	0.983	2.95 ± 9.0 (0.349)	0.953

example of the analysis of chronic MI using all the different muscles is illustrated in Figure 5.

Using the muscle serratus anterior as a reference, there was no significant interobserver variability ($P = 0.065$, Table 3), while the subscapularis muscle was less reproducible between two readers ($P = 0.039$, Table 3). Using a combination of infraspinatus and teres minor muscles and a combination of major and minor pectoralis muscles also did not show any significant difference between observers ($P = 0.580$, $P = 0.672$, Table 3).

Also, no significant intraobserver variability was observed with the serratus anterior, infraspinatus-teres minor, or pectoralis muscle groups ($P > 0.24$, Table 3). There was, however, significant intraobserver variability when using the subscapularis muscle ($P = 0.027$, Table 3).

In patients with chronic MI, the Bland Altman graphs indicated that the serratus anterior was the best muscle due to its reliability and reproducibility with the same observer and between observers. In both the intra- and interobserver analysis the serratus anterior measurements deviated least from one another, compared to other muscle groups used (Figure 6).

4. Discussion

Our data indicate that the selection of skeletal muscles as reference regions affects results when quantifying the extent of the myocardial area at risk using the T2 SI ratio. The data indicate that sizing myocardial edema using the serratus anterior muscle as a reference resulted in the best agreement with its expected extent. While the area of the myocardium at risk strongly correlated with the visual quantification of the size of edematous area using all the 4 different muscles groups, the serratus anterior muscle had the strongest correlation and best interobserver and intraobserver agreement. The inferior correlation of other muscles may be explained by magnetic field inhomogeneities, affecting the signal intensity quantification in the context of a low signal-to-noise ratio.

The use of the serratus anterior muscle, however, led to an underestimation of the edematous area when compared with the visual assessment. This should be considered when an exact quantification of the salvaged area at risk is required (e.g., to assess the benefit of early [13] or late [1] revascularization).

In patients with chronic MI, where edema should not be present, the serratus anterior did not show relevant false

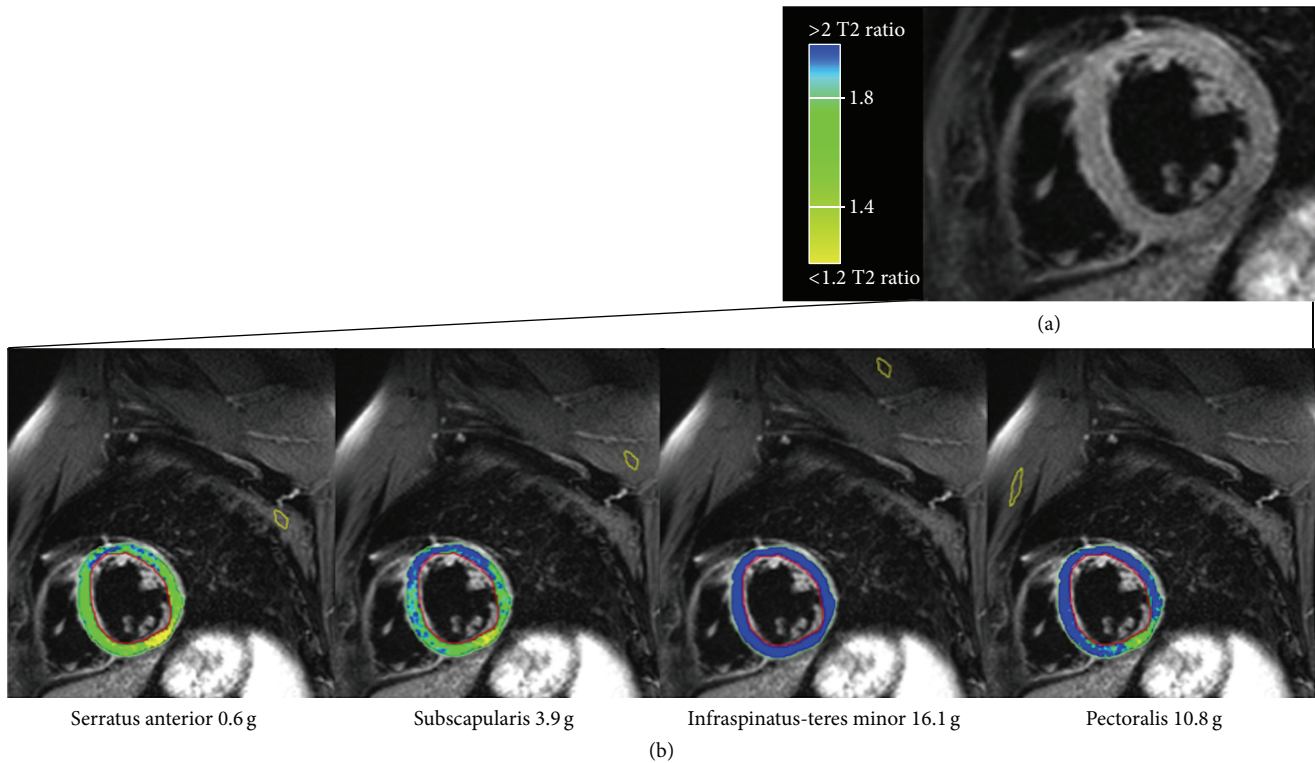


FIGURE 5: Basal short axis views in a patient 5 months after acute myocardial infarction (the same patient as shown during the acute stage in Figure 2). (a) T2-weighted image without evidence of significantly increased signal intensity. (b) Color-coded visualization of the automated sizing of the myocardium at risk using the T2 SI ratio with four different muscle groups as reference regions. All muscles except for the serratus anterior resulted in significant false positive results.

positive results (apparent edema size 1.5 ± 0.6 g versus 21.6 ± 5.2 g to 44.5 ± 8.9 g when using other reference muscles). Furthermore in those patients, evaluation using the serratus anterior muscle as a reference also showed low intra- and interobserver variability. These results and the Bland Altman plots suggest that the serratus anterior is the best available reference muscle when normalizing the myocardial signal intensity for a quantitative analysis of myocardial edema.

Clear visibility of the muscle serratus anterior was present in 85–89% (85% in the chronic patients, 89% in the acute patients) and was mostly limited to the more basal planes. As per our results, however, a combination of the major and minor pectoralis can be used as an alternative to the serratus anterior muscle especially in the more apical planes.

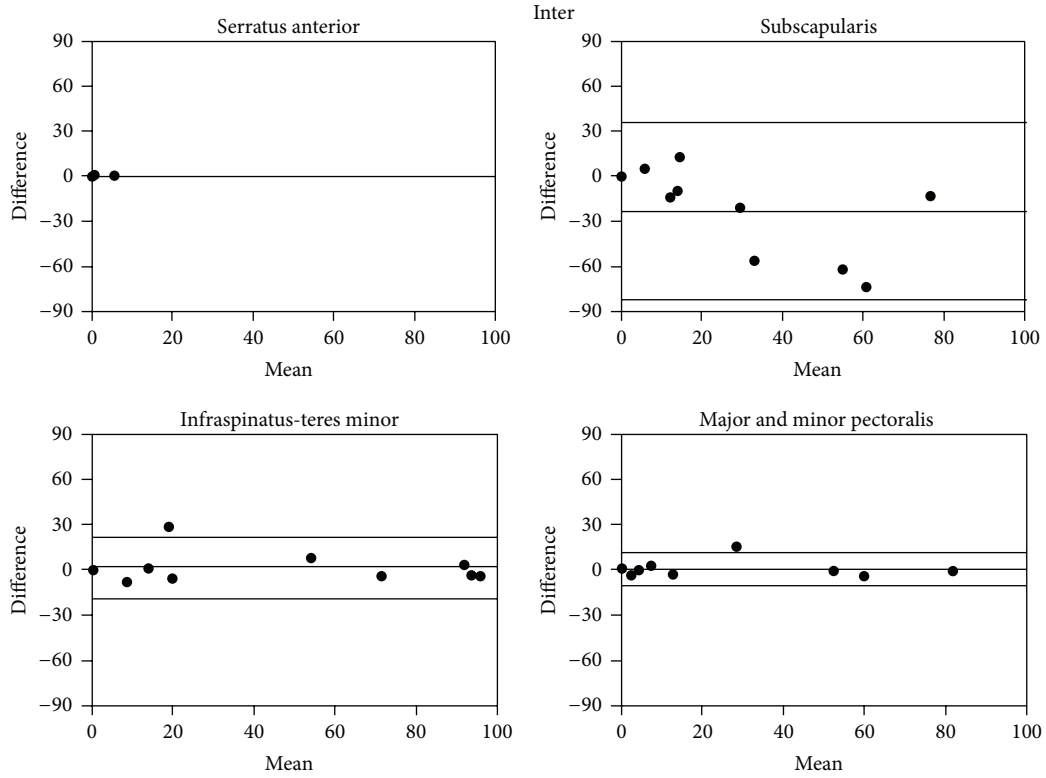
While a standardized method for the quantification of myocardial edema appears essential, especially in patients with diffuse edema, most studies do not specify the skeletal muscle used for the T2 SI ratio [1, 5, 9, 14]. In a recent paper, Röttgen et al. [11] used the erector spinae when analyzing 131 patients with acute myocarditis; they reported a sensitivity and specificity of 58.3% and 57.1%, respectively, for the detection of edema using pathological specimen as a gold standard. A comparison with other reference muscles has not been performed, but the selection of the muscle may have had a significant impact on such analysis.

The exact cause of the better performance of the serratus anterior to other muscle groups could be related to B0 field inhomogeneity as well as the location of the muscle. Using

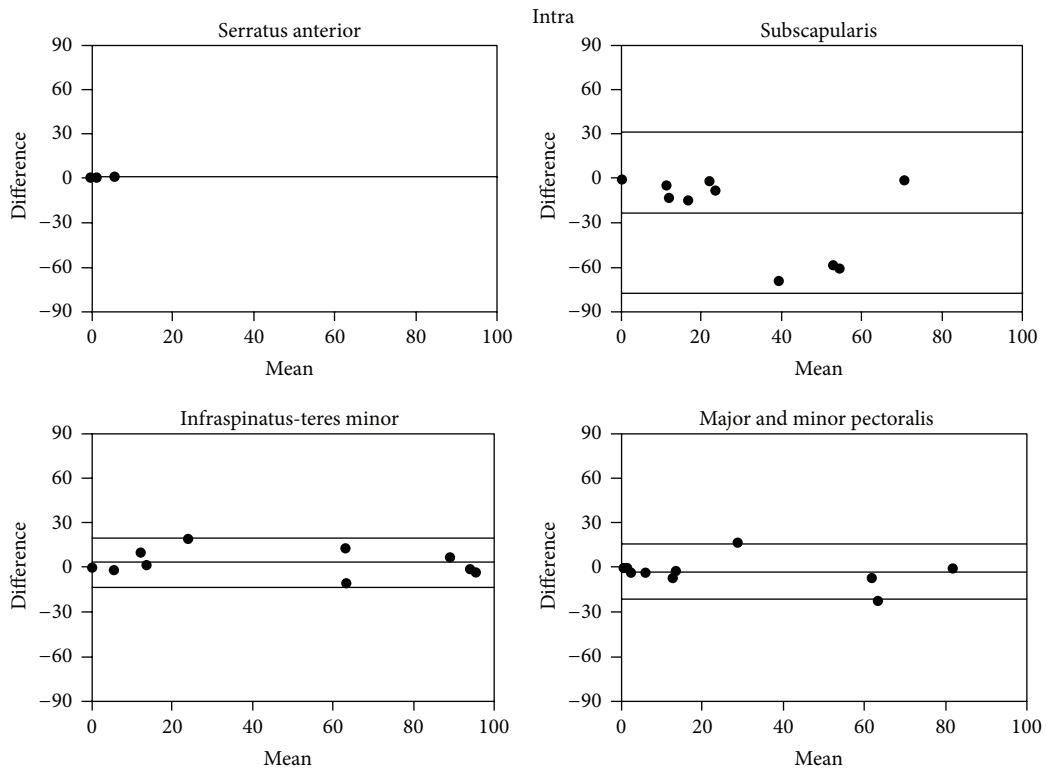
the body coil, the isocenter of the magnet has the highest level of magnetic field homogeneity. With increasing distance from the center this homogeneity decreases, which may account for a signal loss in the skeletal muscle, leading to a false high T2 SI ratio. Similarly, there is also an increased B1 inhomogeneity related to the RF pulse in the periphery of the FOV. Furthermore, among the four muscle groups the serratus anterior was the only muscle located at the same level of the LV, along the z-axis, and thus is expected to be at the same level of homogeneity. Nonetheless, further studies are needed to confirm these findings and better understand the different variables involved in the assessment of edema using skeletal muscle referencing. Finally, with age, the subscapularis and teres minor-infraspinatus muscles tend to undergo atrophy and subsequent fatty replacement [14]. This would result in a decreased SI in the T2-STIR images and a subsequent increase of the T2 SI ratio when using these muscles as a reference.

Recently, T2 mapping has emerged as a novel approach to assess infarct-related edema [15]; yet the spatial resolution of T2 mapping is inferior to that of T2-weighted imaging and image registration issues may further limit its utility. Thus, more validation studies are required, before T2 mapping can be considered clinically useful.

4.1. Study Limitations. We used a visual analysis as a standard of truth in evaluating the area of increased T2-w signal intensity, which may be subject to observer bias. Visual analysis



(a)



(b)

FIGURE 6: Bland Altman analysis of inter- (a) and intraobserver variability (b) assessment of the T2 SI ratio measurements of the edematous area with 95% confidence intervals using different muscle groups in patients with chronic MI. Enhancement referenced to the serratus anterior muscle had the best inter- and intraobserver agreement. 95% confidence intervals are labeled.

has been used as the standard reference for the present study, since myocardial edema cannot be histologically quantified in patients with AMI. An increased amount of free water results in a bright signal on T2-w images which can be visually seen.

While detection of focal processes (i.e., AMI) is more reliable with CMR, recognition of edema in diffuse diseases (i.e., acute myocarditis) remains a major challenge in which visual analysis is of limited support and validation of a reference muscle would provide better standardization and reproducibility of results [16].

The analysis was performed independently by an experienced observer, however, without comparing results during the analysis. Our sample is relatively small and represents patients with acute and chronic myocardial infarction only. Reflecting clinical practice, we analyzed images only in short axis views; thus, our results may be less applicable to long axis images.

5. Conclusion

This study shows that the serratus anterior muscle should be the first choice for quantifying the extent of myocardial edema by calculating the T2 signal intensity ratio with a skeletal muscle reference. This is due to the availability and reliability of the serratus anterior, relative to other muscles groups. However, more studies should be performed. Our findings also demonstrate the need for the standardization of T2 signal evaluation to avoid significant variability among different readers and centers.

Key Points

- (1) Role of skeletal muscle reference for the quantification of myocardial edema.
- (2) A standardized approach for the quantification of myocardial edema is highly desirable.
- (3) The muscle serratus anterior provides reliable and reproducible results for myocardial edema quantification.

Conflict of Interests

Matthias G. Friedrich is advisor and shareholder of Circle Cardiovascular Imaging, the manufacturer of the software used in this study.

References

- [1] H. Abdel-Aty, M. Cocker, C. Meek, J. V. Tyberg, and M. G. Friedrich, "Edema as a very early marker for acute myocardial ischemia: a cardiovascular magnetic resonance study," *Journal of the American College of Cardiology*, vol. 53, no. 14, pp. 1194–1201, 2009.
- [2] R. J. Beyers, R. S. Smith, Y. Xu et al., "T2-weighted MRI of post-infarct myocardial edema in mice," *Magnetic Resonance in Medicine*, vol. 67, no. 1, pp. 201–209, 2012.
- [3] R. C. Cury, K. Shash, J. T. Nagurney et al., "Cardiac magnetic resonance with T2-weighted imaging improves detection of patients with acute coronary syndrome in the emergency department," *Circulation*, vol. 118, no. 8, pp. 837–844, 2008.
- [4] H. Abdel-Aty, A. Zagrosek, J. Schulz-Menger et al., "Delayed enhancement and T2-weighted cardiovascular magnetic resonance imaging differentiate acute from chronic myocardial infarction," *Circulation*, vol. 109, no. 20, pp. 2411–2416, 2004.
- [5] H. Abdel-Aty, P. Boyé, A. Zagrosek et al., "Diagnostic performance of cardiovascular magnetic resonance in patients with suspected acute myocarditis: comparison of different approaches," *Journal of the American College of Cardiology*, vol. 45, no. 11, pp. 1815–1822, 2005.
- [6] M. G. Friedrich, U. Sechtem, J. Schulz-Menger et al., "Cardiovascular magnetic resonance in myocarditis: a JACC white paper," *Journal of the American College of Cardiology*, vol. 53, no. 17, pp. 1475–1487, 2009.
- [7] I. Eitel, F. Von Knobelsdorff-Brenkenhoff, P. Bernhardt et al., "Clinical characteristics and cardiovascular magnetic resonance findings in stress (takotsubo) cardiomyopathy," *The Journal of the American Medical Association*, vol. 306, no. 3, pp. 277–286, 2011.
- [8] O. Simonetti, "Black blood' T2-w inversion recovery MR imaging of the heart," *Radiology*, vol. 199, no. 1, pp. 1–9, 1996.
- [9] D. O. H-Ici, J. P. Ridgway, T. Kuehne et al., "Cardiovascular magnetic resonance of myocardial edema using a short inversion time inversion recovery (STIR) black-blood technique: diagnostic accuracy of visual and semi-quantitative assessment," *Journal of Cardiovascular Magnetic Resonance*, vol. 14, no. 1, article 22, 2012.
- [10] M. G. Friedrich, O. Strohm, J. Schulz-Menger, H. Marciniak, F. C. Luft, and R. Dietz, "Contrast media-enhanced magnetic resonance imaging visualizes myocardial changes in the course of viral myocarditis," *Circulation*, vol. 97, no. 18, pp. 1802–1809, 1998.
- [11] R. Röttgen, R. Christiani, P. Freyhardt et al., "Magnetic resonance imaging findings in acute myocarditis and correlation with immunohistological parameters," *European Radiology*, vol. 21, no. 6, pp. 1259–1266, 2011.
- [12] J. M. Bland and D. G. Altman, "Statistical methods for assessing agreement between two methods of clinical measurement," *The Lancet*, vol. 1, no. 8476, pp. 307–310, 1986.
- [13] M. Francone, C. Bucciarelli-Ducci, I. Carbone et al., "Impact of primary coronary angioplasty delay on myocardial salvage, infarct size, and microvascular damage in patients with ST-segment elevation myocardial infarction: insight from cardiovascular magnetic resonance," *Journal of the American College of Cardiology*, vol. 54, no. 23, pp. 2145–2153, 2009.
- [14] D. O'Reilly and R. M. Bernstein, "Shoulder pain in the elderly," *British Medical Journal*, vol. 301, no. 6751, pp. 503–504, 1990.
- [15] S. Hammer-Hansen, M. Ugander, L. Y. Hsu et al., "Distinction of salvaged and infarcted myocardium within the ischaemic area-at-risk with T2 mapping," *European Heart Journal—Cardiovascular Imaging*, vol. 15, no. 9, pp. 1048–1053, 2014.
- [16] M. Francone, C. Chimenti, N. Galea et al., "CMR sensitivity varies with clinical presentation and extent of cell necrosis in biopsy-proven acute myocarditis," *JACC: Cardiovascular Imaging*, vol. 7, no. 3, pp. 254–263, 2014.